Investigations on NiZn Ferrite – PZT Composites

A Thesis submitted
for the
Award of the Degree of

Doctor of Philosophy

By

Rekha Rani
(Regn. No. 900912018)

To

School of Physics & Materials Science
Thapar University, Patiala-147 004
Punjab, India

October 2012

This thesis is dedicated

to

my grand parents

Late Sh. Kishan Chand Gandhi

and

Late Smt. Ishwar Devi

CERTIFICATE

This is to certify that the thesis entitled, **"Investigations on NiZn Ferrite – PZT Composites"** being submitted by **"Ms. Rekha Rani"** in fulfillment of the requirements for the award of degree of Doctor of Philosophy to Thapar University, Patiala is a record of bonafide research carried out by her under our supervision and guidance. In our opinion, the work fulfills the requirements for which it is being submitted.

The work incorporated in this thesis has not been submitted elsewhere earlier, in part or in full, for the award of any other degree in this or any other institution or university.

Supervisors

Dr. Chandra Prakash
Directorate of ER&IPR, DRDO
DRDO Bhawan, New Delhi- 110105

Dr. J.K. Juneja
Department of Physics
Hindu College, Sonepat- 131001

Dr. K.K. Raina
School of Physics & Materials Science
Thapar University, Patiala- 147004

ACKNOWLEDGEMENTS

There are many people, to mention in these few paragraphs, who helped me to get to this point. I would like to take this opportunity to thank some of the people who contributed most to the completion of this thesis.

First and foremost, I am extremely grateful to my supervisors **Dr. Chandra Prakash** (DRDO, New Delhi), **Dr. J.K. Juneja** (Hindu College, Sonepat) and **Dr. K.K. Raina** (Thapar University, Patiala) for their motivation, enthusiasm, consistent encouragement and immense knowledge, I received throughout this research work. Their guidance helped me all the time during my research work and thesis writing. I deem it as my privilege to do my doctoral programme under their supervision.

I sincerely thank **Dr. Abhijit Mukherjee**, Director, Thapar University, Patiala for the academic support and the facilities provided to carry out the research work at the university. **Dr. Kulbir Singh**, Head, SPMS, Thapar University, Patiala has been very encouraging and supportive. I express my gratitude to him. At the same time, I would like to express my gratitude to my doctoral committee members, **Dr. Puneet Sharma** and **Dr. Susheel Mittal** for their valuable comments and suggestions during research progress meetings.

Special thanks to **Dr. O.P. Pruthi**, Chairman, Managing Committee and **Dr. Jyoti Juneja**, Principal, GVM Girls College, Sonepat for providing me with necessary research facilities at Electroceramics Research Lab (ERL) at GVM Girls College, Sonepat. Without their help and cooperation, it could not have been possible for me to complete this work. I would also like to thank **Dr. Sangeeta Singh**, GVM Girls College, Sonepat for sharing her valuable time and giving me inspiring ideas to finish this work in time. I will always appreciate her cooperation.

I express my sincere thanks to **Dr. R.K. Kotnala**, National Physical Laboratory, New Delhi for his kind permission to undertake magnetization measurements related to the work. I also acknowledge the contribution of **Dr. Jyoti Shah**, Research Associate, National Physical Laboratory, New Delhi for helping me in magnetic measurements. I do thank **Dr. R.S. Kundu**, GJUS&T, Hisar for providing facilities for SEM measurements. I am

also thankful to **Dr. Nawal Kishore** and **Dr. Rajesh Punia**, GJUS&T, Hisar for numerous discussions and suggestions on related topics that helped me to improve my knowledge in the area.

The financial support in the form of research fellowship through **Department of Science & Technology (DST)**, Govt. of India under INSPIRE AORC scheme is greatly acknowledged. I would also like to acknowledge **CSIR, CICS and PSCST** for providing me financial assistance to visit UNSW, Sydney, Australia to present my work during International Conference on Electroceramics on December 12-16, 2011.

This thesis could not have been completed without the help and useful discussions with my friends and colleagues **Dr. Parveen Kumar, Dr. Pratibha Singh, Ravi Shukla, Renu Rani** and **Dipti**. I would also like to acknowledge the contribution of my friends including **Ramneek Kaur, Gurpreet Kaur, Rishi Kumar** and **Supreet Kaur** at Materials Research Lab, Thapar University for providing essential help throughout the course of my Ph.D. study.

I would also like to thank all the support staff at various institutes, universities and college in which I carried out my research work for their cooperation.

I am very much indebted to my beloved parents whose foresight and values paved the way for a privileged education. Their love and confidence in me has encouraged me to go ahead in my study and career. My parents-in-law deserve my profound gratitude for their support, encouragement and prayer. Most of all, I would like to acknowledge my brother **Anil Gandhi**, brother-in-law **Vikas Sachdeva** and lovely sisters **Jyoti** & **Meenakshi** for their constant care and making this work enjoyable. I thank my fiance **Gulshan Sachdeva** for being so understanding and a great support during past two years.

Above all, I owe it all to Almighty God for his blessings to complete the thesis successfully.

REKHA RANI

ABSTRACT

Many of the modern technologies require materials with unusual combinations of properties i.e. composite materials that exhibit a significant proportion of the properties of constituent phases such that a better combination of properties can be realized. These artificially made composites (multiphase materials) may acquire certain valuable properties not found in the components. The composites are classified as polymer composites, metal composites, elemental composites and ceramic composites. The area of interest in the present work is the magnetoelectric composites which belong to the class of ceramic composites consisting of magnetostrictive and ferroelectric materials.

The coexistence of magnetism and ferroelectricity and particularly existence of a coupling between constituent phases (magnetic and ferroelectric) known as Magnetoelectric (ME) Coupling brings about novel physical phenomenon. Hence the study of magnetoelectric composites has become one of the most popular areas in the field of materials science and offers new ideas for multifunctional materials suitable for a variety of device applications like magnetic field sensors, multiple state memory elements, transducers for magnetic field measurements, electro–optic devices with switching in magnetic fields, magnetically tuned capacitors etc. In recent years, a combination of ferrimagnetic and ferroelectric materials has been extensively studied resulting in magnetostriction induced deformation (ferrite phase) and the generation of piezoelectric charge (ferroelectric phase). However, utilizing magnetoelectric composites for multifunctional device applications is still limited and various research groups have been trying to improve ME coupling by suitable substitutions and better control of processing parameters.

For the present work, composites of NiZn ferrite and PZT were studied and efforts have been made to improve their dielectric, ferroelectric, piezoelectric, magnetic and magnetoelectric properties. In order to achieve the above objectives, the following ceramic compositional series were prepared for detailed investigations:

- Series 1: Conventionally sintered $yNi_{0.8}Zn_{0.2}Fe_2O_4–(1–y)PbZr_{0.65}Ti_{0.35}O_3$ (y = 0, 0.05, 0.10, 0.15, 1)
- Series 2: Conventionally sintered $yNi_{0.8}Zn_{0.2}Fe_2O_4–(1–y)Pb_{1–3x/2}La_xZr_{0.65}Ti_{0.35}O_3$ (x = 0.01, 0.02, 0.03 and y = 0, 0.05, 0.10, 0.15)

- Series 3: Conventionally sintered $yNi_{0.8}Zn_{0.2}Fe_2O_4–(1–y)Pb_{1–3x/2}Sm_xZr_{0.65}Ti_{0.35}O_3$ (x = 0.01, 0.02, 0.03 and y = 0.05, 0.10)
- Series 4: Microwave sintered $yNi_{0.8}Zn_{0.2}Fe_2O_4–(1–y)PbZr_{0.65}Ti_{0.35}O_3$ (y = 0, 0.05, 0.10, 0.15, 1)

The research work carried out for the Ph.D. thesis entitled "Investigations on NiZn Ferrite–PZT Composites" consists of seven chapters.

Chapter I: Introduction

Chapter II: Synthesis and Characterization Techniques

Chapter III: Characterization of NZF-PZT Composites

Chapter IV: Characterization of NZF-PLZT Composites

Chapter V: Characterization of NZF-PSZT Composites

Chapter VI: Characterization of Microwave Sintered NZF-PZT Composites

Chapter VII: Summary & Recommendations for Future Work

Chapter–I gives an introduction to the basic concepts of ferroelectricity, magnetism and magnetoelectric materials. An overview of the historical development and research work that has been carried out till recently in this field is given. The criteria of selection of constituent phases (ferrite & ferroelectric) and aim of carrying out the present work are also discussed. **Chapter–II** includes a detailed description of the conventional solid state route and various intermediate steps adopted for the synthesis of constituent phases and composites. The details of the various characterization techniques used for studying structural, microstructural, dielectric, ferroelectric, piezoelectric, magnetic and magnetoelectric properties are also summarized in this chapter. **Chapter–III** concerns with the optimization of sintering temperature for $0.1Ni_{0.8}Zn_{0.2}Fe_2O_4–0.9PbZr_{0.65}Ti_{0.35}O_3$ composite sample. Results on $yNi_{0.8}Zn_{0.2}Fe_2O_4–(1–y)PbZr_{0.65}Ti_{0.35}O_3$ (NZF–PZT) with y = 0, 0.05, 0.10, 0.15 and 1 (Series 1) are discussed. Change in magnetic properties (M_r and M_s) for electrically poled composite samples is the evidence for magnetoelectric coupling in these composites. **Chapter–IV** presents the studies on structural, microstructural, dielectric, ferroelectric, piezoelectric, magnetic and magnetoelectric properties of $yNi_{0.8}Zn_{0.2}Fe_2O_4–(1–y)Pb_{1–3x/2}La_xZr_{0.65}Ti_{0.35}O_3$ (NZF–PLZT) with x = 0.01, 0.02, 0.03 and y = 0, 0.05, 0.10, 0.15 (Series 2). Comparison of results for this series with those for series 1 is also

given. **Chapter–V** discusses the improvement in properties for composites of NiZn ferrite and Sm substituted lead zirconate titanate having general formula $yNi_{0.8}Zn_{0.2}Fe_2O_4–(1–y)Pb_{1–3x/2}Sm_xZr_{0.65}Ti_{0.35}O_3$ (NZF–PSZT) with x = 0.01, 0.02, 0.03 and y = 0.05, 0.10 (Series 3). The results obtained using microwave sintering for series 1 in order to study structural, microstructural, dielectric, ferroelectric, piezoelectric, magnetic and magnetoelectric properties are discussed in **Chapter–VI**. A comparison of the properties with those obtained for conventionally sintered samples of series 1 is also given. **Chapter–VII** summarizes the important findings of the entire work. Recommendations for the future work are also given in this chapter.

LIST OF PUBLICATIONS

Refreed Journals (included in thesis)

1. *Dielectric Properties of 0.95($Pb_{1-3x/2}La_xZr_{0.65}Ti_{0.35}O_3$)-0.05($Ni_{0.8}Zn_{0.2}Fe_2O_4$) Composites*, **Rekha Rani**, Parveen Kumar, J.K. Juneja, K.K. Raina and Chandra Prakash, *Advances in Condensed Matter Physics **2011** (2011) 637170.*

2. *Ferroelectric Properties of La Substituted PZT Ceramics*, **Rekha Rani**, J.K. Juneja, K.K. Raina and Chandra Prakash, *American Institute of Physics **1372** (2011) 147.*

3. *Studies on Dielectric and Ferroelectric Properties of PZT: NZF Magnetoelectric Composites*, **Rekha Rani**, J.K. Juneja, K.K. Raina and Chandra Prakash, *Journal of Ceramic Processing Research **13** (2012) 76.*

4. *Study of 0.1$Ni_{0.8}Zn_{0.2}Fe_2O_4$-0.9$Pb_{1-3x/2}La_xZr_{0.65}Ti_{0.35}O_3$ Magnetoelectric Composites,* **Rekha Rani**, J.K. Juneja, Sangeeta Singh, K.K. Raina and Chandra Prakash, *Journal of Magnetism and Magnetic Materials **325** (2013) 47.*

5. *Ferroelectric, Magnetic and Magnetoelectric Properties of Ferroelectric Rich $Ni_{0.8}Zn_{0.2}Fe_2O_4$-$PbZr_{0.65}Ti_{0.35}O_3$ ME Composites*, **Rekha Rani**, J.K. Juneja, Sangeeta Singh, K.K. Raina and Chandra Prakash, *Ferroelectric Letters (Accepted).*

6. *Effect of Sm Substitution on Structural, Dielectric and Ferroelectric Properties of Lead Zirconate Titanate and Nickel Zinc Ferrite Composites*, **Rekha Rani**, J.K. Juneja, Sangeeta Singh, K.K. Raina and Chandra Prakash, *Ceramics International (Communicated).*

7. *Dielectric, Ferroelectric and Ferromagnetic Properties of $xNi_{0.8}Zn_{0.2}Fe_2O_4$-(1-x) $Pb_{0.99}La_{0.02}Zr_{0.65}Ti_{0.35}O_3$ Composites*, **Rekha Rani**, Sangeeta Singh, J.K. Juneja, K.K. Raina and Chandra Prakash, *Journal of Alloys & Compounds (Communicated).*

8. *Dielectric, Ferroelectric, Magnetic and Magnetoelectric Properties of 0.1$Ni_{0.8}Zn_{0.2}Fe_2O_4$-0.9$Pb_{1-3x/2}Sm_xZr_{0.65}Ti_{0.35}O_3$ Magnetoelectric Composites*, **Rekha Rani**, J.K. Juneja, Sangeeta Singh, K.K. Raina and Chandra Prakash, *Journal of Physics and Chemistry of Solids (Communicated).*

Other publications in Journals (not included in thesis)

9. *Ferroelectric Properties of Microwave Processed PZT-NiZn Ferrite Composites*, **Rekha Rani**, Parveen Kumar, Sangeeta Singh, J.K. Juneja, Chandra Prakash and K.K. Raina, *Integrated Ferroelectrics **122** (2010) 45*.

10. *Effect of Two-Stage Sintering on Dielectric Properties of $BaTi_{0.9}Zr_{0.1}O_3$ Ceramics*, **Rekha Rani**, Renu Rani, Parveen Kumar, J.K. Juneja, K.K. Raina and Chandra Prakash, *Phase Transitions **84** (2011) 843.*

11. *Study on Microwave Processed PZT:Ni-Zn Ferrite Magneto-Electric Composites*, **Rekha Rani**, J.K. Juneja, Sangeeta Singh, K.K. Raina and Chandra Prakash, *Journal of Ceramic Processing Research (Communicated).*

Full Papers in Conference Proceedings

12. *Study on Microwave Processed PZT-NZF Composite*, **Rekha Rani**, Sangeeta Singh, J.K. Juneja, Chandra Prakash and K.K. Raina, *National Conference on Recent Advances in Material Science, Dyal Singh College, Karnal, Feb 25-26, 2012.*

13. *Structural and Dielectric Study of $0.85Pb_{1-3x/2}La_xZr_{0.65}Ti_{0.35}O_3$–$0.15Ni_{0.8}Zn_{0.2}Fe_2O_4$,* Sangeeta Singh, **Rekha Rani**, J.K. Juneja, Chandra Prakash and K.K. Raina, *National Conference on Recent Advances in Material Science, Dyal Singh College, Karnal, Feb 25-26, 2012.*

14. *Investigations on Microwave Processed $0.1Ni_{0.8}Zn_{0.2}Fe_2O_4$-$0.9PbZr_{0.65}Ti_{0.35}O_3$ Composite*, **Rekha Rani**, Sangeeta Singh, J.K. Juneja, Chandra Prakash and K.K. Raina, *National Symposium on Materials and Processing, BARC, Mumbai, Oct 10-12, 2012.*

Papers presented in Conferences

(i) International Conferences

1. *Structural and Dielectric Properties of BST Ceramics Prepared by Microwave Processing*, Renu Dahiya, **Rekha Rani**, Parveen Kumar, Sangeeta Singh, J.K. Juneja, Chandra Prakash and K.K. Raina, *International Symposium on Nanostructured Materials: Structure, Properties, and Applications, Kanya Mahavidyalaya, Jalandhar, Punjab, Oct. 28-29, 2009.*

2. *Ferroelectric Properties of Microwave Processed PZT-NiZn Ferrite Composites*, **Rekha Rani**, Parveen Kumar, Sangeeta Singh, J.K. Juneja, Chandra Prakash and K.K. Raina, *International Conference on Electroceramics, University of Delhi, Delhi, Dec. 13-17, 2009.*

3. *Study on Microwave Processed PZT:Ni-Zn Ferrite Magneto-Electric Composites*, **Rekha Rani**, Pratibha Singh, Sangeeta Singh, J.K. Juneja, K.K. Raina and Chandra Prakash, *International Workshop & Symposium on the Synthesis and Characterization of Glass/Glass Ceramics, C-MET Pune, July 7-10, 2010.*

4. *Effect of Sm Substitution on Structural, Dielectric and Ferroelectric Properties of Lead Zirconate Titanate and Nickel Zinc Ferrite Composites*, **Rekha Rani**, K.K. Raina and Chandra Prakash, *International Conference on Electroceramics, University of New South Wales, Sydney, Australia, Dec. 12-16, 2011.*

5. *A Comparative Study of Conventionally Sintered and Microwave Sintered* $0.9PbZr_{0.65}Ti_{0.35}O_3$–$0.1Ni_{0.8}Zn_{0.2}Fe_2O_4$ *Composite*, **Rekha Rani**, Sangeeta Singh, J.K. Juneja, Chandra Prakash and K.K. Raina, *International Conference & Workshop on Nanostructured Ceramics & other Nanomaterials, University of Delhi, Delhi, March 13-16, 2012.*

(ii) National Conferences

6. Attended *National Seminar on Condensed Matter, High Energy and Nuclear Physics, Deptt. of Physics, JMI, New Delhi, March 23-24, 2009.*

7. *Dielectric Behavior of Microwave Sintered BST Ceramics*, Renu Rani, **Rekha Rani**, Parveen Kumar, Sangeeta Singh, J.K. Juneja, Chandra Prakash and K.K. Raina, *Recent Trends in Multifunctional Oxide Materials, Osmania University, Hyderabad, July 17-18, 2009.*

8. *A Comparative Study of Conventionally Sintered and Microwave Sintered PZT-NZF Composite*, **Rekha Rani**, Sangeeta Singh, J.K. Juneja, K.K. Raina and Chandra Prakash, *National Symposium on Microwave Processing of Materials, IIT Delhi, Nov 28, 2010.*

9. *Ferroelectric properties of La substituted PZT Ceramics*, **Rekha Rani**, J.K. Juneja, K.K. Raina and Chandra Prakash, *XVI-National Seminar on Ferroelectrics and Dielectrics, Deptt. of Pure & Applied Physics, GGV, Bilaspur, Dec. 2-4, 2010.*

10. *Dielectric Properties of PLZT-NZF Composites*, **Rekha Rani**, Sangeeta Singh, J.K. Juneja, Chandra Prakash and K.K. Raina, *National Seminar on Advanced Materials and Devices, GVM Girls College, Sonepat, July 3-4, 2011.*

11. *Studies on Dielectric Properties of PZT: NZF Composites*, **Rekha Rani**, Sangeeta Singh, J.K. Juneja, Chandra Prakash and K.K. Raina, *National Seminar on Advanced Materials and Devices, GVM Girls College, Sonepat, July 3-4, 2011.*

12. *Effect of La Substitution on Dielectric Properties of PZT-NZF Composite*, **Rekha Rani**, Sangeeta Singh, J.K. Juneja, Chandra Prakash and K.K. Raina, *National Symposium on Advanced Materials, Sharda University, Greater Noida, July 6 2011.*

13. *Structural and Dielectric Properties of* $Pb_{(1-3x/2)}La_xZr_{0.588}Ti_{0.392}Fe_{0.01}Nb_{0.01}O_3$ *Ferroelectric Ceramics*, **Rekha Rani**, Parveen Kumar, Pratibha Singh, J.K. Juneja, K.K. Raina and Chandra Prakash, *National Conference on Futuristic Materials, Sharda University, Greater Noida, Sep. 15-17, 2011.*

14. *Ferroelectric Properties of Rare Earth (La, Sm) Substituted PZT Ceramics*, **Rekha Rani**, Sangeeta Singh, J.K. Juneja, Chandra Prakash and K.K. Raina, *Functional Materials for Sustainable Energy and Advanced Technologies, Thapar University, Patiala, Feb. 13-15, 2012.*

15. *Effect of La Substitution on Structural, Dielectric and Magnetic Properties of Ferroelectric Rich 0.85PZT–0.15NZF Composite*, **Rekha Rani**, J.K. Juneja, Chandra Prakash and K.K. Raina, *National Conference on Functional Materials, GVM Girls College, Sonepat, Sep 24-25, 2012.*

Awards/Prize/Certificate

1. Paper entitled "*Study on Microwave Processed PZT:Ni-Zn Ferrite Magnetoelectric Composites*" was awarded **Best Oral Presentation Award** in *IWSSCGGC-2010 held on July 9-10, 2010 at Yashada MD Centre, Pune.*

CONTENTS

		Page No.
Certificate		i
Acknowledgements		ii
Abstract		iv
List of Publications		vii
Chapter I	**Introduction**	**1**
1.1	Ferroelectricity and Piezoelectricity in Crystals	1
1.1.1	An Introduction to Ferroelectricity	1
1.1.2	General Features of Ferroelectric Materials	2
1.1.3	An Introduction to Piezoelectricity	4
1.2	Magnetism	5
1.2.1	Classification of Magnetic Materials	5
1.2.1.1	Diamagnetic Materials	5
1.2.1.2	Paramagnetic Materials	6
1.2.1.3	Ferromagnetic Materials	7
1.2.1.4	Ferrimagnetic Materials	8
1.2.1.5	Antiferromagnetic Materials	9
1.2.2	Magnetic Hysteresis Loop	10
1.2.3	Magnetostriction	11
1.3	Magnetoelectric Materials	11
1.3.1	Single Phase Systems	12
1.3.2	Two Phase Systems (Composites)	13
1.3.3	Applications of Magnetoelectric Materials	15
1.3.4	Requirements for Materials to Exhibit ME Effect in Composites	16
1.4	Review of Literature on Ferrimagnetic–Ferroelectric (ME) Materials	17
1.5	Selection of Individual Phases	22
1.6	Objectives of Present Work	23
References		25

Chapter II Synthesis and Characterization Techniques **29**

2.1 Material Synthesis: Conventional Solid State Route 29

2.1.1 Raw Materials and Ball Milling 29

2.1.2 Calcination 32

2.1.3 Compaction of Powder (Shaping) 33

2.1.4 Sintering 34

2.1.4.1 Conventional Sintering (CS) 34

2.1.4.2 Microwave Sintering (MS) 34

2.2 Characterization Techniques 36

2.2.1 X–Ray Diffraction (XRD) 36

2.2.2 Density Measurements 38

2.2.3 Scanning Electron Microscope (SEM) 39

2.2.4 Electroding 40

2.2.5 Dielectric Measurements 40

2.2.6 AC Conductivity 42

2.2.7 P–E Hysteresis Loop Set–up 42

2.2.8 Poling 43

2.2.9 Piezoelectric Charge Coefficient 44

2.2.10 Vibrating Sample Magnetometer (M–H Hysteresis Loop Set–up) 45

2.2.11 Magnetoelectric (ME) Coupling 46

2.2.11.1 Using VSM 46

2.2.11.2 ME Set–up 47

References 48

Chapter III Characterization of NZF–PZT Composites **50**

3.1 Synthesis of Individual Phases 51

3.2 $0.1Ni_{0.8}Zn_{0.2}Fe_2O_4–0.9PbZr_{0.65}Ti_{0.35}O_3$: Processing Parameters and Optimization of Sintering Temperature 53

3.3 Synthesis and Characterization of $yNi_{0.8}Zn_{0.2}Fe_2O_4–(1–y)PbZr_{0.65}Ti_{0.35}O_3$ 57

3.3.1 X–Ray Diffraction 58

3.3.2 Scanning Electron Microscope 59

3.3.3 Dielectric Properties 61
3.3.4 Ferroelectric Properties 68
3.3.5 Piezoelectric Properties 70
3.3.6 Ferromagnetic Properties 71
3.3.7 Magnetoelectric Properties 72
References 76

Chapter IV Characterization of NZF–PLZT Composites 78
4.1 Synthesis of Individual Phases 79
4.2 Synthesis of $yNi_{0.8}Zn_{0.2}Fe_2O_4–(1–y)Pb_{1–3x/2}La_xZr_{0.65}Ti_{0.35}O_3$ 80
4.3 Characterization of $yNi_{0.8}Zn_{0.2}Fe_2O_4–(1–y)Pb_{1–3x/2}La_xZr_{0.65}Ti_{0.35}O_3$ 81
4.3.1 X–Ray Diffraction 81
4.3.2 Scanning Electron Microscope 82
4.3.3 Dielectric Properties 90
4.3.4 Ferroelectric Properties 101
4.3.5 Piezoelectric Properties 104
4.3.6 Ferromagnetic Properties 104
4.3.7 Magnetoelectric Properties 105
References 112

Chapter V Characterization of NZF–PSZT Composites 114
5.1 Synthesis of Individual Phases 114
5.2 Synthesis of $yNi_{0.8}Zn_{0.2}Fe_2O_4–(1–y)Pb_{1–3x/2}Sm_xZr_{0.65}Ti_{0.35}O_3$ 115
5.3 Characterization of $yNi_{0.8}Zn_{0.2}Fe_2O_4–(1–y)Pb_{1–3x/2}Sm_xZr_{0.65}Ti_{0.35}O_3$ 116
5.3.1 X–Ray Diffraction 116
5.3.2 Scanning Electron Microscope 116
5.3.3 Dielectric Properties 121
5.3.4. Ferroelectric Properties 127
5.3.5 Piezoelectric Properties 127
5.3.6 Ferromagnetic Properties 129
5.3.7 Magnetoelectric Properties 129

References 135

Chapter VI Characterization of Microwave Processed NZF–PZT Composites 137

6.1 X–Ray Diffraction 137

6.2 Scanning Electron Microscope 138

6.3 Dielectric Properties 140

6.4 Ferroelectric Properties 145

6.5 Ferromagnetic Properties 147

6.6 Magnetoelectric Properties 148

References 151

Chapter VII 152

7.1 Summary 152

7.2 Recommendations for Future Work 154

LIST OF FIGURES

		Page No.
Chapter I	**Introduction**	**1**
Figure 1.1	Ferroelectric (P–E) hysteresis curve	3
Figure 1.2	Diamagnetic materials	6
Figure 1.3	Paramagnetic materials	7
Figure 1.4	(a) Ferromagnetic (b) Ferrimagnetic and (c) Antiferromagnetic ordering	8
Figure 1.5	Unit cell of a magnetic spinel	9
Figure 1.6	Ferromagnetic/ferrimagnetic (B–H) hysteresis loop	10
Figure 1.7	Change in lattice dimension under an applied external magnetic field	11
Figure 1.8	Stress–mediated magnetoelectric effect	13
Figure 1.9	Stress–mediated product property	14
Chapter II	**Synthesis and Characterization Techniques**	**29**
Figure 2.1	Solid state route for synthesis of (a) individual phases and (b) composites	30
Figure 2.2	The schematic of planetary ball milling	31
Figure 2.3	Planetary ball mill	31
Figure 2.4	Programmable furnace for calcination and sintering	32
Figure 2.5	Hydraulic press	33
Figure 2.6	Microwave furnace	35
Figure 2.7	Temperature–time graph for conventional and microwave sintering	36
Figure 2.8	Bragg's law for reflection	37
Figure 2.9	Agilent 4284A LCR meter	41
Figure 2.10	Sawyer–Tower circuit	42
Figure 2.11	P–E hysteresis loop tracer	43
Figure 2.12	Set–up for electric poling	44
Figure 2.13	Piezo d_{33} meter	45
Figure 2.14	Schematic for vibrating sample magnetometer	46

Chapter III	**Characterization of NZF–PZT Composites**	**50**
Figure 3.1	XRD patterns for (a) NZF and (b) PZT	52
Figure 3.2	XRD patterns for 0.1NZF–0.9PZT composite at different sintering temperatures	54
Figure 3.3	Comparison of temperature dependence of dielectric constant (ε') and loss (tanδ) of 0.1NZF–0.9PZT composite for different sintering temperatures at 100 kHz	55
Figure 3.4	P–E hysteresis loops of 0.1NZF–0.9PZT composite samples at different sintering temperatures	56
Figure 3.5	M–H hysteresis loops of 0.1NZF–0.9PZT composite samples at different sintering temperatures	57
Figure 3.6	XRD patterns for yNZF–(1–y)PZT (a) y = 0 (b) y = 0.05 (c) y = 0.10 (d) y = 0.15 and (e) y = 1 at room temperature	58
Figure 3.7	SEM micrographs for yNZF–(1–y)PZT (a) y = 0 (b) y = 0.05 (c) y = 0.10 (d) y = 0.15 and (e) y = 1	60
Figure 3.8	Temperature dependence of ε' and tanδ for PZT (y = 0), NZF (y = 1) and NZF–PZT composites (y = 0.05, 0.10 and 0.15) at 1, 10 and 100 kHz	63
Figure 3.9	Temperature dependence of dielectric properties for yNZF–(1–y)PZT (y = 0, 0.05, 0.10 and 0.15) at 100 kHz	65
Figure 3.10	Frequency dependence of dielectric properties for yNZF–(1–y)PZT (y = 0, 0.05, 0.10 and 0.15) at 100 kHz at room temperature	66
Figure 3.11	Variation of AC conductivity with frequency for yNZF–(1–y)PZT (y = 0, 0.05, 0.10 and 0.15) at 100 kHz	67
Figure 3.12	Room temperature P–E hysteresis loops for (a) y = 0 (b) y = 0.05 (c) y = 0.10 and (d) y = 0.15 at different maximum electric fields (e) comparison of P–E loops for y = 0, 0.05 and 0.10 at 25 kV	69
Figure 3.13	Variation of (a) P_r (b) P_s and (c) E_c with maximum applied electric field for y = 0, 0.05 and 0.10	70
Figure 3.14	M–H hysteresis curve (a) y = 0.05 (b) y = 0.10 (c) y = 0.15 and (d) y = 1	72
Figure 3.15	(a) Comparison of M–H loops for y = 0.05, 0.10 and 0.15, M–H loops	73

	for electrically poled and unpoled samples for (b) y = 0.05 (c) y = 0.10 and (d) y = 0.15	
Figure 3.16	Variation of ME coupling coefficient, α (mV/(cm.Oe)) with DC magnetic field for y = 0.05, 0.10 and 0.15	75
Chapter IV	**Characterization of NZF–PLZT Composites**	**78**
Figure 4.1	XRD patterns for PLZT calcined samples (x = 0, 0.01, 0.02 and 0.03)	80
Figure 4.2	XRD patterns for all samples of series 2A	83
Figure 4.3	XRD patterns for all samples of series 2B	83
Figure 4.4	XRD patterns for all samples of series 2C	84
Figure 4.5	XRD patterns for all samples of series 2D	84
Figure 4.6	SEM micrographs for all samples of series 2A	86
Figure 4.7	SEM micrographs for all samples of series 2B	87
Figure 4.8	SEM micrographs for all samples of series 2C	88
Figure 4.9	SEM micrographs for all samples of series 2D	89
Figure 4.10	Variation of dielectric constant (ε') and loss (tanδ) with temperature for the samples of series 2A (x = 0.01, 0.02 and 0.03) at 1, 10 and 100 kHz	93
Figure 4.11	Variation of dielectric constant (ε') and loss (tanδ) with temperature for the samples of series 2B (x = 0.01, 0.02 and 0.03) at 1, 10 and 100 kHz	94
Figure 4.12	Variation of dielectric constant (ε') and loss (tanδ) with temperature for the samples of series 2C (x = 0.01, 0.02 and 0.03) at 1, 10 and 100 kHz	95
Figure 4.13	Variation of dielectric constant (ε') and loss (tanδ) with temperature for the samples of series 2D (x = 0.01, 0.02 and 0.03) at 1, 10 and 100 kHz	96
Figure 4.14	Variation of dielectric constant (ε') and loss (tanδ) with frequency for all samples of series 2A at room temperature	97
Figure 4.15	Variation of dielectric constant (ε') and loss (tanδ) with frequency for all samples of series 2B at room temperature	98
Figure 4.16	Variation of dielectric constant (ε') and loss (tanδ) with frequency for all samples of series 2C at room temperature	99
Figure 4.17	Variation of dielectric constant (ε') and loss (tanδ) with frequency for all samples of series 2D at room temperature	100

Figure 4.18	Room temperature P–E hysteresis loop for all samples of series 2A (x = 0, 0.01, 0.02 and 0.03) at 20 Hz	102
Figure 4.19	Room temperature P–E hysteresis loop for all samples of series 2B (x = 0, 0.01, 0.02 and 0.03) at 20 Hz	102
Figure 4.20	Room temperature P–E hysteresis loop for all samples of series 2C (x = 0, 0.01, 0.02 and 0.03) at 20 Hz	103
Figure 4.21	Room temperature P–E hysteresis loop for samples of series 2D (x = 0.01) at 20 Hz	103
Figure 4.22	M–H hysteresis loop for all samples of series 2B at room temperature	106
Figure 4.23	M–H hysteresis loop for all samples of series 2C at room temperature	107
Figure 4.24	M–H hysteresis loop for all samples of series 2D at room temperature	108
Figure 4.25	M–H hysteresis loops for electrically poled and unpoled samples with x = 0.02 and y = 0.05, 0.10, 0.15 at room temperature	109
Figure 4.26	Variation of ME coupling coefficient, α (mV/(cm.Oe)) with DC magnetic field for series 2C	110
Chapter V	**Characterization of NZF–PSZT Composites**	**114**
Figure 5.1	XRD patterns for PSZT calcined samples (x = 0.01, 0.02 and 0.03)	115
Figure 5.2	XRD patterns for all samples of series 3A	118
Figure 5.3	XRD patterns for all samples of series 3B	118
Figure 5.4	SEM micrographs for the samples of series 3A (x = 0, 0.01 and 0.03)	119
Figure 5.5	SEM micrographs for the samples of series 3B (x = 0, 0.01 and 0.03)	120
Figure 5.6	Variation of dielectric constant (ε') and loss (tanδ) with temperature for the samples of series 3A (x = 0.01, 0.02 and 0.03) at 1, 10 and 100 kHz	123
Figure 5.7	Variation of dielectric constant (ε') and loss (tanδ) with temperature for the samples of series 3B (x = 0.01, 0.02 and 0.03) at 1, 10 and 100 kHz	124
Figure 5.8	Variation of dielectric constant (ε') and loss (tanδ) with frequency for all samples of series 3A at room temperature	125
Figure 5.9	Variation of dielectric constant (ε') and loss (tanδ) with frequency for all samples of series 3B at room temperature	126
Figure 5.10	Room temperature P–E hysteresis loop for all samples of series 3A (x =	128

0, 0.01, 0.02 and 0.03) at 20 Hz

Figure 5.11 Room temperature P–E hysteresis loop for all samples of series 3B (x = 0, 0.01, 0.02 and 0.03) at 20 Hz 128

Figure 5.12 M–H hysteresis loop for all samples of series 3A at room temperature 130

Figure 5.13 M–H hysteresis loop for all samples of series 3B at room temperature 131

Figure 5.14 M–H hysteresis loops for electrically poled and unpoled samples with x = 0.02 and y = 0.05 at room temperature 132

Figure 5.15 Variation of ME coupling coefficient, α (mV/(cm.Oe)) with DC magnetic field for all samples of series 3B 133

Chapter VI Characterization of Microwave Processed NZF–PZT Composites 137

Figure 6.1 XRD patterns for MS NZF–PZT samples (y = 0, 0.10 and 1) at room temperature 138

Figure 6.2 SEM micrographs for CS and MS NZF–PZT samples (y = 0, 0.10 and 1) 139

Figure 6.3 Temperature dependence of dielectric constant (ε') for MS NZF–PZT samples (y = 0, 0.05, 0.10, 0.15 and 1) at 1, 10 and 100 kHz 142

Figure 6.4 Comparison of temperature dependence of dielectric constant (ε') and loss (tanδ) for CS and MS NZF–PZT samples (y = 0, 0.05, 0.10, 0.15 and 1) at 100 kHz 143

Figure 6.5 Room temperature P–E hysteresis loops for CS and MS NZF–PZT samples (y = 0, 0.05 and 0.10) 146

Figure 6.6 Room temperature M–H hysteresis loops for CS and MS samples (y = 0.05, 0.10, 0.15 and 1) 148

Figure 6.7 Room temperature M–H hysteresis loops for electrically poled and unpoled MS sample with y = 0.10 (series 4) 149

Figure 6.8 Variation of ME coupling coefficient, α (mV/(cm.Oe)) with DC magnetic field for CS and MS sample with y = 0.10 150

LIST OF TABLES

Chapter III	**Characterization of NZF–PZT Composites**	**50**
Table 3.1	Structural parameters of 0.1NZF–0.9PZT composite at different sintering temperatures	55
Table 3.2	Dielectric and piezoelectric parameters of 0.1NZF–0.9PZT at 100 kHz	56
Table 3.3	Structural parameters of $yNi_{0.8}Zn_{0.2}Fe_2O_4$–$(1–y)PbZr_{0.65}Ti_{0.35}O_3$	61
Table 3.4	Variation of T_c, ε'_{RT}, ε'_{max}, $\tan\delta_{RT}$ and $\tan\delta_{max}$ for different values of y at 100 kHz	65
Table 3.5	Piezoelectric, magnetic and magnetoelectric parameters for yNZF–(1–y)PZT (y = 0, 0.05, 0.10 and 0.15)	75
Chapter IV	**Characterization of NZF–PLZT Composites**	**78**
Table 4.1	Structural parameters for NZF–PLZT samples	85
Table 4.2	Dielectric parameters for NZF–PLZT samples at 100 kHz	92
Table 4.3	Values of P_r, E_c, M_r, M_s, H_c, d_{33} and α for NZF–PLZT samples	111
Chapter V	**Characterization of NZF–PSZT Composites**	**114**
Table 5.1	Structural parameters for NZF–PSZT samples	117
Table 5.2	Dielectric parameters for NZF–PSZT samples at 100 kHz	122
Table 5.3	Values of P_r, E_c, M_r, M_s, H_c, d_{33} and α for NZF–PSZT samples	134
Chapter VI	**Characterization of Microwave Processed NZF–PZT Composites**	**137**
Table 6.1	Structural parameters for NZF–PZT samples	140
Table 6.2	Dielectric parameters for NZF–PZT samples at 100 kHz	141
Table 6.3	Ferroelectric parameters for NZF–PZT samples at 20 Hz	145
Table 6.4	Ferromagnetic parameters for NZF–PZT samples	147

Chapter-I

Introduction

Chapter–I

Introduction

Magnetoelectric materials consisting of both ferromagnetic/ferrimagnetic and ferroelectric phases have been the focus of scientists due to their potential applications in many multifunctional devices such as magnetic field sensors, filters, oscillators, phase shifters, multiple state memory elements, transducers and electro–optic devices etc. The area of magnetoelectric materials has attracted researchers from both groups, Ferroelectricity and Magnetism, because it exploits both ferroelectric and magnetic properties of matter. These materials show magnetoelectric (ME) effect which is a coupled two field effect i.e. induced magnetization as a response to an applied electric field or induced polarization by applying an external magnetic field.

The present work aims at the synthesis and characterization of ferrite–ferroelectric (NiZn ferrite–PZT) composites. In this context, some basic concepts of ferroelectricity and magnetism are discussed in this chapter.

1.1 Ferroelectricity and Piezoelectricity in Crystals

1.1.1 An Introduction to Ferroelectricity

Ferroelectricity is defined as electrically switchable polarization in crystals. Ferroelectricity was reported for the first time by Joseph Valasek, who worked at the University of Minnesota in Minneapolis, in his work "Piezoelectricity and Allied Phenomenon in Rochelle Salt" in 1920 [1–3]. Before 1940, only two types of ferroelectric materials were known, Rochelle salt and potassium dihydrogen phosphate. In the early 1940's, the discovery of barium titanate ($BaTiO_3$) ceramic, first ferroelectric material without hydrogen bonds, led to the discovery of a large number of similar perovskite viz. $KNbO_3$, $LiNbO_3$, $PbTiO_3$ etc. During mid–1940's there has been a continuous succession of new materials and technology developments that have led to

a significant number of applications such as high dielectric constant capacitors, transducers, filters, buzzers, gas ignitors, positive temperature coefficient (PTC) sensors and switches, thin film capacitors and ferroelectric memories [4–7].

1.1.2 General Features of Ferroelectric Materials

The materials exhibiting the phenomenon of ferroelectricity are called ferroelectric materials. A ferroelectric crystal exhibits an electric dipole moment even in the absence of an external electric field. In the ferroelectric state, the centre of positive charge of the crystal does not coincide with the centre of the negative charge [8]. Usually at a well–defined temperature, there is a change in the structure of the crystal. This temperature is called ferroelectric Curie temperature (T_c) and this change is known as phase transition. When the temperature increases through the Curie temperature, the ferroelectric crystal undergoes a structural phase transition from a ferroelectric phase to a paraelectric phase. Dielectric constant has the maximum value at Curie temperature. In most ferroelectrics, the temperature dependence of the dielectric constant above the Curie temperature ($T>T_c$), can be described using Curie–Weiss law:

$$\varepsilon' = \frac{C}{T - T_o} \qquad \ldots. (1.1)$$

Where ε is the dielectric constant, C is Curie constant and T_o is the Curie–Weiss temperature, which defines the paraelectric phase. The Curie–Weiss temperature T_o is different from the Curie temperature T_c. For first order transitions, $T_o<T_c$ while for second order phase transitions, $T_o = T_c$ [9–10].

Ferroelectric materials also exhibit hysteresis properties and there is evidence for the existence of domains in them. These ferroelectric domains are the regions of uniformly oriented spontaneous polarization within the material. In general, the direction of spontaneous polarization is not the same throughout a microscopic crystal. Rather the crystal consists of a number of domains and within each domain, the polarization has a specific direction, but this direction varies from one domain to another domain. Ferroelectric hysteresis loop property is

measured by the behavior of polarization reversal or switching [11] in a ferroelectric material, shown in figure 1.1.

The hysteresis loop can be observed experimentally by using a Sawyer–Tower circuit [12]. The starting point is assumed to be at O (figure 1.1). As the electric field strength is increased, the domain starts to align in the positive direction, giving rise to rapid increase in the polarization. At very high field levels, the polarization saturates. When the field strength starts decreasing, some domains will reverse but polarization does not fall to zero when the applied field is reduced to zero. Some of the domains remains aligned in the positive direction and the crystal show a remanant polarization P_r (OD). The field required to bring the polarization to zero is called the coercive field strength, E_c. If the field is increased to more negative value, the direction of polarization flips and a hysteresis loop is obtained. The spontaneous polarization P_s (OE) is usually taken as the intercept of the polarization axis with the extrapolated linear segment BC [13]. In polycrystalline materials, true spontaneous polarization equal to that of a single crystal can never be reached and hence it is more correct to speak of saturated rather than of spontaneous polarization [14]. The coercive field, spontaneous and saturation polarizations and shape of the loop are affected by a number of factors including thickness, presence of charged defects, mechanical stresses, preparation conditions, pinning centers and measurement temperatures [9, 15].

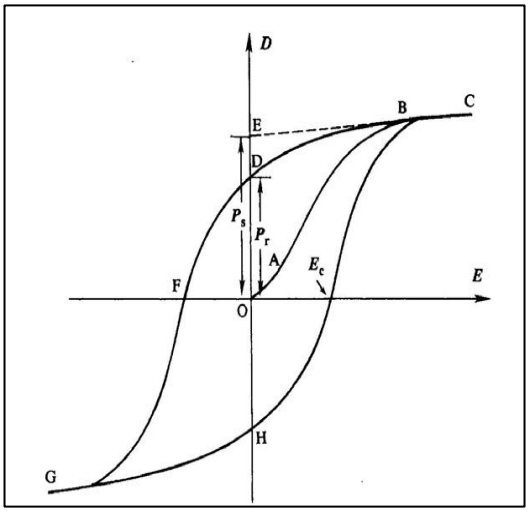

Figure 1.1 Ferroelectric (P–E) hysteresis curve

1.1.3 An Introduction to Piezoelectricity

Piezoelectricity was discovered in 1880 by Jacques and Pierre Curie during their study of the effect of pressure on the generation of electrical charge by crystals such as quartz and tourmaline. A piezoelectric material develops a potential across its boundaries when subjected to a mechanical stress (direct piezoelectric effect) and such materials can be used to make sensors. Conversely, by applying an electric field to the material, a mechanical deformation occurs (converse piezoelectric effect). This property is exploited to make actuators. The piezoelectric effect in a crystal results from the displacement of ionic charges within a crystal structure. In the absence of the external stress, the charge distribution within the crystal is symmetric and net electric dipole moment is zero. When an external stress is applied, displacement of charges will take place and a net polarization develops which results in an internal electric field.

When a piezoelectric material is subjected to stress, electric charge generated per unit force is called piezoelectric charge coefficient and is denoted by 'd'. This property is directional e.g. d_{31} indicates that piezoelectric charge coefficient is related to the generation of polarization in the electrode perpendicular to direction 3 or vertical direction and to the stress mechanically applied in direction 1 or lateral direction; d_{33} indicates the polarization generated in the direction 3 when the stress is applied in the direction 3. The d coefficients are usually measured in pC/N. In addition to the d coefficients, piezoelectric voltage coefficient (g) relates the electrical field produced by mechanical stress. It is used to measure the field produced by the stress in piezoelectric ceramics.

The g constant is related to the d constant via relationship:

$$g = \frac{d}{\varepsilon' . \varepsilon_o} \qquad \ldots. (1.2)$$

Where ε' and ε_o are the dielectric constant of the material and permittivity of the free space, respectively.

In addition to d and g, there is electromechanical coupling factor 'k' which gives us the measure of the part of the applied electrical energy converted into mechanical energy or vice–versa and measured by resonance method [16].

$$k^2 = \frac{\text{Mechanical energy converted into electrical energy}}{\text{input mechanical energy}} \quad \ldots. (1.3)$$

There exist various electromechanical coupling factors e.g. k_p, k_t and k_{31} depending on the mode of energy conversion. Here, k_p is planar coupling coefficient, related to the energy conversion, when the applied electric field is perpendicular to the generated mechanical vibrations which are along the plane. k_t is the thickness coupling factor related to the energy conversion when the applied electric field is in the direction of generated mechanical vibrations and which are along the thickness in the material. The ferroelectric ceramics do not possess any piezoelectric property due to random orientation of the ferroelectric domains in the ceramics. For domain reorientation, a field must be applied on the sample and maintained for certain time to force the domains to reorient in the direction of the applied electric field (the process is called poling). After poling, remanant polarization and remanant strain are maintained within the material and it starts exhibiting piezoelectric effect [9].

1.2 Magnetism

Magnetism is the property of materials by virtue of which they respond to an applied magnetic field. Its origin lies in the orbiting electrons and their spin motions. Magnetism in materials also depends on the electrons interactions with each other. Most of the free atoms have net total angular momentum and hence have net magnetic moments. But in all the molecules or solids, net angular momentum is always zero except in the case of three transition series which possess a resultant magnetic moment because of the presence of unpaired d electrons.

1.2.1 Classification of Magnetic Materials

1.2.1.1 Diamagnetic Materials

These materials are composed of atoms which have zero magnetic moments. When an external magnetic field is applied, a negative magnetization is produced. Hence, these materials have very small negative susceptibilities (~ 10^{-6}). M vs H plot and susceptibility dependence on

temperature for these materials is shown in figure 1.2 (a) and (b). Some examples are inert gases, hydrogen, quartz, calcite, many organic compounds etc.

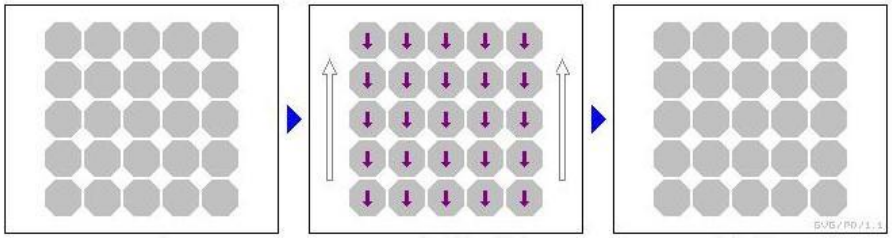

before the field is applied magnetic field applied magnetic field removed

(a)

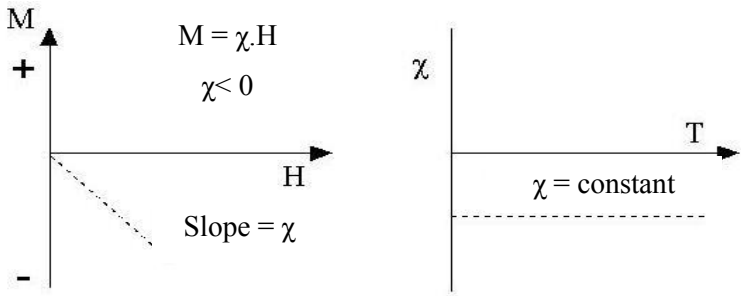

(b)

Figure 1.2 Diamagnetic materials

1.2.1.2 Paramagnetic Materials

These materials are composed of atoms which have a permanent magnetic moment arising due to spin and orbital motion of electrons. An external magnetic field tends to align the moments in the direction of field, resulting in net positive magnetization. The susceptibilities are therefore positive but small (~ 10^{-3} – 10^{-6}). When field is removed, magnetization is zero like diamagnetic materials. They obey Curie's law (i.e. alignment of moments in an external field is

opposed by the disordering effects of temperature). M vs H plot and susceptibility dependence on temperature for these materials is shown in figure 1.3 (a) and (b). Examples are pyrite, biotite, compounds containing transition metal ions etc.

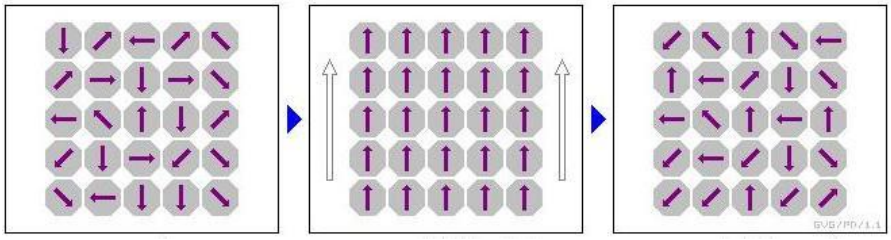

before the field is applied magnetic field applied magnetic field removed

(a)

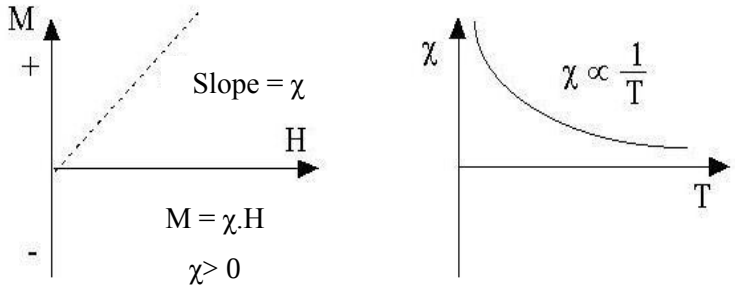

(b)

Figure 1.3 Paramagnetic materials

1.2.1.3 Ferromagnetic Materials

These materials are composed of atoms having net magnetic moments with very strong interactions produced by electronic exchange forces. It results in the parallel or antiparallel alignment of uncompensated electron spins i.e. these materials are spontaneously magnetized (below Curie temperature) as shown in the figure 1.4(a).

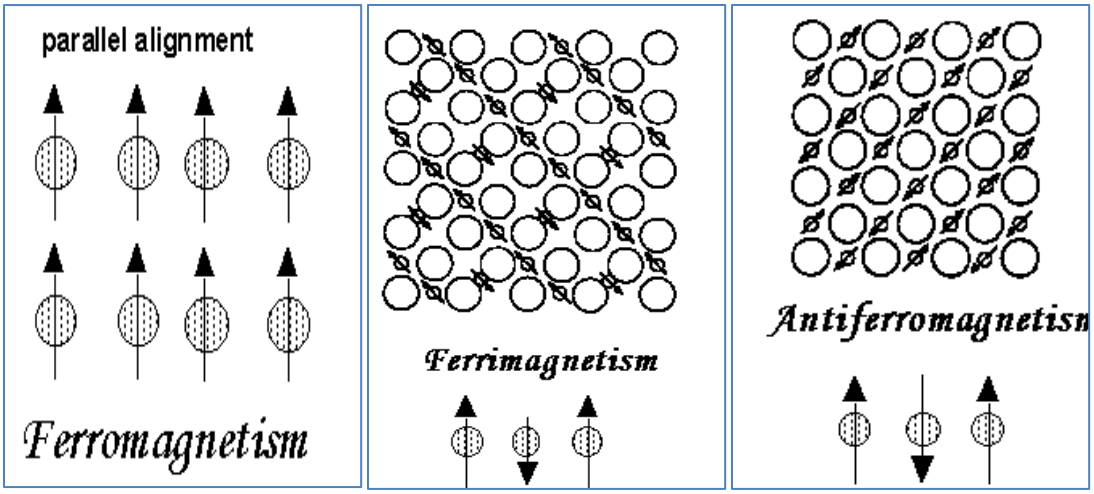

(a) (b) (c)

Figure 1.4 (a) Ferromagnetic (b) Ferrimagnetic and (c) Antiferromagnetic ordering

There is no spontaneous magnetization in those ferromagnetic materials which have not been exposed to an external magnetic field because of the formation of microscopic volumes (domains), each having its own direction of magnetization. In their lowest energy state, domains are so oriented that spontaneous magnetization is zero. Other related term is the saturation magnetization; maximum induced magnetic moment in an external magnetic field (no further increase in magnetization beyond this). Although exchange forces are very large in ferromagnetic materials, thermal energy eventually overcomes these forces and produces a disordering effect, at a particular temperature called Curie temperature. Some examples are Fe, Ni, Co and their alloys etc.

1.2.1.4 Ferrimagnetic Materials

These materials have structures composed of two magnetic sub–lattices (A and B) separated by oxygens and there is antiferromagnetic coupling between cations occupying different crystallographic sites. The magnetization of one sub–lattice is antiparallel to that of another sub–lattice and is of unequal strength resulting in a net spontaneous magnetization similar to ferromagnetic materials (figure 1.4(b)). With increase in temperature, the spontaneous

magnetization decreases and reaches to zero at a particular temperature called Neel temperature (T_N).

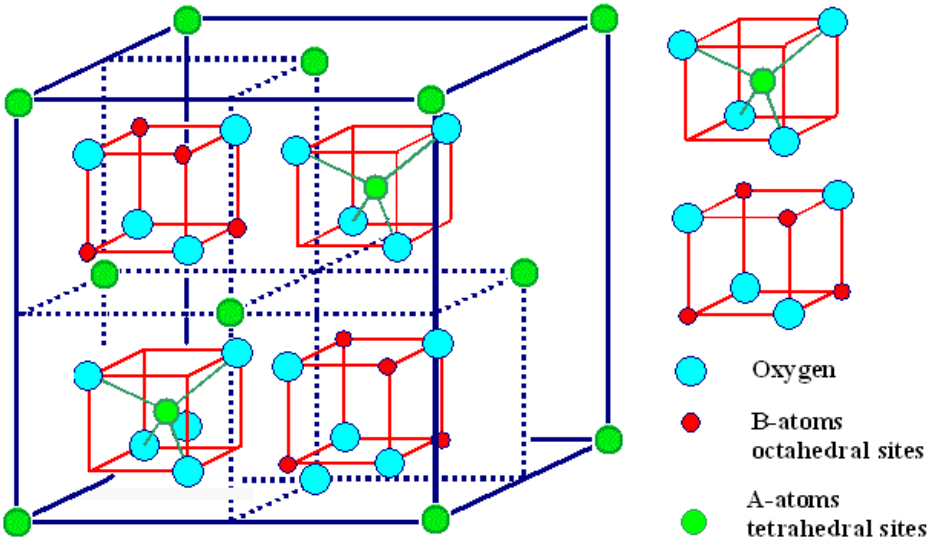

AB_2O_4 spinel The red cubes are also contained in the back half of the unit cell

Figure 1.5 Unit cell of a magnetic spinel

Example is magnetite (Fe_3O_4), naturally occurring ferrite having spinel structure. In this structure, oxygen ions form a cubic close packed arrangement with Fe ions filled in two types of interstitial sites: tetrahedral and octahedral. Unit cell of spinel structure has 8 formula units, 64 tetrahedral sites and 32 octahedral sites designated as A and B sites, respectively. Out of these, 8 tetrahedral and 16 octahedral sites are occupied. The unit cell is shown in figure 1.5. The spins on the two sub–lattices (A and B) are antiparallel to each other, illustrating the antiferromagnetic coupling.

1.2.1.5 Antiferromagnetic Materials

These materials have structures composed of two magnetic sub–lattices and the magnetization of one sub–lattice is antiparallel to that of another sub–lattice in such a way that their magnetizations neutralize one another and overall magnetization is zero (shown in figure

1.4(c)). Examples are Mn, Cr and many transition metal oxides. They have low susceptibility values (~ 10^{-3}) and at temperature called Neel temperature, antiferromagnetic coupling breaks down and they become paramagnetic.

1.2.2 Magnetic Hysteresis Loop

Ferromagnetic/ferrimagnetic materials exhibit hysteresis properties (B vs H or M vs H loop). When such material is magnetized in one direction, it does not relax back to zero magnetization when the imposed magnetizing field is removed. It must be driven back to zero by a field in the opposite direction. If an alternating magnetic field is applied to the material, its magnetization will trace out a loop called a hysteresis loop. The lack of retraceability of the magnetization curve is the property called hysteresis and it is related to the existence of magnetic domains in the material. Once the magnetic domains are reoriented, it takes some energy to turn them back again. A great deal of information can be learned about the magnetic properties of a material by studying its hysteresis loop. Typical B–H hysteresis loop is shown in figure 1.6.

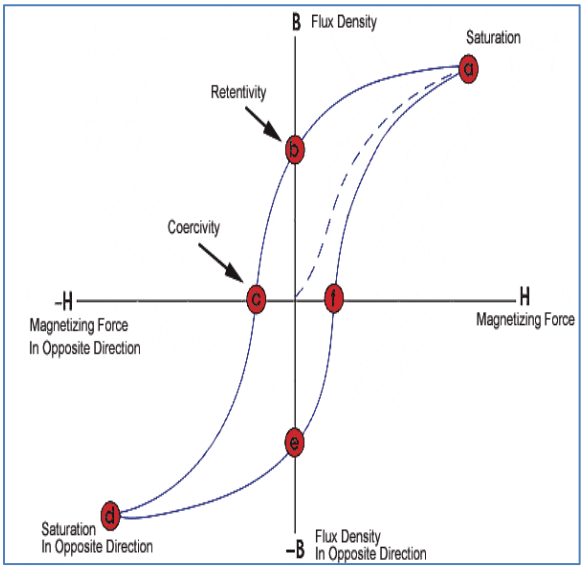

Figure 1.6 Ferromagnetic/ferrimagnetic (B–H) hysteresis loop

1.2.3 Magnetostriction

Ferromagnetic/ferrimagnetic materials change their shape/dimensions during the process of magnetization because of the spin–orbit coupling of electrons. Whenever there is a change in the spin direction, it results in a change in orbits orientation which slightly affects the lattice dimensions as shown in figure 1.7. This effect is known as magnetostriction. Variation in magnetization of material by applying external magnetic field always changes this magnetostrictive strain (due to change in dimensions) until it reaches to a saturation value, λ called magnetostriction coefficient. It can also be defined as strain induced by saturating field. If the external field causes an increase in dimensions in the direction of field, it is taken with positive sign otherwise negative.

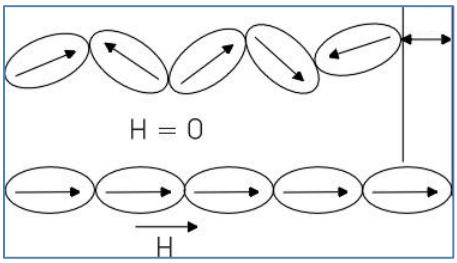

Figure 1.7 Change in lattice dimension under an applied external magnetic field

1.3 Magnetoelectric Materials

There are innumerable materials that show ferroelectric properties or ferromagnetic properties but in recent years, materials having coexistence of ferroelectricity and magnetism, simultaneously, have been drawing increasing interest due to multifunctional behavior. Simultaneous existence of these properties is well reported in literature for single phase as well as composite materials [17–21]. The magnetoelectric effect in these materials is defined as an induced electric polarization in external magnetic field or an induced magnetization in external electric field. This coupling of polarization, P, with magnetization, M, can be exploited for a number of multifunctional applications and is called magnetoelectric coupling. In 1894, it was P. Curie's idea that gave first breath to such coupling on the basis of symmetry considerations [22].

In 1888, Rontgen discovered magnetization of a moving dielectric in an electric field and seventeen years later, a reverse effect was also observed i.e., polarization of a moving dielectric in a magnetic field [23]. These magnetoelectric materials are classified into two groups: Single phase and two phase (composites) systems.

1.3.1 Single Phase Systems

In single phase systems, materials have coexistence of ferroelectric and magnetic orders in single phase and exhibit direct magnetoelectric coupling. Landau's free energy expression for linear magnetoelectric effect in single phase systems in terms of applied electric field (E) and magnetic field (H) is given by:

$$F(E, H) = F_o - \alpha_{ij} E_i H_j \quad \ldots. (1.4)$$

The subscripts i, j and k are the three directions of a cartesian coordinate system.

F_o is the free energy for E = H = 0 and α_{ij} is linear ME coefficient that corresponds to induction of polarization by a magnetic field or induction of magnetization by an electric field. Derivative of this free energy F(E, H) with respect to E_i (H_j) gives the polarization P_i (Magnetization M_j) in terms of applied field $H_j(E_i)$ as shown below:

$$P_i = -\frac{\partial F}{\partial E_i} = \alpha_{ij} H_j \quad \ldots. (1.5(a))$$

$$M_j = -\frac{\partial F}{\partial H_j} = \alpha_{ij} E_i \quad \ldots. (1.5(b))$$

For nonlinear (higher order) magnetoelectric effects, the free energy expression contains terms that are non–linear in E and H.

$$F(E,H) = F_o - \alpha_{ik} E_i H_k - \frac{1}{2}\beta_{ijk} E_i H_j H_k - \frac{1}{2}\gamma_{ijk} H_i E_j E_k \quad \ldots. (1.6)$$

Though the experimental evidences of ME effect in single phase systems were observed in the first half of 20^{th} century but the materials showing ME coupling were found to be rare. The

limiting factors which restrict the coexistence of ferroelectricity and magnetism in single phase are given below;

- Out of 122 Shubnikov point groups, 31 point groups allow spontaneous electric polarization and 31 allow spontaneous magnetization. However, there are only 13 point groups (1, 2, 2', m, m', 3, 3m', 4, 4m'm', m'm2', m'm'2', 6 and 6m'm') that allow both spontaneous electric polarization and spontaneous magnetization simultaneously in single phase [24].
- The coexistence of ferroelectric and magnetic ordering in single phase is hampered due to the effect of electron occupancy in d–orbitals. In conventional ferroelectrics like PZT, $BaTiO_3$ etc., the ferroelectricity is due to off centre displacement of Ti ion which is possible only with an empty d–orbital. However, for magnetic ordering, d–orbital should be partially filled. Therefore, different mechanism of ferroelectricity is necessary to get magnetoelectric coupling [25].

1.3.2 Two Phase Systems (Composites)

To enhance magnetoelectric coupling coefficients (many orders of magnitude larger than in single phase systems), idea of indirect coupling between ferroelectricity and magnetism was introduced for two phase systems [26]. This indirect coupling takes place via stress and results in magnetostriction induced deformation and the generation of piezoelectric charge [27–29] i.e. one phase should be magnetostrictive or piezomagnetic and other should be piezoelectric or electrostrictive. This stress mediated magnetoelectric coupling is shown in figure 1.8.

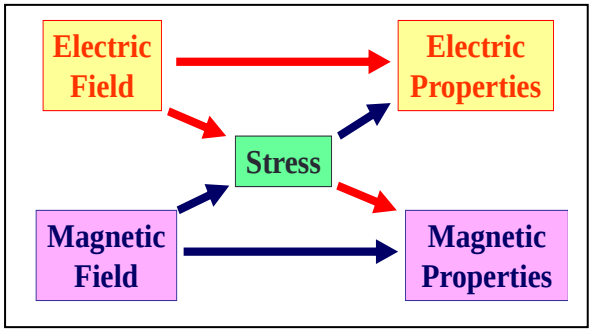

Figure 1.8 Stress–mediated magnetoelectric effect

This effect in two phase systems is analyzed from concept of product properties introduced by Van Suchetelene [30]. Figure 1.9 and equation 1.7 show the schematic representation of ME effect in two phase systems (composites) utilizing the product property [31].

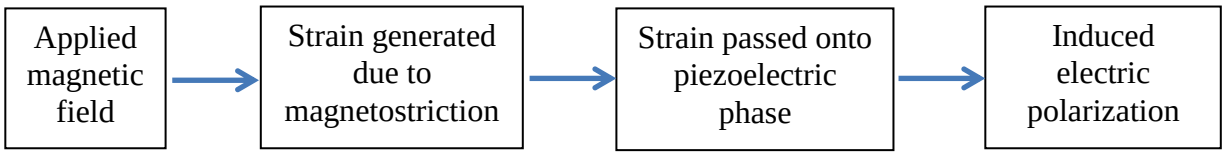

Figure 1.9 Stress–mediated product property

$$\alpha_E = \frac{\delta E}{\delta H} = \left(\frac{\delta E}{\delta z}\right) \cdot \left(\frac{\delta z}{\delta H}\right) \quad \ldots. (1.7)$$

Where,

$\alpha_E = \frac{\delta E}{\delta H}$ = ME coefficient

$\frac{\delta E}{\delta z}$ = Piezoelectric field generation

$\frac{\delta z}{\delta H}$ = Magnetostriction deformation

This can be obtained in the form of laminates, composites or epitaxial layers [32, 33]. All of these exhibit ME response with varying degree of magnitude which depends on the nature of phases (amorphous, ceramic, metal, polymer etc.), shapes of composites (disk, cylinder, plate, sphere, toroid etc.), sizes (number of layers, thickness, length and width of layers), number of connectivity patterns and choices of materials depending on magnetostriction coefficient, piezoelectric strain, permeability, permittivity, resistivity, sintering temperature and chemical reactivity etc. [34].

For n phases, the number of connectivity patterns is given by the formula:

$$\frac{(n+3)!}{n!3!} \quad \text{.... (1.8)}$$

For two phase systems (n = 2), it comes out to be 10.

Usually a combination of ferroelectric and ferrimagnetic materials has been used for studying this effect. The most widely studied systems that have been reported correspond to substituted $NiFe_2O_4$, $CoFe_2O_4$, $MnFe_2O_4$, $ZnFe_2O_4$, Terfenol ferrites with substituted PZT, PMN–PT, PVDF and $BaTiO_3$ [35]. For the present work, composites of substituted PZT and $NiFe_2O_4$ were synthesized by conventional solid state reaction route. Detailed discussion is given in the following sections.

1.3.3 Applications of Magnetoelectric Materials

There are many ideas for device applications [36–42] based on magnetoelectric effect due to their multifunctionality. Some of the applications of magnetoelectric materials are:

- Magnetoelectric materials can be used as high sensitivity magnetic field sensors through zero field current measurements.
- For multiple state memory elements (where data is stored both in the polarization P and magnetization M) i.e. these materials may be used to store more than one bit of information in a single domain. Here, information is written magnetically, but stored in the electric polarization and leads to non–volatile memory devices. This multiple state memory elements can be read magnetically and can be erased and rewritten electrically which is faster and consumes less power as compare to magnetic rewriting.
- Transducers for magnetic field measurements.
- Electro–optic devices with switching in magnetic fields.
- Magnetically tuned capacitor where the frequency dependence of electric circuits could be tuned magnetically.

- Other applications include electrically tunable microwave devices such as filters, oscillators and phase shifters in which magnetic resonance is tuned electrically instead of magnetically.

Out of the above mentioned applications, Srinivas et al. [43] designed a low field AC Hall probe using Nickel Cobalt Ferrite–Lead Zirconate Titanate composite and AC magnetic field in the range of 1–64 Oe was detected at a fixed magnetic field of 1 kOe. Dong et al. [44] fabricated a transformer using Lead Zirconate Titanate–Terfenol D composite and predicted the possibility of an extremely high magnetoelectric voltage gain. Similarly, Tatarenko et al. [45] designed a magnetoelectric phase shifter using Yttrium Iron Garnet–Lead Zirconate Titanate composite where electric field control of the phase shift was done through magnetoelectric interactions.

1.3.4 Requirements for Materials to Exhibit ME Effect in Composites

Although piezoelectric–magnetostrictive composites (two phase systems) will give larger ME effect than that in single phase ME materials but to achieve ME effect in composites itself is a challenging task. In 1978, Boomgaard and Born outlined some requirements to obtain better ME effect in composites which are summarized here:

- Two phases should be in equilibrium and no chemical reaction should take place between the constituent phases.
- To achieve good ME coupling, magnetostriction coefficient of magnetostrictive phase and piezoelectric coefficient of piezoelectric phase should be high.
- Resistivity of the constituent phases should be high to avoid the leakage of charges developed in the piezoelectric phase and possibility to pole at higher fields (high poling strength) to get higher magnetoelectric output.
- Sintering temperature should not be too high so as to avoid diffusion between two phases (results in an increase in defect concentrations which leads to lower resistivity of composites and makes the poling more difficult).

i.e. selection of suitable combination of two phases is required to achieve better ME signal.

1.4 Review of Literature on Ferrimagnetic–Ferroelectric (ME) Materials

After 30 years of limited activity, from 2000 onwards the field of magnetoelectrics is again in limelight and extensive work has been done and reported by a number of research groups in the last decade. Number of publications per year on magnetoelectrics is also increasing drastically because this topic is attracting researchers from both groups i.e. of ferroelectricity and magnetism. Detailed survey was carried out using INSPEC data base and internet and the information collected is summarized here:

Boomgaard et al. [46] observed that the sign and the magnitude of the magnetoelectric conversion in magnetoelectric composites depend on the treatment used to achieve electrical polarization. The observed phenomena were explained by the existence of a space charge field in the ferroelectric phase, which arises due to the high temperature poling procedure used. $CuFe_{1.6}Cr_{0.4}O_4$–$BaTiO_3$ composites were prepared using conventional double sintering process and the nature of conduction was discussed in the light of polaron hopping model by Patankar et al. [47]. The maximum value of DC $(ME)_H$ was found to be 95.6 μV/(cm–Oe). Role of sintering on magnetoelectric composites of $CuFe_{1.8}Cr_{0.2}O_4$–$Ba_{0.8}Pb_{0.2}Ti_{0.8}Zr_{0.2}O_3$ has also been reported by Patankar et al. [48]. The particle size for either phase of the composite was found to increase, whereas porosity decreases with increase in sintering temperature. The variation of dielectric constant with temperature reflects diffused phase transition (DPT) type behavior. The maximum value of the magnetoelectric conversion factor equal to 182.7 μV/(cm–Oe) was obtained for 70% $Ba_{0.8}Pb_{0.2}Ti_{0.8}Zr_{0.2}O_3$–30% $CuFe_{1.8}Cr_{0.2}O_4$ composite when sintered at 1000 °C.

Kothale et al. [49] studied ME composites of $Cu_{0.6}Co_{0.4}Fe_2O_4$–$Ba_{0.8}Pb_{0.2}TiO_3$ and the maximum value of ME coefficient was observed for 15% ferrite–85% ferroelectric phase. Zhai et al. [50] studied variation of dielectric behavior of the composites (PZT:Co ferrite) with frequency in the range of 100 Hz to 1 MHz at room temperature. The ME coefficient was investigated at various bias fields and frequencies. Kulkarni et al. [51] investigated composites of $Ni_{0.8}Co_{0.1}Cu_{0.1}Fe_2O_4$–PZT and measured ME output as a function of DC magnetic field. The maximum value of ME output (625mV/cm) was observed for 25% ferrite and 75% ferroelectric phase. ME response was observed to be linear within low DC magnetic field. The maximum ME response was explained in terms of the content of ferrite, permittivity of dielectric material and the intensity of magnetic field. Tang et al. [52] showed the frequency dependence of ME effect

in $CoFe_2O_4$–$Ba_{0.55}Sr_{0.25}Ca_{0.2}Nb_2O_6$ composites. Very high values of dielectric constant were obtained at low frequencies and an interesting temperature dependence of dielectric constant was observed. The highest dE/dH value of 9.51 mV/(cm–Oe) was observed in $0.2CoFe_2O_4$–$0.8Ba_{0.55}Sr_{0.25}Ca_{0.2}Nb_2O_6$ composites under applied magnetic field of strength 1 kOe and frequency 90 kHz.

Li et al. [53] developed a two phase magnetoelectric parallel sandwich by bonding two longitudinally magnetized Terfenol–D/epoxy pseudo–1–3 magnetostrictive composite plates on two longitudinally polarized PZT/epoxy 2–2 piezoelectric composite plates combined longitudinally as a single plate and with their polarization directions arranged in reverse directions. A significantly large ME voltage sensitivity of 3.1 V/Oe was observed at the resonance frequency of 42.8 kHz under a relatively low bias field of 0.8 kOe. Further, a theory for the low–frequency Maxwell–Wagner relaxation in ME coefficients of bulk composites of nickel or cobalt ferrite and PZT was discussed by Petrov et al. [54]. ME coefficients versus frequency spectra show two types of relaxation, over 0.1–100 μHz and 1–1000 Hz. The relaxation frequencies and the magnitude of the ME coefficients are dependent on the electrical and composite parameters and volume fraction for the two phases.

The $50\%CoFe_2O_4$–$50\%BaTiO_3$ composites with four different building structures, namely: $CoFe_2O_4$–$BaTiO_3$ core–shell structure with $CoFe_2O_4$ in core, $BaTiO_3$–$CoFe_2O_4$ core–shell structure with $BaTiO_3$ in core, $CoFe_2O_4$–$BaTiO_3$ mixed structure, and $BaTiO_3$–$CoFe_2O_4$–$BaTiO_3$ layer structure were synthesized and studied by Duong et al. [55]. The core–shell structures give higher magnetoelectric (ME) coefficients compared to the other structures. Duong et al. [56] also studied the effect of preparation conditions on the microstructure of samples and the coupling between two phases (magnetostrictive and piezoelectric). In this work, the optimum conditions for preparing $CoFe_2O_4$–$BaTiO_3$ core–shell structure composites were investigated. The ME coefficients of the studied samples were found to change 20 times, from 0.18 to 3.53 and 0.1 to 2.23 mV/(cm–Oe) for longitudinal and transverse measurements, respectively which mean that the microstructure plays an important role for the magnetoelectric effect in composites. Magnetoelectric composites have been fabricated by sandwiching a lead titanate (PZT) laminate between two magnetostrictive ($Tb(Fe_{0.55}Co_{0.45})_{1.5}$) films and giant ME effect at low fields was obtained by Duc et al. [57]. ME coefficient was highly dependent on the direction

of the magnetic field with respect to the electrical polarization. On the basis of this magnetoelectric composite, a magnetic sensor operating in an AC magnetic field of 0.1 mT at a resonant frequency of 40 Hz was prepared.

Bonaedy et al. [58] systematically studied composites of $Ba_{0.6}Sr_{0.4}TiO_3$ and $La_{0.7}Ca_{0.3}MnO_3$ (where constituents $Ba_{0.6}Sr_{0.4}TiO_3$ and $La_{0.7}Ca_{0.3}MnO_3$ have nearly the same ferroelectric and ferromagnetic Curie temperatures) and observed magnetoelectric and magnetodielectric properties attributed to the extrinsic magnetoresistance origin and to the strain–induced magnetoelectric coupling at 10 K. Investigations on magnetoelectric composites ($Ni_{0.5}Zn_{0.5}Fe_2O_4$–$Ba_{0.8}Pb_{0.2}Zr_{0.8}Ti_{0.2}O_3$) by Bammannavar et al. [59] have revealed that these composites have better ME sensitivity in the low field range and useful in preparing ME devices. The AC susceptibility studies showed the existence of single domain particles of the ferrite phase together with large lattice distortion and plays significant role in piezomagnetic effect. The maximum ME voltage coefficient of 698 mV/(cm–Oe) was observed for the 30%$Ni_{0.5}Zn_{0.5}Fe_2O_4$–70%$Ba_{0.8}Pb_{0.2}Zr_{0.8}Ti_{0.2}O_3$ ME composites.

Magnetoelectric composite of $CoFe_2O_4$ and strontium doped $BaTiO_3$ were synthesized and studied by Kanamadi et al. [60]. Temperature dependent complex impedance analysis was carried out in order to separate the grain, grain boundary and electrode–electrolyte effect. Analysis of AC impedance data indicates a typical negative temperature coefficient of resistance. A maximum magnetoelectric voltage coefficient of 0.761 mV/(cm–Oe) was observed for 15%$CoFe_2O_4$–85%$Ba_{0.8}Sr_{0.2}TiO_3$ composite at room temperature. Nie et al. [61] reported effect of interface recombination on magnetoelectric coupling in $CoFe_2O_4$–$BaTiO_3$ composites. Higher value of ME coefficient was attributed to the better interface sintered by using nano–particles with the two phases and a correct poling strategy on the sample. Two–time sintering process was also performed on those ceramics and ME coefficient drop which was explained by the split of the interface during the recombination in the ceramics preparation. Park et al. [62] carefully examined the effect of an applied electric field on the extended X–ray absorption fine structure spectra of a $CoFe_2O_4$–dispersed PZT matrix composite. These studies demonstrated a tensile–compressive strain relation between the PZT matrix and the dispersed CFO phase, thereby providing an X–ray spectroscopic evidence of the interfacial strain–mediated ME coupling. Agrawal et al. [63] compared the results on three different particulate composites synthesized

using conventional sintering, microwave sintering under magnetic field and microwave sintering under electric field. The results show that magnetoelectric coefficient in the case of samples synthesized using microwave approach yields the same magnitudes as that of conventional sintering.

Gridnev et al. [64] reported magnetic and magnetoelectric properties of particulate $PbZr_{0.53}Ti_{0.47}O_3$–$Mn_{0.4}Zn_{0.6}Fe_2O_4$ composites. Measurements of magnetization–magnetic field loops, temperature and field dependence of the differential magnetic susceptibility as well as the transverse magnetoelectric voltage coefficient have shown the profound effect of the composition on studied properties. Fawzi et al. [65] showed DPT behavior in temperature dependent dielectric constant of composites of $Co_{0.8}Ni_{0.2}Fe_2O_4$ and $Pb(Mg_{1/3}Nb_{2/3})_{0.67}Ti_{0.33}O_3$. These transitions can be well described by fitting the Lorentz–type relation. CFO/PZT multiferroic composite thick films assisted by poly vinyl pyrrolidone were prepared by hybrid sol–gel processing and spin coating technique by Chen et al. [66]. The dynamic and static magnetoelectric effects were strongly dependent on the applied dc/ac magnetic field but their values were very low. The results demonstrated the prediction that ferroelectric and ferromagnetic properties can induce a strong magnetoelectric coupling only if a dense microstructure was achieved.

Kulawik et al. [67] reported the microstructure, dielectric and magnetic properties of bulk and layered $CoFe_2O_4$–$Pb(Fe_{1/2}Ta_{1/2})O_3$ composites. High and broad maxima of dielectric permittivity reaching 2000 at 1 kHz were found for bulk $CoFe_2O_4$–$Pb(Fe_{1/2}Ta_{1/2})O_3$ ceramic. Measurements of the magnetization of the investigated composites as a function of magnetic field and temperature exhibited behavior typical of hard magnetic materials. The layered composites showed lower coercivity, higher saturation magnetization and a higher magnetoelectric coefficient than the bulk ceramics. A. Gupta et al. [68] showed results of detailed structural, dielectric, magnetic and magnetoelectric studies of composites of $PbZr_{0.52}Ti_{0.48}O_3$ and $Mn_{0.3}Co_{0.6}Zn_{0.4}Fe_{1.7}O_4$. In the vicinity of the magnetic transition temperature, an anomaly in tan δ vs T plots was observed which indicates a possible magnetoelectric coupling in the samples. Magnetoelectric voltage coefficient was measured using static magnetoelectric method and highest magnetoelectric voltage coefficient of 0.312 mV/(cm–Oe) was obtained for sample 80:20 at H_{DC} = 1000 Oe.

Recently Chao et al. [69] experimentally studied the phase structure, microstructure, piezoelectric properties, dielectric characteristic and the ME effect of magnetoelectric $Pb[Zr_{0.23}Ti_{0.36}+0.02(Mg_{1/2}W_{1/2})+0.39(Ni_{1/3}Nb_{2/3})]O_3$ and $Ni_{0.8}Co_{0.1}Cu_{0.1}Fe_2O_4$ composites. The piezoelectric constant, dielectric constant, Curie temperature, remanant polarization and coercive electric field were found to decrease with increase of ferrite content. Magnetostrictive–piezoelectric composites of $CoFe_2O_4$–$BaTiO_3$ and $CoMn_{0.2}Fe_{1.8}O_4$–$BaTiO_3$ were synthesized by Hrib et al. [70] using standard solid state ceramic processing. The magnetoelectric response of the composite indicated that the substitution of iron ions for manganese ions results in decrease in the dielectric loss and improvement in the magnetoelectric signal of the composite samples. Ferrimagnetic $CoFe_2O_4$ and ferroelectric Pb $(Mg_{1/3}Nb_{2/3})_{0.35}Ti_{0.65}O_3$ composite ceramics were prepared by Pei et al. [71] and the maximum value of ME voltage coefficient (14.4 mV/cm–Oe) was observed for the composite with 50% ferrimagnetic phase and 50% ferroelectric phase. Magnetoelectric effect in a bulk composite of nickel ferrite and lead zirconate titanate has been investigated by Laletin et al. [72] by applying an AC magnetic field with no bias field. Nonlinearity of ferrite magnetostriction of the sample results in a strong distortion of the ME signals and the magnetically induced voltage can be found by integrating the ordinary ME voltage coefficient over magnetic field.

Sheikh et al. [73] systematically studied magnetoelectric composite system $CoFe_2O_4$–$Pb(Mg_{1/3}Nb_{2/3})_{0.67}Ti_{0.33}O_3$. The lattice strain was calculated using Williamson and Hall equation, which depends on the content of constituent phases in composites. Observed P–E and M–H loops indicate that the multiferroic nature of magnetoelectric ceramics is dependent on the content of individual phases. The magnetoelectric measurements are well explained with magnetostrictive behavior of the magnetic phase. Low frequency magnetoelectric (ME) coupling has been investigated in bulk and multilayers of Zn modified cobalt ferrite and lead zirconate titanate by Srinivasan et al. [74]. In bulk samples, the transverse and longitudinal couplings are weak and are of equal magnitude. A substantial strengthening of ME interactions is evident in layered structures with higher ME voltage coefficient (10–30 times) than in bulk samples.

1.5 Selection of Individual Phases

In literature, it is found that the studied systems correspond to substituted $NiFe_2O_4$, $CoFe_2O_4$, $MnFe_2O_4$, $CuFe_2O_4$, $ZnFe_2O_4$, Terfenol ferrites with substituted PZT, PMN–PT and $BaTiO_3$. Amongst the compositions (for ferromagnetic/ferrimagnetic phase) investigated so far, soft mixed ferrites have attracted a lot of interest. The most popular combinations are nickel zinc ferrites (NiZn ferrites) and manganese zinc ferrites (MnZn ferrites). These are soft magnetic materials having high electrical resistivity, low eddy current losses and high saturation magnetization [75, 76]. NiZn ferrites have higher resistivity among these two due to lower possibility of hopping conduction than in the case of MnZn ferrites which is also one of the considerations for magnetoelectric applications.

The solid solution of ferroelectric lead titanate ($PbTiO_3$) and antiferroelectric lead zirconate ($PbZrO_3$), known as PZT, with varying Zr/Ti ratio, exhibits interesting behavior [77–79] due to (i) stronger dielectric and ferroelectric properties (ii) easier to pole (iii) higher electromechanical coupling coefficients (iv) higher resistivity (v) higher Curie temperatures and (vi) lower sintering temperatures as compared to $BaTiO_3$. Depending upon the specific requirements for different applications, various PZT compositions may be chosen. Further, substitution of some suitable ions at the Pb site results in improved ferroelectric and dielectric properties. Several investigators [80–83] have studied the properties of modified PZT ceramics fabricated from high temperature solid state route. It has been found that La^{+3} and Sm^{+3} (off–valent donors) substitution in PZT (replacing Pb^{+2}) counteracts its p–type conductivity and increases the electrical resistivity. These substituents results in high dielectric constants, enhanced coupling factors, high remanant polarization and square hysteresis loops [84–86]. Thus addition of La and Sm to PZT is expected to give rise to improved magnetoelectric properties.

In addition, work done by various workers on ferrite–ferroelectric composites shows that the nickel ferrite particles are more stable in the PZT matrix as compared to $BaTiO_3$ and do not react even at high sintering temperatures [87] which is a necessary condition for obtaining higher ME output.

1.6 Objectives of Present Work

This thesis aims to synthesize and characterize modified ferrite–ferroelectric bulk composites by conventional solid state reaction method. With the above background of literature survey in this field, Zn substituted nickel ferrite is selected for ferrite phase and lead zirconate titanate (PZT) for the ferroelectric phase. It is also revealed from literature survey that addition of La and Sm in PZT ceramics improves their dielectric, ferroelectric and piezoelectric properties and hence is expected to give improved magnetoelectric coupling (higher ME output). Since solid state reaction method is the cheapest, simplest and conventional way to synthesize bulk samples, hence one of the aims of present work was to develop magnetoelectric composites with improved dielectric, ferroelectric, magnetic and magnetoelectric properties using solid state reaction method. Novel technique of sintering i.e. microwave sintering has not been explored for the synthesis of ferrite–ferroelectric composites. It provides rapid heating of material, less thermal energy losses, fine microstructure and reduced cycle time. In view of reports available on microwave sintered ceramics, some of the compositions were synthesized using microwave sintering for the present work. Structural, dielectric, ferroelectric, piezoelectric, ferromagnetic and magnetoelectric properties of these modified composites are presented here.

The main objectives are as follows:

- To prepare modified composites of Nickel Zinc Ferrite and Lead Zirconate Titanate (PZT).
- Modification was carried out by substituting La and Sm in PZT.
- Preparation and optimization of process parameters by solid state route.
- Sintering of samples by conventional and microwave techniques.
- To systematically characterize the materials for structural, electrical and magnetic properties.
- Analysis of results.

The following ceramic composition series were prepared for detailed investigations:

Series 1: Conventionally sintered $yNi_{0.8}Zn_{0.2}Fe_2O_4–(1–y)\ PbZr_{0.65}Ti_{0.35}O_3$

(y = 0, 0.05, 0.10, 0.15, 1)

Series 2: Conventionally sintered $yNi_{0.8}Zn_{0.2}Fe_2O_4–(1–y)Pb_{1–3x/2}La_xZr_{0.65}Ti_{0.35}O_3$

(x = 0.01, 0.02, 0.03 and y = 0, 0.05, 0.10, 0.15)

Series 3: Conventionally sintered $yNi_{0.8}Zn_{0.2}Fe_2O_4–(1–y)Pb_{1–3x/2}Sm_xZr_{0.65}Ti_{0.35}O_3$

(x = 0.01, 0.02, 0.03 and y = 0.05, 0.10)

Series 4: Microwave sintered $yNi_{0.8}Zn_{0.2}Fe_2O_4–(1–y)PbZr_{0.65}Ti_{0.35}O_3$

(y = 0, 0.05, 0.10, 0.15, 1)

The structural properties using XRD and SEM, the dielectric properties as a function of temperature and frequency, piezoelectric and ferroelectric properties were studied. Magnetic properties using vibrating sample magnetometer (VSM) and magnetoelectric properties using dynamic ME setup were studied.

References

1. W.G. Cady, Piezoelectricity, McGraw Hill, New York, Revised Edition by Dover Publications, New York (1964).
2. J. Valasek, Ferroelectrics, **2** (1971) 239.
3. J. Fousak, Proceedings of ISAF'9, University Park, PA (1994).
4. G. Busch, Ferroelectrics, **74** (1987) 267.
5. W. Kanzig, Ferroelectrics, **74** (1987) 285.
6. L.E. Cross and R.E. Newnham, History of Ferroelectrics, Am. Ceram. Soc., Westerville, OH (1986).
7. G. Busch, Ferroelectrics, **71** (1987) 43.
8. W.D. Kingery, Introduction to Ceramics, John Willey and Sons Inc. (1960).
9. B. Jaffe, W.R. Cook and H. Jaffe, Piezoelectric Ceramics, Academic Press, New York (1971).
10. A. Safari, R.K. Panda and V.F. Janas, Key Eng. Mater., **35** (1996) 122.
11. M.E. Lines and A.M. Glass, Principles and Applications of Ferroelectrics and Related Materials, Oxford University Press, New York (2001).
12. C.B. Sawyer and C.H. Tower, Phys. Rev., **35** (1930) 269.
13. B.T. Batthais and A.V. Hippel, Phys. Rev., **73** (1998) 1378.
14. D. Damjanovic, Rep. Prog. Phys., **61** (1998) 1267.
15. R. Ramesh, S. Aggarwal and O. Auciello, Mater. Sci. Eng. B, **32** (2001) 191.
16. P.R. Chowdhary and S.B. Deshpande, Ind. J. Pure. Appl. Phys., **17** (1979) 571.
17. C.W. Nan, M.I. Bichurin, S. Dong, D. Viehland and G. Srinivasan, J. Appl. Phys., **103** (2008) 031101.
18. A. Kumar, G.L. Sharma, R.S. Katiyar, R. Pirc, R. Blinc and J.F. Scott, J. Phys.: Condens. Matter, **21** (2009) 382204.
19. H. Schmid, Ferroelectrics, **162** (1994) 665.
20. T. Kimura, Nature, **426** (2003) 55.
21. J.F. Scott, Science, **315** (2007) 954.
22. H. Bea, M. Gajek, M. Bibes and A. Barthelemy, J. Phys.: Condens. Matter., **20** (2008) 434221.

23. P. Curie, J. Phys., **3** (1894) 393.
24. W.C. Rontgen, Ann. Phys. Chem., **35** (1888) 264.
25. H. Schmid, Ferroelectrics, **162** (1994) 317.
26. N. Hill, J. Phys. Chem. B, **104** (2000) 6694.
27. A.M.J.G. Run, D.R. Terrell and J.H. Scholling, J. Mater. Sci., **9** (1974) 1710.
28. J.V. Boomgaard and R.A.J. Born, J. Mater. Sci., **13** (1978) 1538.
29. G. Harshe, J.P. Dougherty and R.E. Newnham, Int. J. Appl. Electromag. Mater., **4** (1993) 161.
30. S.X. Dong, J.F. Li and D. Viehland, J. Appl. Phys., **95** (2004) 2625.
31. F. Cebollada, J.M. Gonzalez, J.D. Frutos and A.M. Gonzalez, Bol. Soc. Esp. Ceram. Vidrio, **44** (2005) 169.
32. R.C. Kambale, P.A. Shaikh, C.H. Bhosale, K.Y. Rajpure and Y.D. Kolekar, J. Alloys Compds., **489** (2010) 310.
33. J.K. Lee, C.H. Kim, H.S. Suh and K.S. Hong, Appl. Phys. Lett., **80** (2002) 3593.
34. W. Erenstein, N.D. Mathur and J.F. Scott, Nature, **442** (2006) 759.
35. S. Priya and D.J. Inman, Energy Harvesting Technologies, LLC (2009).
36. K. Uchino, Ferroelectric Devices, New York, Marcel Dekker Inc. (2000).
37. J.F. Scott, Nat. Mater., **6** (2007) 256.
38. M. Gajek, M. Bibes, S. Fusil, K. Bouzehouane, J. Fontcuberta, A. Barthelemy and A. Fert, Nat. Mater., **6** (2007) 296.
39. M. Vopsaroiu, J. Blackburn, A. Muniz–Piniella and M.G. Cain, J. Appl. Phys., **103** (2008) 07F506.
40. S.V. Suryanarayana, Bull. Mater. Sci., **17** (1994) 1259.
41. S. Dong, J.F. Li and D. Viehland, Appl. Phys. Lett., **85** (2004) 2307.
42. N. Ortega, P. Bhattacharya, R.S. Katiyar, P. Dutta, A. Manivannan, M.S. Seehra, I. Takeuchi and S.B. Majumder, J. Appl. Phys., **100** (2006) 126105.
43. A. Srinivas, Ph.D. Thesis, Osmania University, Hyderabad (2000).
44. S. Dong, J.F. Li, D. Viehland, J. Cheng and L.E. Cross, Appl. Phys. Lett., **85** (2004) 3534.
45. A.S. Tatarenko, G. Srinivasan and M.I. Bichurin, Appl. Phys. Lett., **88** (2006) 183507.
46. J.V. Boomgaard and A.M.J.G. van Run, Solid State Commun., **19** (1976) 405.

47. K.K. Patankar, S.A. Patil, K.V. Sivakumar, R.P. Mahajan, Y.D. Kolekar and M.B. Kothale, Mater. Chem. Phys., **65** (2000) 97.
48. K.K. Patankar, R.P. Nipankar, V.L. Mathe, R.P. Mahajan and S.A. Patil, Ceram. Int., **27** (2001) 853.
49. M.B. Kothale, K.K. Patankar, V.L. Mathe and B.K. Chougule, Mater. Chem. Phys., 77 (2002) 691.
50. J.Y. Zhai, N. Cai, L. Liu, Y.H. Lin and C.W. Nan, Mater. Sci. Eng. B, **99** (2003) 329.
51. S.R. Kulkarni, C.M. Kanamadi and B.K. Chougule, Mater. Res. Bull., **40** (2005) 2064.
52. Y.H. Tang, X.M. Chen, Y.J. Li and X.H. Zheng, Mater. Sci. Eng. B, **116** (2005) 150.
53. T. Li, S.W. Or, H. Lai and W. Chan, J. Magn. Magn. Mater., **304** (2006) e442.
54. V.M. Petrov, M.I. Bichurin, G. Srinivasan, J. Zhai and D. Viehland, Solid State Commun., **142** (2007) 515.
55. G.V. Duong, R. Groessinger and R.S. Turtelli, J. Magn. Magn. Mater., **310** (2007) e361.
56. G.V. Duong and R. Groessingera, J. Magn. Magn. Mater., **316** (2007) e624.
57. N.H. Duc and D.T.H. Giang, J. Alloys Compd., **449** (2008) 214.
58. T. Bonaedy, K.M. Song, K.D. Sung, N. Hur and J.H. Jung, Solid State Commun., **148** (2008) 424.
59. B.K. Bammannavar and L.R. Naik, J. Magn. Magn. Mater., **321** (2009) 382.
60. C.M. Kanamadi, J.S. Kim, H.K. Yang, B.K. Moon, B.C. Choi and J.H. Jeong, J. Alloys Compd., **481** (2009) 781.
61. J.W. Nie, G.Y. Xu and X.J. Qi, Trans. Nonferr. Metal. Soc., **19** (2009) 1593.
62. J.H. Park, M.G. Kim, S.J. Ahn, S. Ryu and H.M. Jang, J. Magn. Magn. Mater., **321** (2009) 1971.
63. S. Agrawal, J. Cheng, R. Guo, A.S. Bhalla, R.A. Islam and S. Priya, Mater. Lett., **63** (2009) 2198.
64. S.A. Gridnev, A.V. Kalgin, A.A. Amirov and I.K. Kamilov, Ferroelectrics, **397** (2010) 142.
65. A.S. Fawzi, A.D. Sheikh and V.L. Mathe, Mater. Chem. Phys., **119** (2010) 385.
66. W. Chen, S. Shannigrahi, X.F. Chen, Z.H. Wang, W. Zhu and O.K. Tan, Solid State Commun., **150** (2010) 271.
67. J. Kulawik, P. Guzdek, D. Szwagierczak and A. Stoch, Compos. Struct., **92** (2010) 2153.
68. A. Gupta and R. Chatterjee, J. Magn. Magn. Mater., **322** (2010) 1020.

69. X. Chao, Z. Yang, M. Dong and Y. Zhang, J. Magn. Magn. Mater., **323** (2011) 2012.
70. L.M. Hrib and O.F. Caltun, J. Alloys Compd., **509** (2011) 6644.
71. Y. Pei, Q. Li, W. Shi, B. Zhang, Q. Chen, X. Yue, D. Xiao and J. Zhu, Ferroelectrics, **410** (2011) 82.
72. V.M. Laletin and V.M. Petrov, Solid State Commun., **151** (2011) 1806.
73. A.D. Sheikh and V.L. Mathe, J. Phys. Chem. Solids, **72** (2011) 1423.
74. G. Srinivasan, R. Hayes and C.P. DeVreugd, to be published in Appl. Phys. A.
75. A.G. Nutan, C.V. Subhash and D.C. Kashyap, Solid State Commun., **134** (2005) 689.
76. M.A. Ruiting, Y. Wang, T. Yanwen, Z. Chunli and L. Xikun, J. Mater. Sci. Technol., **24** (2008) 419.
77. O.P. Thakur and C. Prakash, Integr. Ferroelectr., **122** (2010) 100.
78. J.K. Juneja, C. Prakash, O.P. Thakur and T.P. Sharma, Ferroelectr. Lett., **29** (2002) 11.
79. G. H. Haertling, J. Am. Ceram. Soc., **82** (1999) 797.
80. G.H. Haretling and C.E. Land, J. Am. Ceram. Soc., **54** (1971) 1.
81. C. Prakash, O.P. Thakur and P. Kishan, Ferroelectrics, **263** (2001) 61.
82. S.K. Pandey, O.P. Thakur, A. Goyal, D.S. Rawal, C. Prakash. R. Chatterjee and T.C. Goyal, Mod. Phys. Lett. B, **20** (2006) 1883.
83. K. Kakegawa, K. Arai, Y. Sasaki and Y. Tomizawa, J. Am. Ceram. Soc., **71** (1988) 49.
84. Y. Tomita, K. Lijima, R. Takayama and I. Ueda, J. Appl. Phys., **60** (1986) 361.
85. M. Okyama and Y. Hamakawa, Ferroelectrics, **63** (1985) 243.
86. M. Einat, D. Shur, E. Jerby and G. Roseman, J. Appl. Phys., **89** (2001) 548.
87. R.A. Islam and S. Priya, Integr. Ferroelectr., **82** (2006) 1.

Chapter-II

Synthesis and Characterization Techniques

Chapter–II

Synthesis and Characterization Techniques

In this chapter, the detailed experimental procedure for synthesis of the samples is discussed. Synthesized samples were studied for their structural, microstructural, dielectric, ferroelectric, magnetic and magnetoelectric properties. The description of various characterization techniques used to study these properties is also discussed in this chapter.

2.1 Material Synthesis: Conventional Solid State Route

Though the material properties are basically controlled by the composition, synthesis methodology and their processing parameters play an important role in deciding end product performance. Our main objective for synthesizing ferrite–ferroelectric composites is to prepare materials with good properties. Several processing techniques have been developed such as conventional solid state route, coprecipitation, sol–gel processing, hydrothermal synthesis, spray and freeze drying etc. For the present study, we have selected the solid state route as it is the cheapest, simplest and conventional way to synthesize bulk samples. Various steps used in the processing of modified composites via solid state route are described in the figure 2.1. The method was used to synthesize both (ferrite and ferroelectric) components separately (figure 2.1(a)). Fully reacted powder of two compositions was mixed in desired ratio and processed as shown in figure 2.1(b). Description of various steps used in the synthesis of modified ME composites is given in the schematic ahead.

2.1.1 Raw Materials and Ball Milling

The first step of material synthesis is to weigh the raw materials in stoichiometric proportion followed by mixing of raw materials to eliminate aggregate and to reduce particle size. The particle size reduction is necessary before firing because the time taken for compound formation during heating is proportional to the square of the particle size. The most commonly used method for grinding (or mixing) is wet ball milling. This method can

eliminate aggregates and can reduce the particle size (10–1 μm) and results in homogeneous mixture.

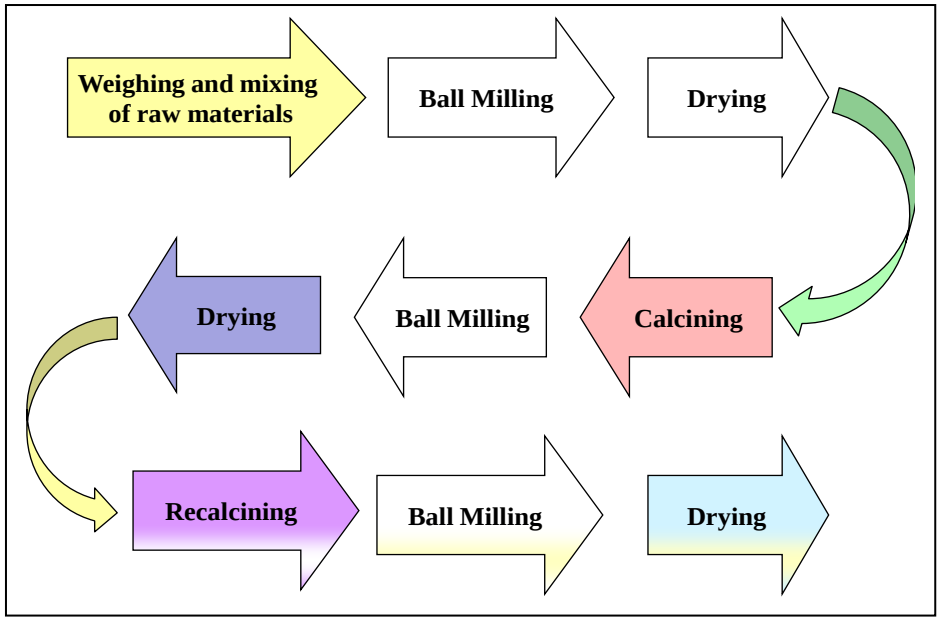

(a)

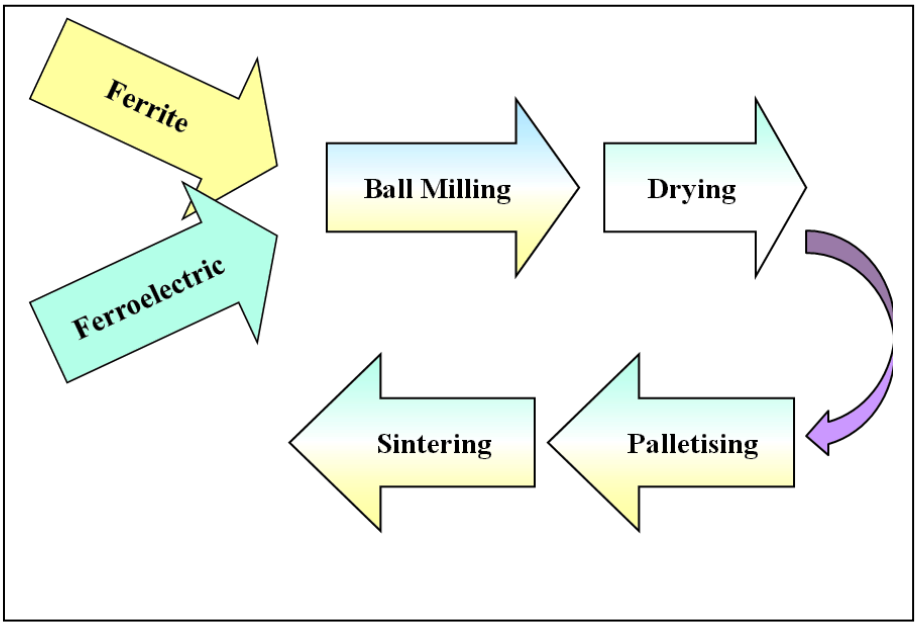

(b)

Figure 2.1 Solid state route for synthesis of (a) individual phases and (b) composites

The ball milling technique chosen for mixing and grinding was planetary ball milling. The schematic of the planetary ball milling is shown in figure 2.2. It consists of grinding bowls which are arranged eccentrically on a rotating plate. The direction of movement of the plate is opposite to that of the bowls. The difference in the speeds of the grinding balls and bowl releases high dynamic energies resulting in better homogeneity and finer particle size of the powder.

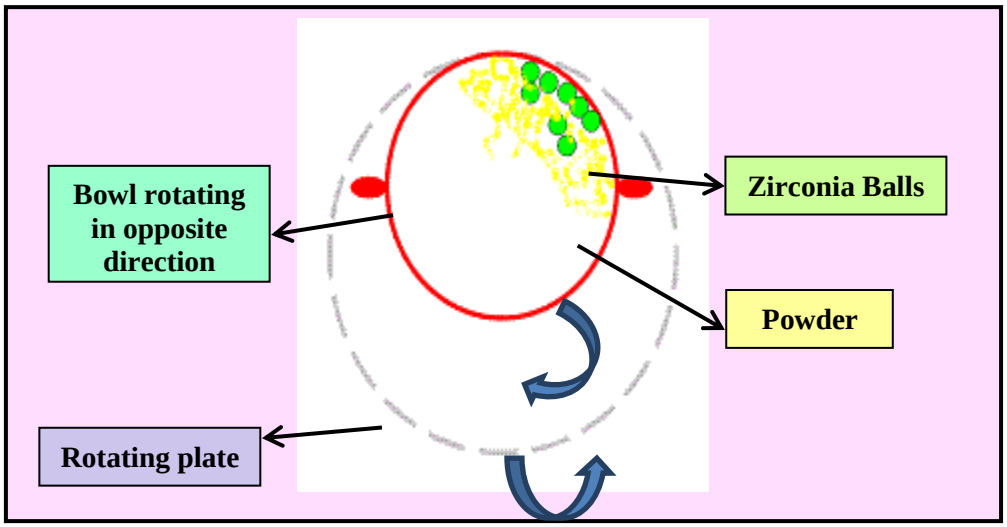

Figure 2.2 The schematic of planetary ball milling

Specifications

- Type: Mini Ball Mill (Two Bowls)
- Purpose: For grinding raw materials for synthesis of ceramics
- Plate speed: 40 to 500 r.p.m.
- Bowl speed: Maximum 1000 r.p.m.
- Motor: AC motor with variable speed
- Fully programmable speed, rotation direction and run time.

Figure 2.3 Planetary ball mill

In the present work, AR grade PbO, ZrO_2, TiO_2, La_2O_3 and Sm_2O_3 for modified lead zirconate titanate and NiO, ZnO, MnO_2 and Fe_2O_3 for modified nickel zinc ferrite were used as raw materials and weighed in the required molar proportions. Ball milling was done using water as milling media and zirconia balls as grinding media in planetary ball mill (figure 2.3) for 3 hrs. The wet slurry was then subjected to drying in oven at 140 ^oC.

2.1.2 Calcination

Calcination is a pre–firing process in which the constituents react by inter–diffusion of their ions. It reduces the extent of diffusion that must occur during sintering and results in homogeneous products. During calcination, the carbonates decompose into oxides and the solid state reaction just starts. The calcination temperature must be high enough to cause reaction, but low enough to avoid grinding problems due to hardening of powder. The containers must be closed and calcination temperature must be comparatively low if any of the constituents are volatile e.g. PbO. After calcination, the powder must be ball milled as calcined powder is coarser and more abrasive than the raw materials.

Specifications

- Heating elements: Silicon carbide
- Working area (inside heating zone): 12" Depth x 6" Height x 6" Width
- Maximum operating temperature:1450 ^oC
- Thermocouple used: R–type
- Accuracy: ±1 ^oC
- Heating rate and soaking period are programmable using a PID controller.

Figure 2.4 Programmable furnace for calcination and sintering

The dried powder mixture for ferroelectric phase was calcined at 800 ^{o}C for 4 hrs. The reacted powder mixture was ball milled and then re–calcined at 1000 ^{o}C for 4 hrs after drying. The dried powder mixture for ferrite phase was calcined at 1000 ^{o}C for 4 hrs. A small amount of MnO_2 (0.5% by weight) was added as sintering aid and to improve resistivity. After ball milling and drying, powder mixture was re–calcined at 1100 ^{o}C for 4 hrs. A programmable furnace with silicon carbide heating elements (figure 2.4) was used for calcination and sintering of samples. The calcined powders were ground in an agate pestle mortar, ball milled again and dried.

2.1.3 Compaction of Powder (Shaping)

The dried powder is then compacted to the desired shape. Before compaction, it is necessary to add an organic binder into the powder for giving sufficient strength to the green samples. It should be possible to remove the binder from the compacted shapes without any disruptive effect. There are a number of compaction techniques which include uniaxial pressing, isostatic pressing, calendaring, extrusion, jiggering, injection moulding, slip casting, band casting etc.

Figure 2.5 Hydraulic press

For the present work, uniaxial pressing technique was employed. The dried powder mixtures were mixed with few drops of diluted (3% by wt.) polyvinyl alcohol (PVA) binder and dried. Hydraulic press (figure 2.5) was used for pressing circular discs (~ 15 mm diameter and 1–2 mm thickness) by applying a pressure of 200 kg/cm^2 for 2 min.

2.1.4 Sintering

The sintering is basically a heat treatment that converts the green disc into a denser polycrystalline structure. In this structure, crystallites (grains) are joined to one another by grain boundaries of varying thickness (100 pm to 1 μm range) [1]. At an appreciable temperature, the area between the grains in contact increases due to the thermal expansion of the grains and finally only one interface between two grains remain which results in densified ceramics [2]. Grain growth and densification take place simultaneously and this process is energetically favoured by the reduction in the area of grain boundaries.

2.1.4.1 Conventional Sintering (CS)

In conventional sintering, energy is transferred to the inside of the material through convection, conduction and radiation of heat from the surfaces of the material. It is a slow heating process and takes considerable time to achieve thermal equilibrium. For the present work, the green bodies were sintered at optimized temperature of 1200 ^{o}C in a programmable silicon carbide heating elements based high temperature furnace (figure 2.4). The heating rate was kept at 5 ^{o}C/min and soaking period of 4 hrs. The pellets were sintered in closed alumina crucibles and a lead rich atmosphere was maintained to minimize lead loss during sintering. $PbZrO_3$ powder was kept along with the material to be sintered for maintaining lead rich atmosphere along with an excess amount of lead during weighing of raw materials.

2.1.4.2 Microwave Sintering (MS)

Microwave processing of ceramic materials has recently become an attractive area for research [3–7]. The growing interest in use of microwave energy for materials processing over conventional processing methods is essentially due to absorption of microwave energy

followed by generation of heat within the sample volume itself by the conversion of electromagnetic energy into thermal energy [8]. This results in many advantages such as volumetric and rapid heating of material, less thermal energy losses and lower reaction temperatures. This unique heating method also results in fine microstructure [9, 10]. Especially for the lead based ceramics, there is problem of lead loss and serious environmental issues due to lengthy sintering soaking time during conventional sintering which can be reduced by using microwave technique. It has already been reported by a number of researchers [11–16] that microwave sintering of materials is superior to conventional sintering. For present work, green bodies were sintered at 1150 ^{o}C for 10 min in a programmable microwave furnace (figure 2.6) at a heating rate of 50 ^{o}C/min. The temperature–time graph for conventional sintering and microwave sintering is compared in figure 2.7.

Specifications

- Insulation: High alumina bricks & back up by zirconia blend ceramic fiber
- Size of sample: Maximum 35 mm
- Heating system: Microwaves (2.45 GHz) by magnetron
- Power output: 1.5 kW
- Maximum Temperature: 1650 ^{o}C
- Temperature sensor: IR sensor
- Fully programmable

Figure 2.6 Microwave furnace

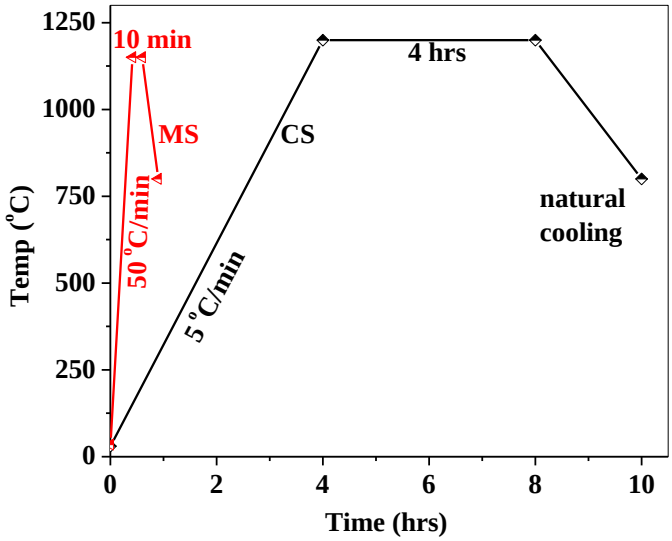

Figure 2.7 Temperature–time graph for conventional and microwave sintering

2.2 Characterization Techniques

The samples prepared by solid state method were characterized for their structural, dielectric, ferroelectric, piezoelectric, ferromagnetic and magnetoelectric properties. Detailed description of various characterization techniques is given in this section.

2.2.1 X–Ray Diffraction (XRD)

XRD is the basic characterization technique for structural analysis in material science. It provides a convenient and practical means for the qualitative identification of crystalline compounds because it gives unique pattern for each crystalline substance. XRD data can be used to determine lattice parameters and crystal structure. The systematic scattering properties of X–rays make them ideally suitable for probing the structural arrangement of atoms and molecules in a wide range of materials (figure 2.8) because the wavelength of X–rays is comparable to the interplanar spacing. The energetic X–rays can penetrate deep into the material and provide information about the bulk structure of the material [17, 18]. The basic principle involved is that the constructive interference occurs for a fixed set of interplanar spacing (d) and angle of incidence (θ) for a particular wavelength (λ).

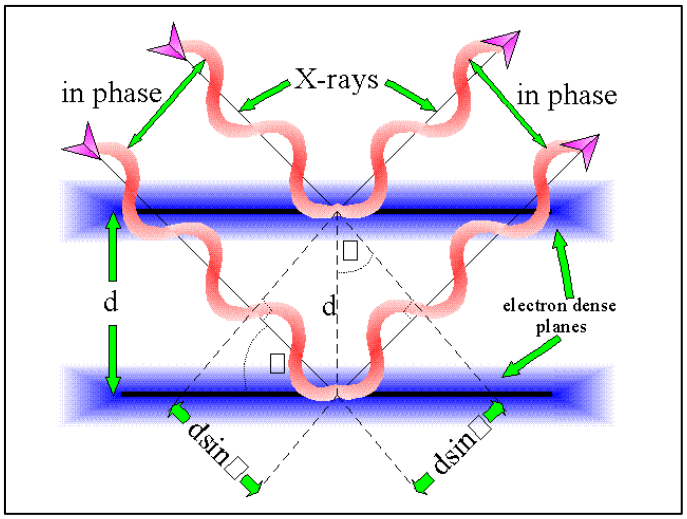

Figure 2.8 Bragg's law for reflection

An XRD instrument measures intensity of diffracted radiations as a function of θ. These θ values can be used to determine interplanar spacing (d) using Bragg's equation:

$$2d\sin\theta = n\lambda \qquad \ldots. (2.1)$$

Where n is the order of the diffraction (normally only first order is observed in XRD).

For a cubic system, the interplanar spacing (d) is given by:

$$\frac{1}{d^2} = \frac{h^2 + k^2 + l^2}{a^2} \qquad \ldots. (2.2)$$

Where h, k and l are Miller indices and a is lattice constant.

Combining equations 2.1 and 2.2, we get:

$$\sin^2\theta = \frac{\lambda^2}{4a^2}\left(h^2 + k^2 + l^2\right) \qquad \ldots. (2.3)$$

Similarly, relations for a tetragonal, orthorhombic and rhombohedral system are:

$$\sin^2\theta = \frac{\lambda^2}{4}\left(\frac{h^2 + k^2}{a^2} + \frac{l^2}{c^2}\right) \qquad \ldots. (2.4)$$

$$\sin^2\theta = \frac{\lambda^2}{4}\left(\frac{h^2}{a^2}+\frac{k^2}{b^2}+\frac{l^2}{c^2}\right) \quad \ldots. (2.5)$$

$$\sin^2\theta = \lambda^2\left[\frac{(h^2+k^2+l^2)\sin^2\alpha + 2(hk+kl+lh)(\cos^2\alpha-\cos\alpha)}{4a^2(1+2\cos^3\alpha-3\cos^2\alpha)}\right] \quad \ldots. (2.6)$$

Using these equations, we can determine the lattice parameters of the unit cell. Further intensities of diffracted beams give information about the atomic positions within the unit cell.

For the present study, the XRD data was recorded using a Philips XPERT–PRO Diffractogram. Cu–K_α radiation was used to obtain the diffraction pattern. The X–ray tube was operated at 45 kV and 40 mA current. X–ray data was taken for the calcined powders and sintered pellets in the range of $2\theta = 20^o$–70^o with step size of 0.01^o. Lattice parameters were calculated by indexing the peaks of the XRD patterns using the standard reference data of the materials.

2.2.2 Density Measurements

Measurement of density of ceramic samples gives the information regarding the presence of crystal defect such as vacancies, porosity etc. In most of the electrical applications, samples are required to have good densification. However, there are cases where porosity is quite desirable e.g. in humidity and gas sensors. For the present work, the experimental density (d_{exp}) of the samples was determined by using Archimedes' principle and is given as:

$$d_{exp} = \frac{W_a}{W_a - W_w} \times d_w \quad \ldots. (2.7)$$

Where, W_a is the weight of the sample in the air, W_w is the weight of the sample in the water and d_w is the density of the water.

Theoretical density of the composites was computed using the following formula:

$$d_{th} = y\left(\frac{nM}{Na^3}\right)_{ferritephase} + (1-y)\left(\frac{nM}{Na^3}\right)_{ferroelectic\ phase} \quad \ldots. (2.8)$$

Where, y is the fraction of ferrite phase present in the composite samples, n is the number of molecules per unit cell (n = 8 for ferrite phase and 1 for ferroelectric phase), M is the molecular weight, N is Avogadro's number and a is the lattice constant.

Experimental bulk density of any sample, determined using Archimedes' principle is always less than that of theoretical (X–ray) density because the sample usually contains some defects like cracks, vacancies, pores etc.

Relative density (%) was calculated using the formula:

$$d_{rel}(\%) = \frac{d_{exp}}{d_{th}} \times 100 \quad \text{.... (2.9)}$$

and porosity P(%) was calculated using the formula:

$$P(\%) = 100 - d_{rel}(\%) \quad \text{.... (2.10)}$$

2.2.3 Scanning Electron Microscope (SEM)

The scanning electron microscope (SEM) has unique capabilities for analyzing surfaces. The SEM uses electrons for image formation, which have much shorter wavelength than light photons and are capable of generating high resolution information. It has a large depth of field (ability to maintain focus across a field of view regardless of surface roughness). It results in micrographs with the three dimensional appearance of textured surfaces. The combination of high resolution, an extensive magnification range and high depth of field makes the SEM highly suited for the study of surfaces. It also helps in investigating the effect of substituents on microstructure.

For the present work, SEM micrographs of the freshly broken pieces of sintered samples were obtained using JEOL JSM 6510LV, Japan. The broken pieces were placed on the brass stub and a thin layer of gold was deposited using sputtering technique. Micrographs taken were used to observe the grains and helped in studying and identifying the porosity and uniformity of the samples.

2.2.4 Electroding

The sintered samples were lapped and polished using abrasive powders of different grades. These polished samples were ultrasonically cleaned to remove any kind of impurities left on the surface. Care was taken to ensure that the opposite faces of the samples were parallel and flat. To study electrical properties of the samples, the electrical contacts were made by depositing silver epoxy on both flat surfaces of the sample. Then samples were heated at 400 ^{o}C for 30 min to ensure curing and good ohmic contacts.

2.2.5 Dielectric Measurements

Study of the dielectric properties provides a great deal of information about the suitability of the material for various applications e.g. as capacitive elements in electronic applications. Dielectric constant (ε') and dielectric loss (tanδ) are the important practical parameters for most applications. Dielectric properties of materials depend on temperature, frequency of applied field, humidity, crystal structure and other external factors [19].

Dielectric properties (dielectric constant and dielectric loss) can be measured by comparing the capacitance of a parallel plate capacitor in vacuum with one in the presence of the material for which the dielectric properties are to be measured. The capacitance (C) for a parallel plate capacitor separated by vacuum is given by:

$$C = \frac{\varepsilon_o A}{t} \qquad \ldots. (2.11)$$

Where ε_o is the permittivity of free space and is equal to 8.85 x 10^{-12} F/m, A is the area of the plate and t is the separation between two parallel plates. If a dielectric material is introduced between the plates of the capacitor, the new value of capacitance is given as:

$$C = \frac{\varepsilon A}{t} \qquad \ldots. (2.12)$$

Where ε is the dielectric constant of the material placed between the plates.

The relative permittivity i.e. dielectric constant of the material is:

$$\varepsilon_r = \frac{\varepsilon}{\varepsilon_o} \qquad \ldots. (2.13)$$

For an alternating electric field, the dielectric constant can be expressed in terms of real and imaginary quantities as:

$$\varepsilon_r = \varepsilon' - i\varepsilon'' \quad \text{.... (2.14)}$$

When the dielectric material between the plates of capacitor is ideal (loss free), the current leads the voltage by 90^o. However, in practical dielectric materials (non–ideal), there exists a loss current in addition to the charging current associated with the storage of electric charge by the dipoles which arises due to DC ohmic conduction and the dissipation of energy associated with the rotation or oscillation of dipoles [20]. Thus, the total current in the practical dielectrics is a complex quantity and leads the voltage by 90–δ, where δ is called loss angle. Dielectric loss, also known as dissipation factor, is given as:

$$\tan\delta = \frac{\varepsilon''}{\varepsilon'} \quad \text{.... (2.15)}$$

The dielectric properties of the modified ferrite–ferroelectric composites were measured as a function of temperature (30 – 500 ^oC) at discrete frequencies of 1 kHz, 10 kHz and 100 kHz and as a function of frequency (100 Hz – 1 MHz) at room temperature using Agilent 4284A LCR meter (figure 2.9). The LCR meter is connected with a programmable temperature controller and interfaced with a PC.

Figure 2.9 Agilent 4284A LCR meter

2.2.6 AC Conductivity

The AC conductivity measurement is a powerful tool to understand the performance of the dielectric material. It provides information of the defects and loss mechanisms in the dielectric materials. Most of the earlier investigations on ceramic materials describe the electrical conductivity in terms of electrons (holes), polarons, oxygen vacancies and impurities [21].

For the present work, the AC conductivity of the samples was calculated from the dielectric parameters using the standard relation:

$$\sigma_{ac} = \omega\varepsilon' \varepsilon_o \tan\delta \qquad \ldots. (2.16)$$

Where ω is the angular frequency, ε_o is the permittivity of the free space, ε' is the dielectric constant and $\tan\delta$ is the loss tangent.

2.2.7 P–E Hysteresis Loop Set–up

Polarization switching is a common criterion of ferroelectricity which can be observed by measuring the polarization versus electric field (P–E) relationship below T_c[2]. This is usually done using Sawyer–Tower circuit [22] shown in figure 2.10. The method consists of applying an alternating voltage and studying the relationship between the stored charge and instantaneous voltage for test sample. A capacitor C_1 of high value is connected in series with the test sample (C_x). The voltage across this capacitor measures the charge stored on the test sample.

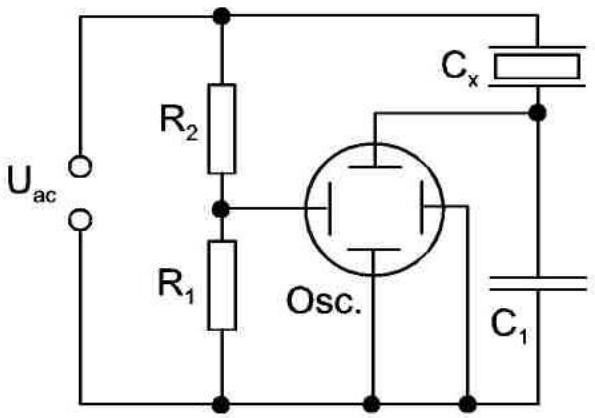

Figure 2.10 Sawyer–Tower circuit

Figure 2.11 represents the P–E loop tracer used for the present study. It is based on Sawyer–Tower circuit and is operated at discrete frequencies ranging 20–1000 Hz. The system consists of a PC, software, programmable voltage source (up to 3 kV) and sample holder. The sample was kept in silicon oil bath to avoid any sparking or breakdown at high voltage.

Figure 2.11 P–E hysteresis loop tracer

2.2.8 Poling

The domains are randomly oriented in the polycrystalline ferroelectric ceramics and hence these ceramics show piezoelectric effect only after domain reorientation. Proper electric field must be applied on the sample for certain time for domain reorientation. It results in reorientation of domains in the direction of the applied electric field and the sample starts exhibiting piezoelectric effect. The properties of ferroelectric ceramics can be controlled by changing magnitude of applied field and temperature at which poling is done [23]. For obtaining better properties, a field higher than coercive field (E_c) must be applied at higher temperature during poling.

For present work, the sample was electroded, mounted in sample holder and then kept in silicon oil bath. The sample was heated to 150 ^{o}C and a DC electric field (~15 kV/cm) was

applied for 1 hr. Then the sample was cooled to room temperature in the presence of field. Care was taken so that the applied field does not cause dielectric breakdown. The set–up for electrical poling is shown in figure 2.12.

Figure 2.12 Set–up for electric poling

2.2.9 Piezoelectric Charge Coefficient

The piezoelectric charge coefficient (d_{33}) of electrically poled sample was measured using d_{33} meter (Model–2, Concord Electroceramic Industries, India) shown in figure 2.13. This is based on Berlincourt principle. It consists of force head, electronic driver and d_{33} read out unit. The force head has an electromagnetic driver which vibrates the internal calibration piezo element as well as the piezo test specimen which are mechanically in series. It is so designed that it facilitates measurement of d_{33} coefficient for a variety of piezoelectric materials of varying sizes and shapes. The piezoelectric sample under test is clamped within the jaws of the force head unit for testing. The oscillator and electromagnetic driver provide AC voltage to the electromagnetic driver in the force head and the charge developed across the sample is measured and displayed digitally in d_{33} read out. The measurable d_{33} range by this meter is 50–1000 pC/N with accuracy up to ±5.0%.

Figure 2.13 Piezo d_{33} meter

2.2.10 Vibrating Sample Magnetometer (M–H Hysteresis Loop Set–up)

Magnetic hysteresis loop is the most significant characteristic of magnetic materials. It provides essential information about the magnetic properties of the materials. There are many techniques to obtain magnetic hysteresis loops like vibrating sample magnetometer (VSM), superconducting quantum interference device (SQUID), hysteresisgraph etc. For the present work, VSM technique was employed for obtaining M–H hysteresis loops as it is very sensitive and suitable for weak magnetic samples. This technique was developed by Simon Foner [24]. It is based on the change in flux in a coil when a sample is made to vibrate (figure 2.14). The vibrating sample is placed in an adjustable uniform magnetic field. The magnetic moment of the sample is detected by pickup coils (induced voltage in pickup coils is directly proportional to the magnetic moment). Hysteresis curve of the material is obtained by measuring the induced voltage in pickup coils using lock–in amplifier and measuring the intensity of field produced by electromagnet. Lake Shore 735 VSM Controller, Model 662 was used for recording M–H hysteresis loops and from these loops, related parameters i.e. saturation magnetization (M_s), coercive field (H_c) and remanant magnetization (M_r) were determined.

2.2.11 Magnetoelectric (ME) Coupling

As discussed in chapter–I, the coexistence of magnetism & ferroelectricity and particularly existence of magnetoelectric (ME) coupling between the constituent phases (magnetic and ferroelectric) offers new ideas for multifunctional device applications. Various direct or indirect methods have been reported in literature to measure ME coupling. The methods that we have used for studying ME coupling are:

1. Using VSM and 2. ME Set–up

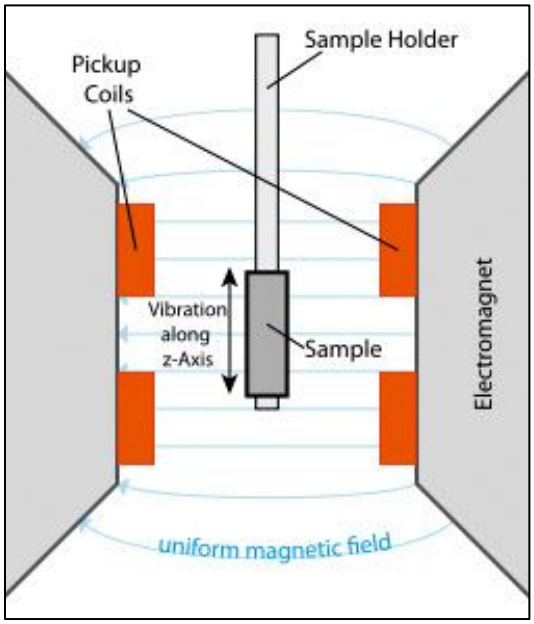

Figure 2.14 Schematic for vibrating sample magnetometer

2.2.11.1 Using VSM

In this method, two pieces from a single pellet were taken to study magnetoelectric coupling. One piece was electrically poled at 15 kV/cm before doing M–H measurements and M–H hysteresis curves were measured for both electrically poled and unpoled samples and compared. An enhancement in magnetization was observed for electrically poled sample, which confirms the presence of magnetoelectric coupling between the constituent phases.

2.2.11.2 ME Set–up

In this method, the magnetoelectric signal (voltage) for composite samples was determined as a function of increasing DC magnetic field (0–2000 Oe) using 7265 DSP lock–in amplifier in the presence of small AC magnetic field (H_{AC} = 10 Oe at 1 kHz). The superimposed AC magnetic field does not allow the charges to move towards the electrodes and true value of ME signal can be obtained. Prior to the magnetoelectric measurements, the sample was electrically poled at 15 kV/cm. Electrically poled sample was mounted in sample holder and placed in between the pole pieces of an electromagnet. Proper shielding arrangements were made to avoid stray signals. ME coupling coefficient, α (mV/cm–Oe) was determined from the magnetoelectric signal (δV) using the formula [25]:

$$\alpha = \frac{\delta V}{t \cdot H_{AC}} \quad \text{…. (2.17)}$$

Where δV is the magnetoelectric signal (voltage generated due to magnetoelectric effect), t is the thickness of the sample and H_{AC} is the AC magnetic field.

References

1. A.J. Moulson and J.M. Herbert, Electroceramics: Materials, Properties, Applications, Chapman and Hall, London (1990).
2. Y. Xu, Ferroelectric Materials and their Applications, Elsevier Science Pub. Co., New York (1991).
3. W.H. Sutton, Am. Ceram. Soc. Bull., **68** (1989) 376.
4. A.C. Metaxas and J.G.P. Binner, Advanced Ceramic Processing Technology, Noyes Publications, NJ, USA (1990).
5. R. Roy, D. Agrawal, J. Cheng and S. Gedevanishvili, Nature, **399** (1999) 668.
6. Z. Cao, Z. Wang, N. Yoshikawa and S. Taniguchi, J. Phys. D: Appl. Phys., **41** (2008) 092003.
7. M.W. Porada, Mater. Res. Bull., **18** (1993) 51.
8. D. Agrawal, Trans. Ind. Ceram. Soc., **65** (2006) 129.
9. L.M. Sheppard, Am. Ceram. Soc. Bull., **67** (1988) 1656.
10. J.D. Katz and R.D. Blake, Am. Ceram. Soc. Bull., **70** (1991) 1304.
11. B. Vaidhyanathan, A.P. Singh, D.K. Agrawal, T.R. Shrout and R. Roy, J. Am. Ceram. Soc., **10** (2001) 1197.
12. O.P. Thakur, C. Prakash and D.K. Agrawal, Mater. Lett., **56** (2002) 970.
13. C.C. Chou, H.Y. Chang, I.N. Lin, B.J. Shaw and J.T. Tan, Jpn. J. Appl. Phys., **37** (1998) 5269.
14. Z. Xie, Z. Gui, L. Li, T. Su and Y. Huang, Mater. Lett., **36** (1998) 191.
15. Z. Xie, J. Yang and Y. Huang, J. Eur. Ceram. Soc., **19** (1999) 381.
16. S. Singh, O.P. Thakur and C. Prakash, J. Phys. D: Appl. Phys., **38** (2005) 1621.
17. S.K. Chatterjee, X–ray Diffraction: its Theory and Applications, Prentice Hall of India Private Limited, New Delhi (1999).
18. B.D. Cullity, Elements of X–ray Diffraction, Addison–Wesley Publication Company Inc., Massachusetts, Menlo Park, California (1978).
19. M.W. Barsoum, Fundamentals of Ceramics, The McGraw–Hill Companies Inc., New York (1997).
20. B. Jaffe, W. Cook and H. Jaffe, Piezoelectric Ceramics, Academic Press, London (1971).
21. R.C. Buchanan, Ceramic Materials for Electronics, Marcel Dekker Inc., New York (1998).
22. C.B. Sawyer and C.H. Tower, Phys. Rev., **35** (1930) 269.

23. I.S. Zheludev, Physics of Crystalline Materials, Plenum Press, New York (1971).
24. S. Foner, Rev. Sci. Instrum., **30** (1959) 548.
25. K. Tahmasebi, A. Barzegar, J. Ding, T.S. Herng, A. Huang and S. Shannigrahi, Mater. Design, **32** (2011) 2370.

Chapter-III

Characterization of NZF-PZT Composites

Chapter–III

Characterization of NZF–PZT Composites

The experimental results of NZF–PZT composite system (series 1) are discussed in this chapter. Individual phases i.e. NZF phase ($Ni_{0.8}Zn_{0.2}Fe_2O_4$) and PZT phase ($PbZr_{0.65}Ti_{0.35}O_3$) were synthesized using conventional solid state reaction method. Phase confirmation for both phases was carried out using XRD analysis. Optimization of sintering temperature was done for $0.1Ni_{0.8}Zn_{0.2}Fe_2O_4–0.9PbZr_{0.65}Ti_{0.35}O_3$ composite sample. This sample was sintered at four different sintering temperatures (1100 ^oC, 1150 ^oC, 1200 ^oC and 1225 ^oC) for 4 hrs. It was found that the composite sample sintered at 1200 ^oC for 4 hrs exhibits very good dielectric, ferroelectric, piezoelectric and ferromagnetic properties.

Further studies on structural, microstructural, dielectric, ferroelectric, piezoelectric, ferromagnetic and magnetoelectric properties of $yNi_{0.8}Zn_{0.2}Fe_2O_4–(1–y)PbZr_{0.65}Ti_{0.35}O_3$ (y = 0, 0.05, 0.10, 0.15 and 1) were carried out. The studied composites are ferroelectric rich ferrite–ferroelectric composites with small content (5%, 10% and 15 %) of ferrite phase (NZF). The reason is that composites with higher ferrite content show lossy P–E loops due to relatively low resistivity of ferrite phase as compared to that for ferroelectric phase and are also difficult to pole. Higher value of ferrite content also results in lower magnetoelectric output due to the leakage charges developed in the ferroelectric grains which reduces the charges generated during magnetoelectric effect [1]. All samples were sintered at optimized sintering temperature 1200 ^oC for 4 hrs. Coexistence of individual phases was confirmed using XRD analysis. Dielectric properties were studied as a function of temperature as well as frequency presuming that the interactions between the individual phases may result in various anomalies in the dielectric properties of composites. There is a decrease in the dielectric constant values and increase in the loss tangent values with increase in ferrite content i.e. y. Room temperature P–E and M–H hysteresis loops were recorded to study ferroelectric and magnetic properties of composites respectively. Increase in P_r and P_s with increase in ferroelectric content and increase in M_r and M_s with increase in ferrite content show that these composites obey the rule of mixtures. Higher

values of M_r and M_s were observed for all electrically poled composite samples (y = 0.05, 0.10 and 0.15). Magnetoelectric coupling coefficients, α (mV/(cm.Oe)) were measured as a function of applied DC magnetic field. The measurement was performed in the presence of AC magnetic field of 10 Oe at 1 kHz. Change in magnetic properties (M_r and M_s) for electrically poled composite samples and generation of polarization by applying magnetic field are the evidences for magnetoelectric coupling in these composites. The maximum value of ME coupling coefficient of 6.67 mV/(cm.Oe) was observed for composite sample with y = 0.10.

3.1 Synthesis of Individual Phases

Our first objective was to select individual phases i.e. ferrite phase and ferroelectric phase exhibiting good ferromagnetic and ferroelectric properties respectively. $Ni_{0.8}Zn_{0.2}Fe_2O_4$ (NZF) composition for ferrite phase and $PbZr_{0.65}Ti_{0.35}O_3$ for ferroelectric phase was chosen as promising candidates for further studies as per literature survey (discussed in chapter I). These individual phases (ferrite and ferroelectric) were prepared by conventional solid state reaction route. AR grade NiO, ZnO and Fe_2O_3 for the ferrite phase were weighed in the required molar proportions. The mixing process was carried out by ball milling in distilled water using zirconia balls as the milling media. The dried powder was calcined at 1000 ^oC for 4 hrs. A small amount of MnO_2 (0.5% by weight) was added to the calcined powder as the sintering aid. The powder mixture was ball milled again, dried and then re–calcined at 1100 ^oC for 4 hrs. AR grade PbO, ZrO_2 and TiO_2 were used as raw materials for synthesis of the ferroelectric phase. An excess of 2% of PbO was added to compensate for lead loss during sintering. The powder mixture was ball milled, dried and then calcined at 800 ^oC for 4 hrs. After ball milling and drying, the powder mixture was re–calcined at 1000 ^oC for 4 hrs. Various steps involved in the synthesis of individual phases are shown in figure 2.1(a) (chapter II).

Phase identification for both phases was carried out using XRD analysis in a range of Bragg angles ($20^o \leq 2\theta \leq 70^o$). XRD patterns for individual phases (NZF and PZT) at room temperature are shown in figure 3.1. The patterns for NZF and PZT show well–defined peaks with specific indices (hkl) characteristic of spinel and perovskite structures respectively. This confirms the cubic spinel structure in the ferrite phase (NZF) and the perovskite structure in the

ferroelectric phase (PZT). The phase formation was confirmed by comparing the patterns with standard JCPDS card 52–0277 for NZF and 89–1279 for PZT.

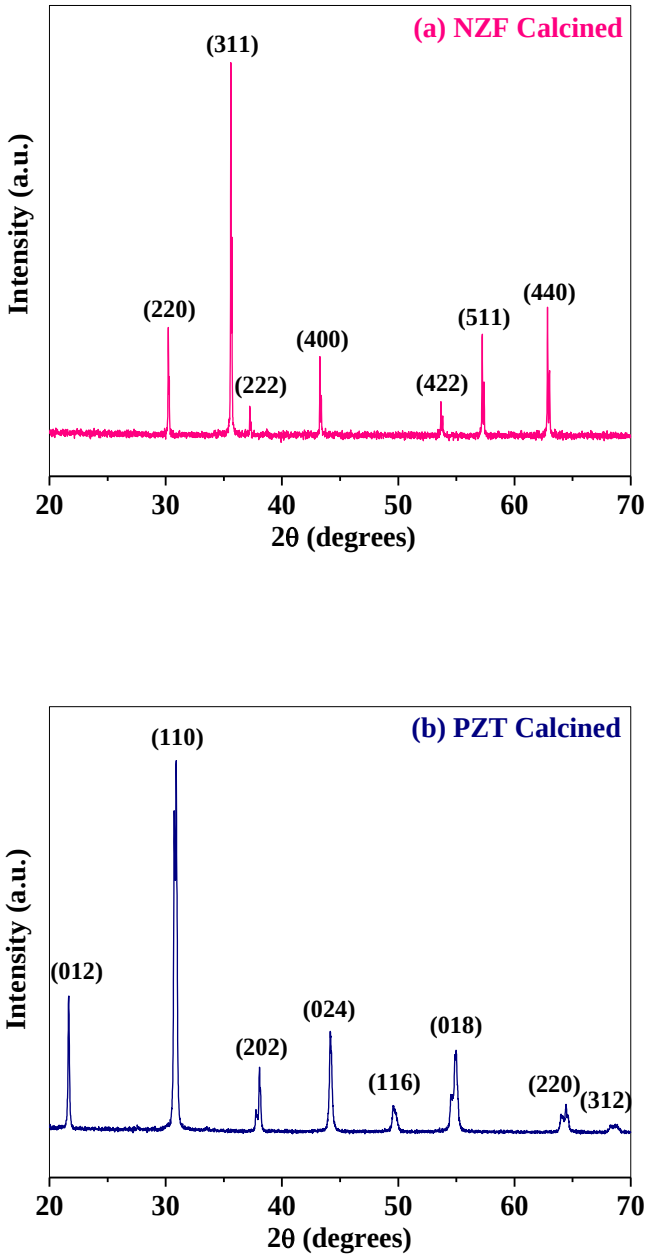

Figure 3.1 XRD patterns for (a) NZF and (b) PZT

3.2 $0.1Ni_{0.8}Zn_{0.2}Fe_2O_4$–$0.9PbZr_{0.65}Ti_{0.35}O_3$: Optimization of Processing Parameters and Sintering Temperature/Schedule

Ferroelectric–ferrite composites with general formula $yNi_{0.8}Zn_{0.2}Fe_2O_4$–$(1–y)PbZr_{0.65}Ti_{0.35}O_3$ (NZF–PZT) were prepared by mixing two phases in desired ratio. Powder mixture was ball milled in distilled water and then dried powder was mixed with small amount of diluted polyvinyl alcohol (3% by weight) as binder. This dried mixture was pressed into circular discs using uniaxial hydraulic press and were finally sintered in a programmable furnace. As sintering temperature significantly influences the system properties including phase evolution, microstructure and density of the material [2–4], particularly involving PZT due to volatile nature of PbO, hence, in order to find out optimum sintering temperature, the green bodies were sintered at four different sintering temperatures viz. 1100 ^oC, 1150 ^oC, 1200 ^oC and 1225 ^oC for 4 hrs in lead rich atmosphere to minimize lead loss during sintering. The optimization of sintering temperature was done for $0.1Ni_{0.8}Zn_{0.2}Fe_2O_4$–$0.9PbZr_{0.65}Ti_{0.35}O_3$ (0.1NZF–0.9PZT) and this composition was considered as the starting point for further research. Various steps involved in the synthesis of composites are shown in figure 2.1(b) (chapter II).

XRD patterns of 0.1NZF–0.9PZT composite sintered at different sintering temperatures were recorded and shown in figure 3.2. The analysis shows that XRD patterns for samples sintered at 1100 ^oC, 1150 ^oC and 1200 ^oC have well defined diffraction peaks with specific indices confirming the coexistence of cubic spinel structure in ferrite phase (NZF) and rhombohedral perovskite structure in ferroelectric phase (PZT). No diffraction peak other than the constituent phases was observed confirming that no chemical reaction took place between the individual phases during sintering. Intensity of peaks corresponding to ferrite phase is very small which is due to small concentration of ferrite phase as compare to ferroelectric phase. As sintering temperature is increased to 1225 ^oC, an additional diffraction peak other than NZF and PZT phases was found at a 2θ value around 28.2^o. The appearance of this extra phase suggests that any chemical reaction occurred between NZF and PZT phases during the sintering process. This sample (sintered at 1225 ^oC for 4 hrs) was not studied further because the presence of extra phase in composite would deteriorate the magnetoelectric effect [5].

With increase in sintering temperature, the diffraction peaks corresponding to both phases are found to be slightly shifting towards lower angle side indicating an increase in lattice constants (table 3.1). The experimental density (determined by Archimedes Principle), X–ray density and relative density were calculated using formulae discussed in chapter II and their values are summarized in table 3.1. It is observed that densification increases with increase in sintering temperature which may be due to grain growth with rise in sintering temperature and better compaction of grains together.

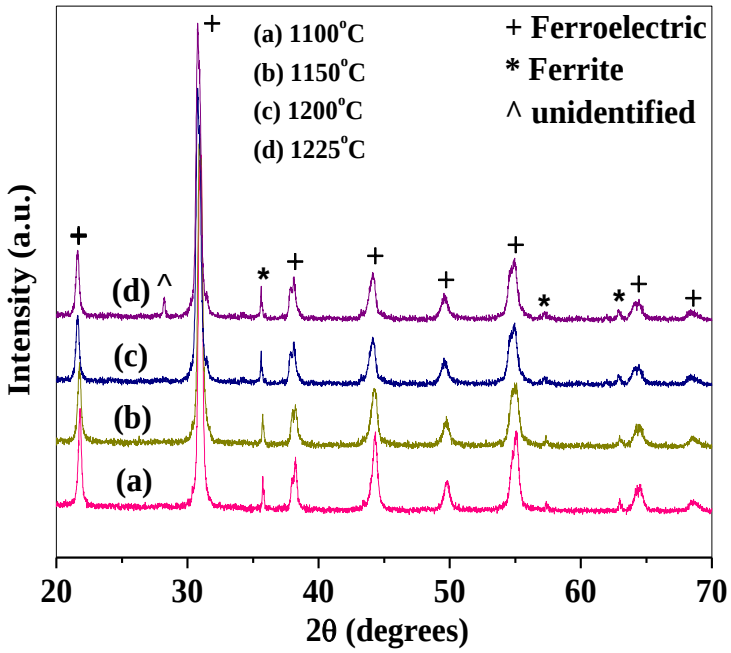

Figure 3.2 XRD patterns for 0.1NZF–0.9PZT composite at different sintering temperatures

Figure 3.3 shows the comparison of temperature dependence of dielectric properties (dielectric constant and loss) of 0.1NZF–0.9PZT composite sample at 100 kHz for different sintering temperatures. It was observed that dielectric constant (ε') is maximum and loss (tanδ) is minimum for the sample sintered at 1200 ^{o}C. The values of ferroelectric Curie temperature (T_c), room temperature dielectric constant (ε'_{RT}), room temperature dielectric loss ($\tan\delta_{RT}$), dielectric

constant at T_c (ε'_{max}) and dielectric loss at T_c ($\tan\delta_{max}$) at 100 kHz for all the samples are given in table 3.2.

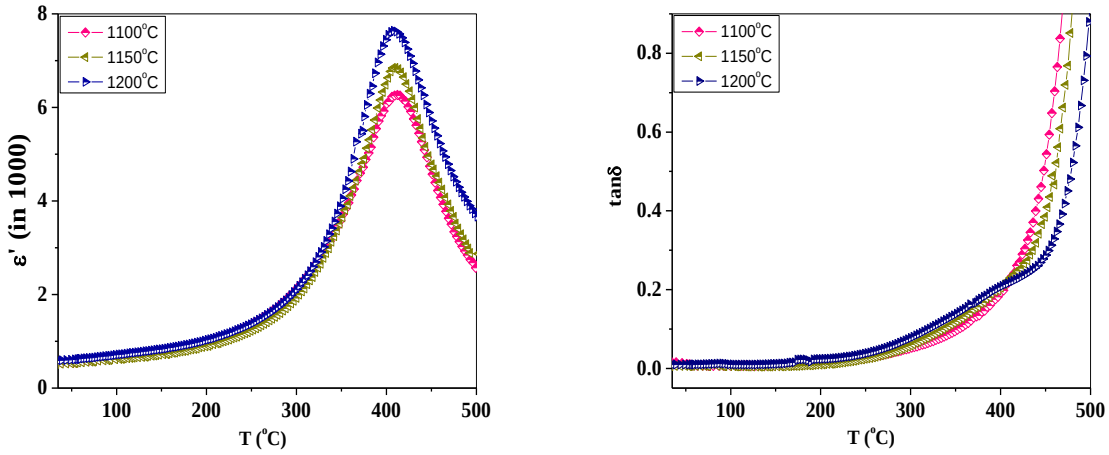

Figure 3.3 Comparison of temperature dependence of dielectric constant (ε') and loss (tanδ) of 0.1NZF–0.9PZT composite for different sintering temperatures at 100 kHz

Table 3.1 Structural parameters of 0.1NZF–0.9PZT composite at different sintering temperatures

Sintering Temperature	**1100 °C**	**1150 °C**	**1200 °C**
Lattice Constant (Å) (Ferroelectric phase)	4.083	4.084	4.104
Lattice Constant (Å) (Ferrite phase)	8.324	8.326	8.353
Exp. Density (g/cc)	6.46	6.80	6.88
X–ray Density (g/cc)	7.81	7.80	7.75
Relative Density (%)	82.7	87.2	88.8

Table 3.2 Dielectric and piezoelectric parameters of 0.1NZF–0.9PZT at 100 kHz

Sintering Temperature (^oC)	**T_c (^oC)**	**ε'_{RT}**	**ε'_{max}**	**$tan\delta_{RT}$**	**$tan\delta_{max}$**	**d_{33} (pC/N)**
1100	412	540	6265	0.02	0.23	44
1150	410	515	6840	0.01	0.22	57
1200	408	590	7635	0.01	0.21	72

To study ferroelectric ordering in 0.1NZF–0.9PZT composite sample, room temperature P–E hysteresis loops were recorded at 20 Hz. Composite sample sintered at 1100 ^oC shows a lossy loop (not shown here). Figure 3.4 depicts P–E hysteresis behavior of 0.1NZF–0.9PZT composite sample sintered at 1150 ^oC and 1200 ^oC. Increase in remanant polarization (P_r) and saturation polarization (P_s) was observed for the sample sintered at 1200 ^oC as compared to that for 1150 ^oC. Increase in values of piezoelectric charge coefficient (d_{33}) with increase in sintering temperature was also observed (table 3.2). To confirm magnetic ordering, M–H hysteresis loops were taken and are shown in figure 3.5.

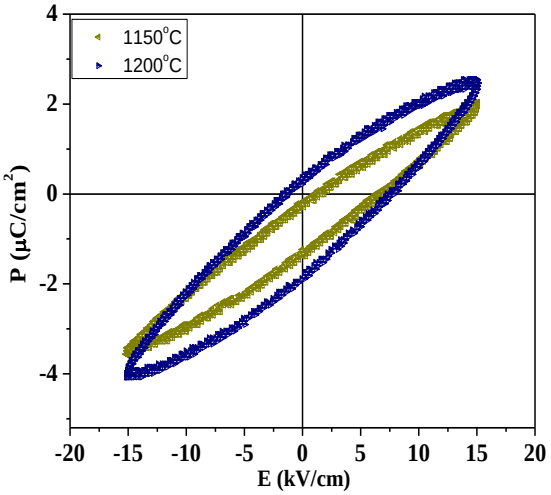

Figure 3.4 P–E hysteresis loops of 0.1NZF–0.9PZT composite samples at different sintering temperatures

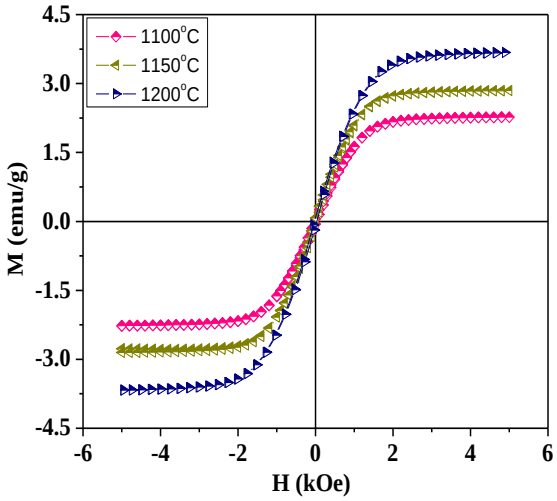

Figure 3.5 M–H hysteresis loops of 0.1NZF–0.9PZT composite samples at different sintering temperatures

From the results, it can be concluded that sintering temperature significantly affects the material properties. Relative density, dielectric constant (ε'), remanant polarization (P_r), saturation polarization (P_s), piezoelectric coefficient (d_{33}), remanant magnetization (M_r) and saturation magnetization (M_s) were observed to be maximum for the sample sintered at 1200 ^oC and dielectric loss (tanδ) is minimum. Hence, the 1200 ^oC temperature was chosen as the optimized sintering temperature for further studies.

3.3 Synthesis and Characterization of $yNi_{0.8}Zn_{0.2}Fe_2O_4–(1–y)PbZr_{0.65}Ti_{0.35}O_3$

A study on structural, dielectric, ferroelectric, piezoelectric, magnetic and magnetoelectric properties of sintered PZT (y = 0), NZF (y = 1) and yNZF–(1–y)PZT composites (where, y = 0.05, 0.10 and 0.15) was carried out to explore their properties. All samples were sintered by conventional solid state reaction route at optimized sintering temperature, 1200 ^oC for 4 hrs.

3.3.1 X–Ray Diffraction

Figure 3.6 shows the XRD patterns for pure ferroelectric sample (y = 0), pure ferrite sample (y = 1) and their composites (y = 0.05, 0.10 and 0.15) at room temperature. The patterns for PZT (y = 0) and NZF (y = 1) show well–defined peaks with specific indices characteristic of rhombohedral perovskite and cubic spinel structures respectively. The diffraction peaks for composite samples (y = 0.05, 0.10 and 0.15) confirm the perovskite structure in the ferroelectric phase (PZT) and the cubic spinel structure in the ferrite phase (NZF). No extra peaks other than the constituent phases were observed in XRD patterns of composite samples which confirm that no chemical reaction took place between the two phases (NZF and PZT) during sintering. A comparison between the XRD patterns of composites reveals that there is an increase in the intensity of peaks corresponding to ferrite phase with increase in ferrite content. The number of peaks corresponding to the ferrite phase also increases with increase in ferrite content.

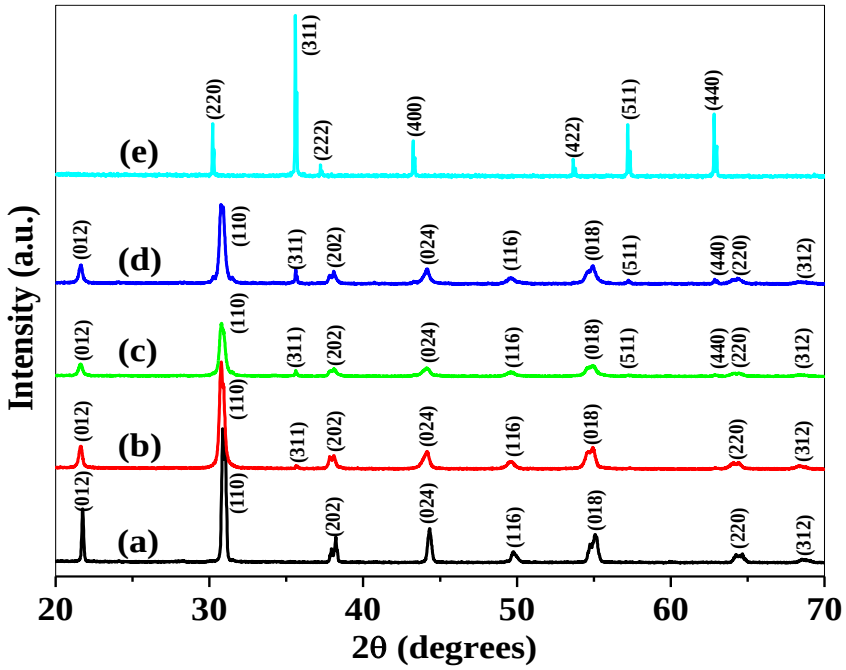

Figure 3.6 XRD patterns for yNZF–(1–y)PZT (a) y = 0 (b) y = 0.05 (c) y = 0.10 (d) y = 0.15 and (e) y = 1 at room temperature

The lattice constants for both phases are given in table 3.3. These values are in well consistence with the constituent phases suggesting the absence of any structural change in composites with compositional changes. Further, the values of lattice constants corresponding to the constituent phases in composite samples are found to be slightly different as compared to the individual phases which may be attributed to the stresses induced by individual phases on each other. The experimental density has been measured by Archimedes principle as discussed in chapter II. The experimental density, X–ray density and relative density for all the samples were calculated and are given in table 3.3. Comparison shows that there is decrease in density with increase in ferrite content (y) which is due to low density of NZF (y = 1) as compared to PZT (y = 0). However, the composite with y = 0.15 has slightly higher value of relative density which may be due to better compaction and sinterability [6].

3.3.2 Scanning Electron Microscope

A study of microstructure is necessary to understand the chemical homogeneity, atomic arrangement, grain morphology and size. It also helps in investigating the effect of substituent content on microstructure and provides useful information for further investigation of other electrical properties such as dielectric, ferroelectric and piezoelectric properties. Scanning electron micrographs of the freshly broken surfaces of all the sintered samples were taken and are shown in figure 3.7. In all micrographs, grains of different sizes with well defined grain boundaries were observed. The average grain size was calculated for all samples using linear intercept method and values are given in table 3.3. Average grain size for pure ferroelectric sample (y = 0) and pure ferrite sample (y = 1) was observed to be 2.3 μm and 1.2 μm respectively. In micrographs of composite samples (y = 0.05, 0.10 and 0.15), it is difficult to differentiate NZF and PZT phases because the amount of NZF (y) is small.

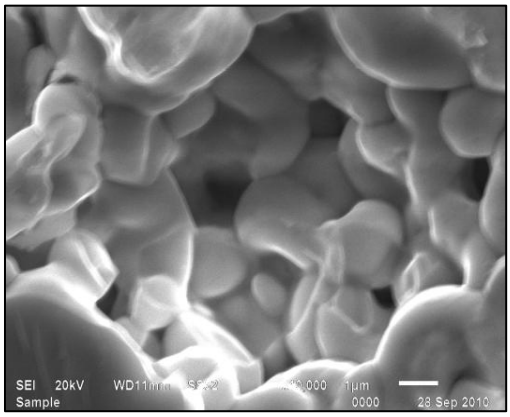

(a)

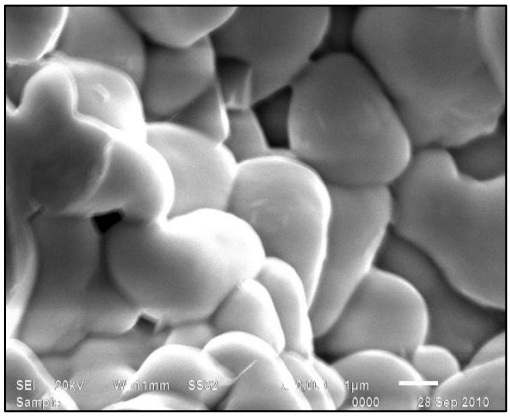

(b)

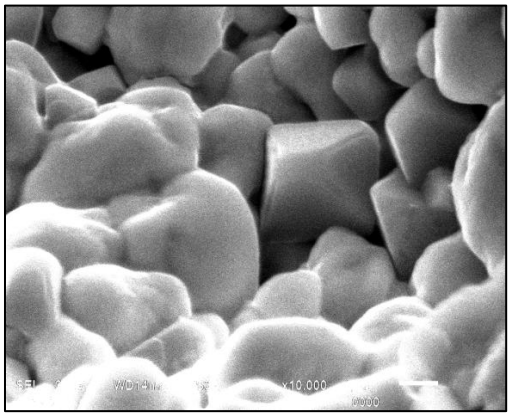

(c)

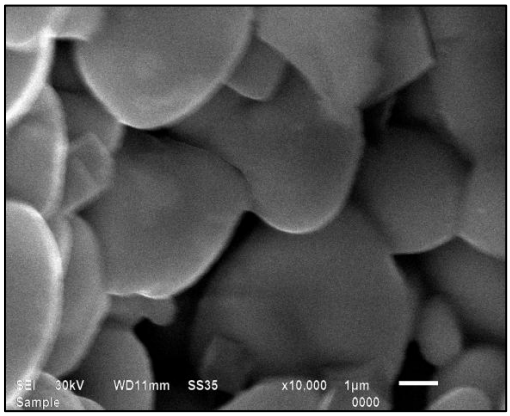

(d)

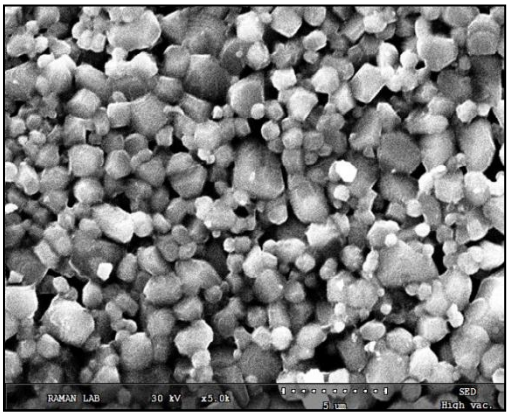

(e)

Figure 3.7 SEM micrographs for yNZF–(1–y)PZT (a) y = 0 (b) y = 0.05 (c) y = 0.10 (d) y = 0.15 and (e) y = 1

Table 3.3 Structural parameters of $yNi_{0.8}Zn_{0.2}Fe_2O_4–(1–y)PbZr_{0.65}Ti_{0.35}O_3$

y	**0**	**0.05**	**0.10**	**0.15**	**1**
Lattice Constant (Å) (Ferroelectric phase)	4.093	4.106	4.104	4.108	–
Lattice Constant (Å) (Ferrite phase)	–	8.346	8.353	8.353	8.361
Exp. Density (g/cc)	7.58	7.31	6.88	6.78	4.63
X–ray Density (g/cc)	8.02	7.89	7.75	7.62	5.36
Relative Density (%)	94.5	92.7	88.8	89.0	86.4
Avg. Grain Size (µm)	2.3	2.5	2.4	3.2	1.2

3.3.3 Dielectric Properties

Dielectric properties are measured as a function of temperature (35–500 ^oC) at three discrete frequencies (1, 10 and 100 kHz). The typical variation in the dielectric constant (ε') and loss (tanδ) with temperature for pure PZT (y = 0), pure NZF (y = 1) and NZF–PZT composites (y = 0.05, 0.10 and 0.15) are shown in figures 3.8(a)–(e) respectively. For y = 0, initially the dielectric constant increases with increase in temperature and attains a maximum value (dielectric maxima, ε'_{max}) at the ferroelectric Curie temperature (T_c) and then decreases with further increase in the temperature. A dielectric dispersion is observed near and above T_c. The position of dielectric maxima does not change with frequency indicating characteristics of normal ferroelectrics [7].

For y = 1, an increase in the value of dielectric constant is observed with increase in temperature which is typical behavior of ferrites. This increase in the dielectric constant at high temperatures is due to an increase in the dielectric polarization which is a result of thermally–activated electron exchange interactions ($Fe^{+2} \leftrightarrow Fe^{+3}$ and $Ni^{+2} \leftrightarrow Ni^{+3}$). Further, this increase is quite significant at lower frequency (1 kHz). It is known that there are four main contributions to the polarization in ferroelectrics and ferrites viz. interfacial, dipolar, ionic and electronic [8]. At

lower frequency, only interfacial and dipolar polarizations play dominant role and both are temperature dependent. Interfacial polarization is known to increase with increase in temperature and dipolar polarization decreases with increase in temperature. The observed increase in dielectric constant with temperature at lower frequency is supporting the fact that interfacial polarization is more pronounced [9]. Similar behavior is observed for dielectric loss with temperature at different frequencies as that for dielectric constant. The observed temperature dependence is consistent with Debye's equation for dielectric constant and loss [8].

For NZF–PZT composites (y = 0.05, 0.10 and 0.15), a maximum in dielectric constant is observed at all frequencies which corresponds to ferroelectric–paraelectric transition in ferroelectric phase (PZT). For all composites, dielectric dispersion is clearly observed over a wide range of temperature around T_c. Also, the dielectric peaks get broadened and suppressed with increase in ferrite content (y). This is due to the microstructural inhomogeneity created by addition of ferrite phase (non–ferroelectric phase) to the ferroelectric phase [10]. In the paraelectric region, it is observed that there is an increase in the dielectric constant with increase in the temperature for y = 0.10 and 0.15 and this increase is more pronounced for y = 0.15. But with an increase in the measurement frequency this observed behavior gradually reduces showing that it could be related to a low frequency relaxation process [11]. This increase in dielectric constant at high temperatures is due to an increase in the dielectric polarization which is a result of thermally–activated electron hopping between $Fe^{+2} \leftrightarrow Fe^{+3}$ ions as well as $Ni^{+2} \leftrightarrow Ni^{+3}$ ions present in the ferrite phase.

Figure 3.9 shows the comparison of temperature dependence of the dielectric constant and loss at 100 kHz for y = 0, 0.05, 0.10 and 0.15. The higher values of the loss are observed at high temperatures which may be attributed to the thermal conductivity losses. The values of ferroelectric Curie temperature (T_c), room temperature dielectric constant (ε'_{RT}), room temperature dielectric loss ($\tan\delta_{RT}$), dielectric constant at T_c (ε'_{max}) and dielectric loss T_c ($\tan\delta_{max}$) at 100 kHz for all the samples are given in table 3.4. There is a decrease in the dielectric constant and increase in the loss with increase in the ferrite concentration and is already reported by many researchers [12–14] indicating that composites obey mixture rule.

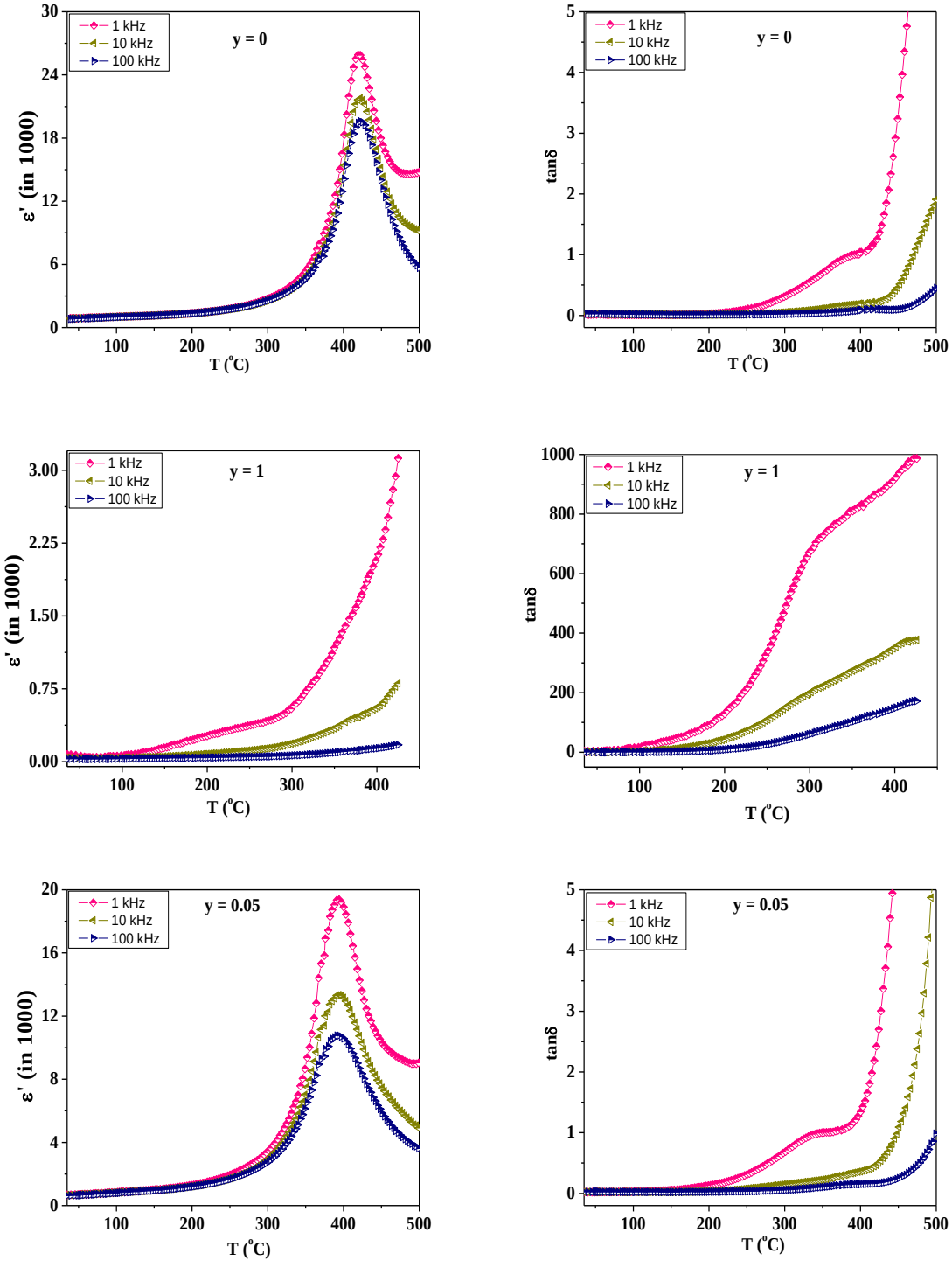

Figure 3.8 Temperature dependence of ε' and tanδ for PZT (y = 0), NZF (y = 1) and NZF–PZT composites (y = 0.05, 0.10 and 0.15) at 1, 10 and 100 kHz (continued)

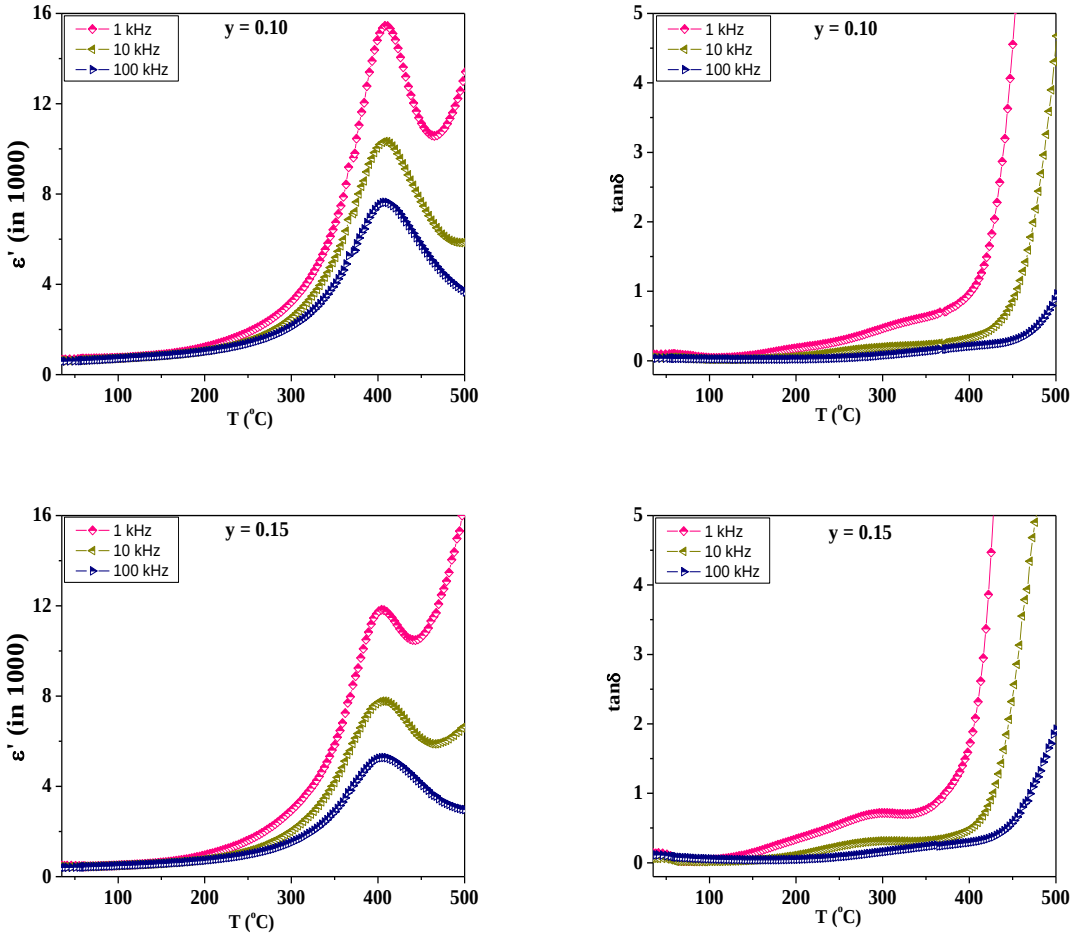

Figure 3.8 Temperature dependence of ε' and tanδ for PZT (y = 0), NZF (y = 1) and NZF–PZT composites (y = 0.05, 0.10 and 0.15) at 1, 10 and 100 kHz

The variation of dielectric constant and loss with frequency at room temperature was also studied for all the samples and is shown in figure 3.10. The general trend for all samples is that ε' and tanδ decrease with increase in frequency. This decrease is rapid for the lower frequency region because as the frequency increases, dipolar and ionic polarizations decrease. Higher values of dielectric constant at lower frequencies may be the result of space charge polarization because of inhomogeneity in the structure [15]. However, in case of composites, the higher values of the dielectric constant can be explained on the basis of the fact that ferroelectric regions are surrounded by non–ferroelectric regions (ferrite grains) similar to that in relaxor

ferroelectrics [16]. A similar dispersion to that of the dielectric constant is observed in the case of the dielectric loss with frequency.

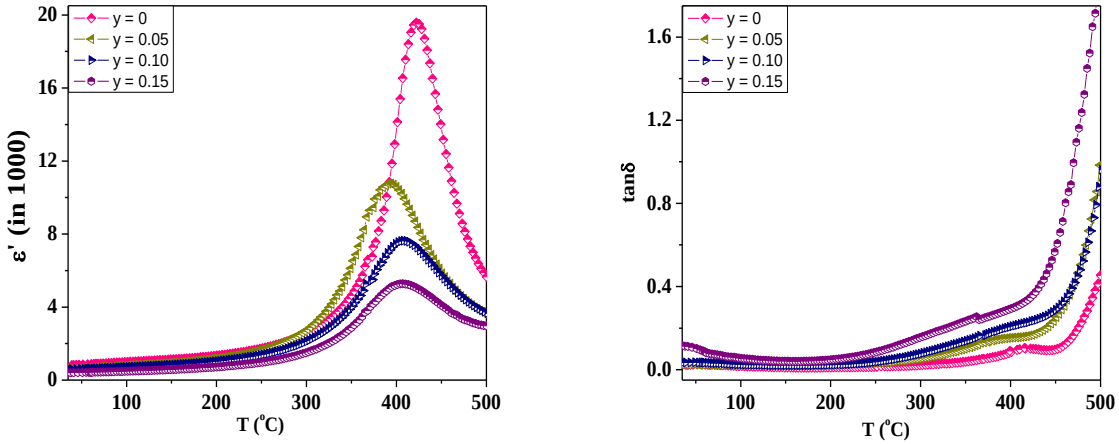

Figure 3.9 Temperature dependence of dielectric properties for yNZF–(1–y)PZT (y = 0, 0.05, 0.10 and 0.15) at 100 kHz

Table 3.4 Variation of T_c, ε'_{RT}, ε'_{max}, $\tan\delta_{RT}$ and $\tan\delta_{max}$ for different values of y at 100 kHz

y	**0**	**0.05**	**0.10**	**0.15**
T_c (°C)	422	394	408	407
ε'_{RT}	820	625	590	405
ε'_{max}	19585	10760	7635	5275
$\tan\delta_{RT}$	0.02	0.03	0.03	0.12
$\tan\delta_{max}$	0.10	0.15	0.22	0.31

Further with increase in ferrite content (y), dielectric dispersion increases. This behavior may be explained qualitatively by the supposition that the polarization process in ferrites is similar to that of the conduction process. There is a strong correlation between the conduction

mechanism and dielectric properties of ferrites [17]. For the present system, conduction mechanism in ferrites can be explained by the electron hopping between $Fe^{+2} \leftrightarrow Fe^{+3}$ ions as well as $Ni^{+2} \leftrightarrow Ni^{+3}$ ions. These electron exchange interactions result in local displacement of electrons in the direction of the applied electric field and determine the polarization in ferrites. It is also known that the effect of polarization is to reduce the field inside the medium [18], thereby lowering the dielectric constant at higher frequencies.

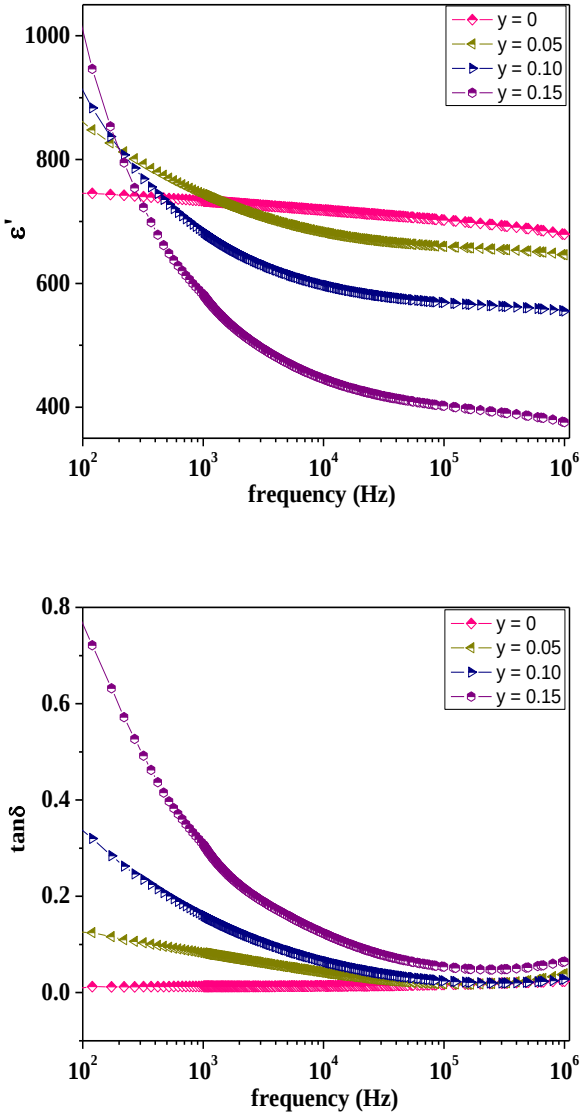

Figure 3.10 Frequency dependence of dielectric properties for yNZF–(1–y)PZT (y = 0, 0.05, 0.10 and 0.15) at 100 kHz at room temperature

The AC conductivity of the samples was calculated from the dielectric parameters using the following formula:

$$\sigma_{AC} = \omega \varepsilon' \varepsilon_o \tan\delta \quad \ldots. (3.1)$$

Where ω is the angular frequency, ε_o is the permittivity of free space, ε' is the dielectric constant and tanδ is the dielectric loss. Variation of AC conductivity with frequency is studied and shown in figure 3.11. The plots of $\ln\sigma_{AC}$ vs frequency are linear for all the samples and AC conductivity is increasing with increase in frequency indicating small polaron hopping conduction mechanism [19].

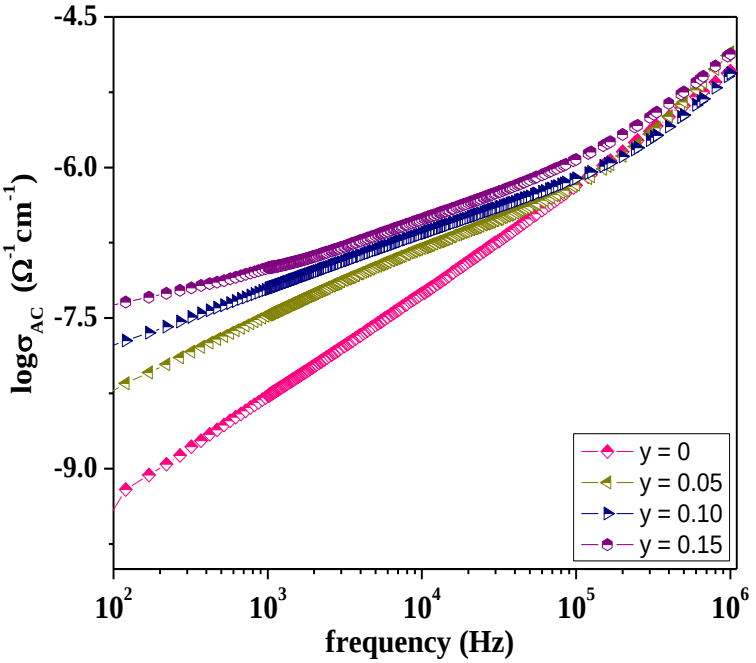

Figure 3.11 Variation of AC conductivity with frequency for yNZF–(1–y)PZT (y = 0, 0.05, 0.10 and 0.15) at 100 kHz

3.3.4 Ferroelectric Properties

To study ferroelectric behavior of composites, room temperature P–E hysteresis loops were recorded for PZT (y = 0) and NZF–PZT composites (y = 0.05, 0.10 and 0.15) at different electric fields (figure 3.12). The hysteresis loops for y = 0, 0.05 and 0.10 confirm well defined ferroelectric behavior. But the composite sample with y = 0.15 shows lossy loop (broader at the tip and more wide as compared to that for y = 0.05 and 0.10) and indicating high leakage current in the sample due to presence of ferrite phase having high conductivity as compared to ferroelectric phase [20]. It is observed that the loops for composite samples are slightly asymmetric and this asymmetry increases with increase in ferrite content (y) which may be due to internal bias field developed in the ferroelectric phase, electrode/PZT interface or due to defects present in the sample [21]. This asymmetry behavior can easily be seen in P–E hysteresis loop for y = 0.15. A comparison of P–E plots (figure 3.12(e)) reveals that both the remanant polarization (P_r) and saturation polarization (P_s) decrease with increase in ferrite content i.e. ferroelectric behavior is weakening which may be due to low internal polarizability [22] because ferrite particles with spinel structure are distributed along the circumference of ferroelectric phase resulting in low polarization values. The values of P_r and P_s obey the rule of mixtures i.e. go on decreasing with decrease in ferroelectric content.

The values of remanant polarization (P_r), saturation polarization (P_s) and coercive field (E_c) for y = 0, 0.05 and 0.10 at different applied electric fields were compared and are shown in figure 3.13. For y = 0 (pure ferroelectric phase), as the applied field increases from 15 kV/cm to 25 kV/cm, there is increase in P_r (from 8 $\mu C/cm^2$ to 26 $\mu C/cm^2$), P_s (from 17 $\mu C/cm^2$ to 45 $\mu C/cm^2$) and E_c (from 5.3 kV/cm to 7.2 kV/cm). For further increase in applied field (at 30 kV/cm), no change was observed for y = 0 i.e. with increase in applied field, the polarization first increases and thereafter reaches to a saturation value. But for composite samples (y = 0.05 and 0.10), there is continuous increase in ferroelectric parameters and no saturation was observed up to 35 kV/cm. Increase in the values of coercive field was also observed with increase in ferrite content which is due to clamping effect derived from the ferrite phase (non–ferroelectric) [23].

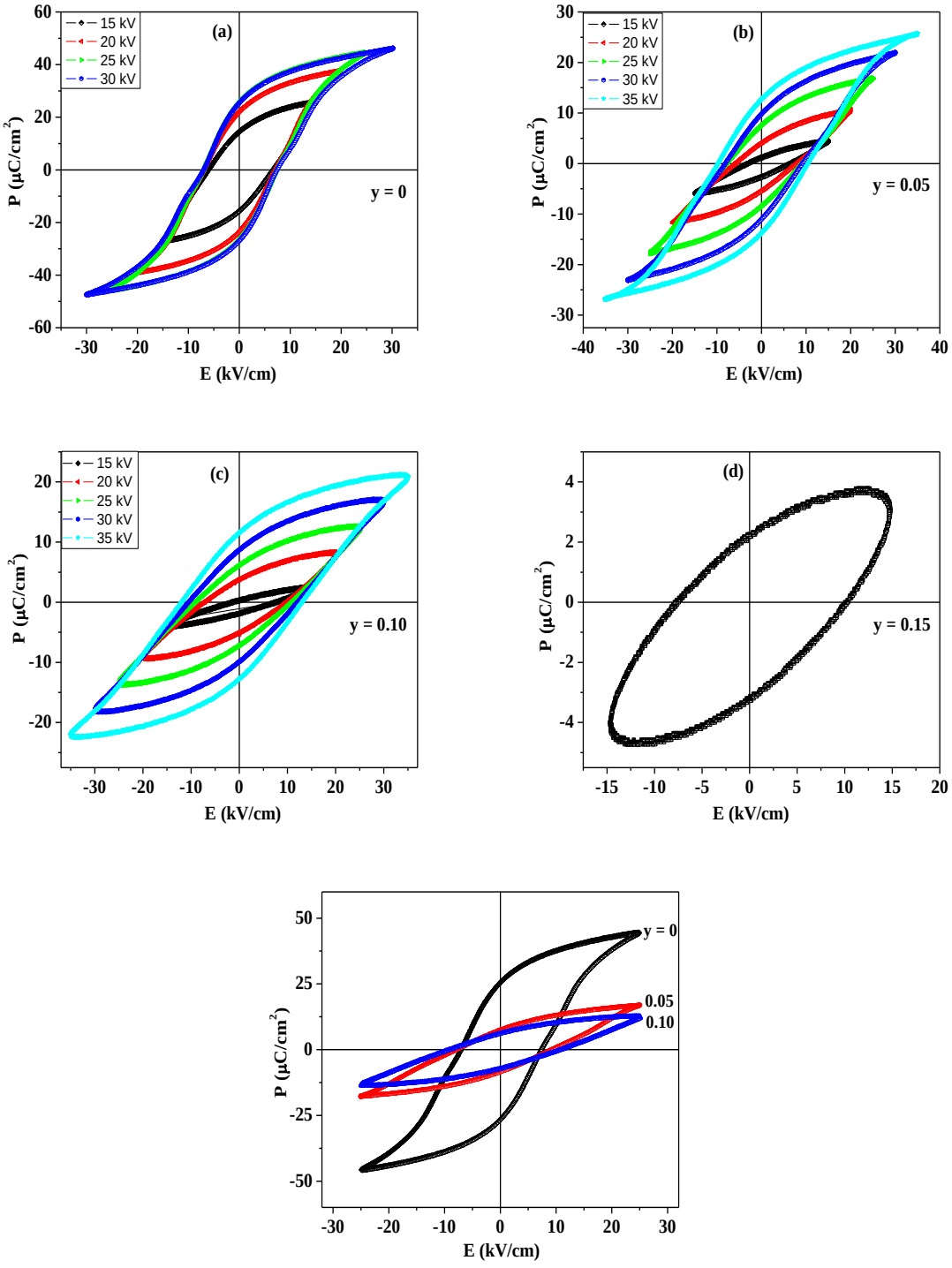

Figure 3.12 Room temperature P–E hysteresis loops for (a) y = 0 (b) y = 0.05 (c) y = 0.10 and (d) y = 0.15 at different maximum electric fields (e) comparison of P–E loops for y = 0, 0.05 and 0.10 at 25 kV

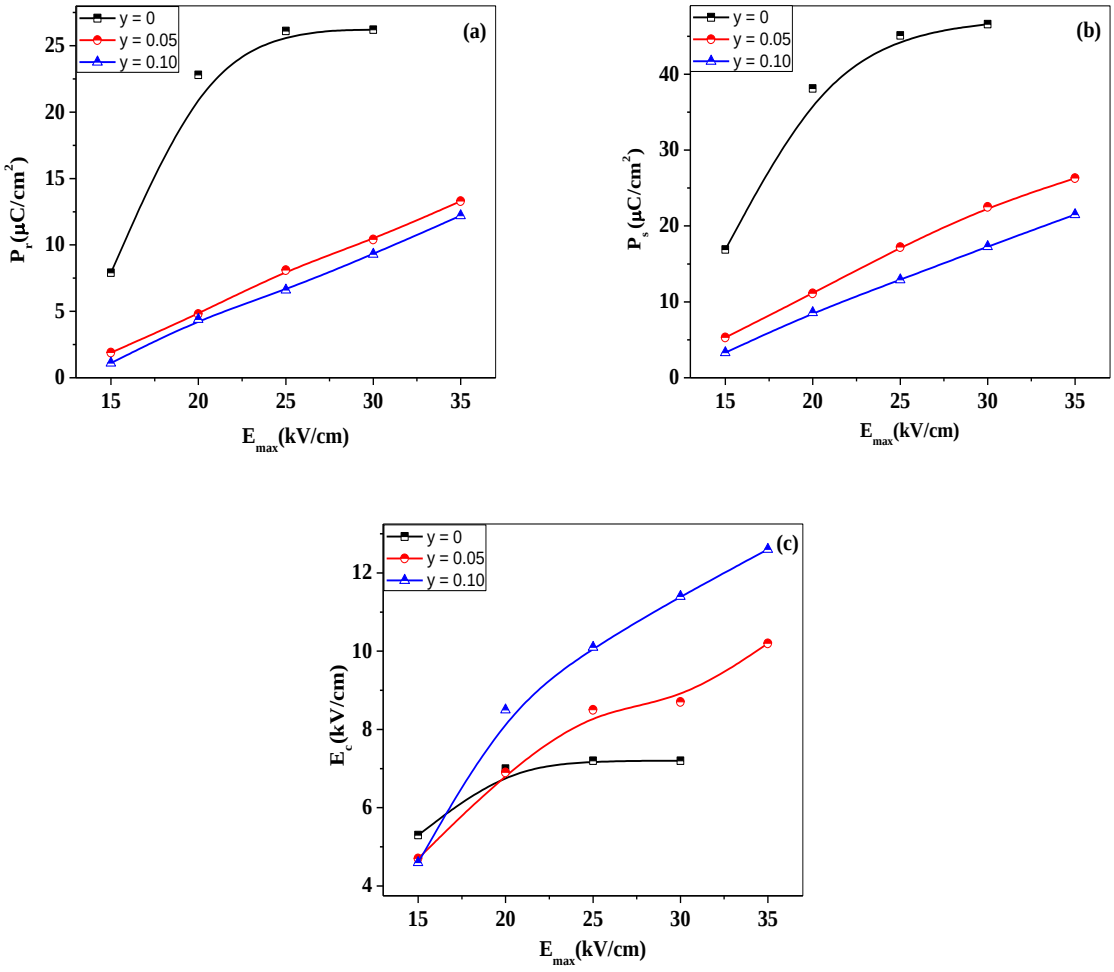

Figure 3.13 Variation of (a) P_r (b) P_s and (c) E_c with maximum applied electric field for y = 0, 0.05 and 0.10

3.3.5 Piezoelectric Properties

The piezoelectric charge coefficient (d_{33}) depends on composition and microstructure which is controlled by sintering temperature [24]. Apart from the intrinsic parameters, other parameters like domain wall motion, grain size, electrostrictive constants, dielectric constants and spontaneous polarization also play an important role in determining the piezo–coefficients [25, 26]. In order to perform piezoelectric measurement, samples were poled under a DC field of 15 kV/cm for 1 hr in a silicon oil bath at 150 ^{o}C. Values of piezoelectric charge coefficient (d_{33})

for pure PZT (y = 0) and NZF–PZT composites (y = 0.05, 0.10 and 0.15) are given in table 3.5. The gradual decrease has been observed in d_{33} with increase in NZF content (y). Charge coefficient, d_{33} attains a maximum value of 108 pC/N for pure PZT and thereafter d_{33} value exhibits a diminishing trend. Decrease in d_{33} values with increase in NZF content (y) is due to decrease in piezoelectric phase (PZT) [27]. Further, relatively high conductivity of NZF phase makes the poling process more difficult due to increase in leakage current which leads to the loss of induced voltage and hence d_{33} values decrease [28].

3.3.6 Ferromagnetic Properties

Figure 3.14 shows M–H hysteresis loops for composites (y = 0.05, 0.10 and 0.15) and pure NZF (y = 1) at room temperature. All the samples show well defined ferromagnetic behavior confirming the existence of magnetic ordering in pure NZF sample as well as in mixed ferrite–ferroelectric (NZF–PZT) composite system. Figure 3.15(a) shows comparison of M–H hysteresis loops for composite samples (y = 0.05, 0.10 and 0.15) measured at room temperature. Comparison of M–H loops shows that saturation in loops shifts towards high field [29] with increase in ferrite content (y) because in composites, M–H hysteresis loops are obtained due to presence of NZF as magnetic phase and PZT as non–magnetic phase.

The values of remanant magnetization (M_r), saturation magnetization (M_s) and coercive field (H_c) determined from M–H hysteresis loops are listed in table 3.5. Increase in remanant magnetization (M_r) and saturation magnetization (M_s) with increase in ferrite content (y) is observed i.e. magnetic parameters also obey the rule of mixtures. However, the value of coercive field (H_c) remains almost same for all samples indicating absence of any intermediate phase due to interdiffusion as is evident from XRD analysis (section 3.3.1).

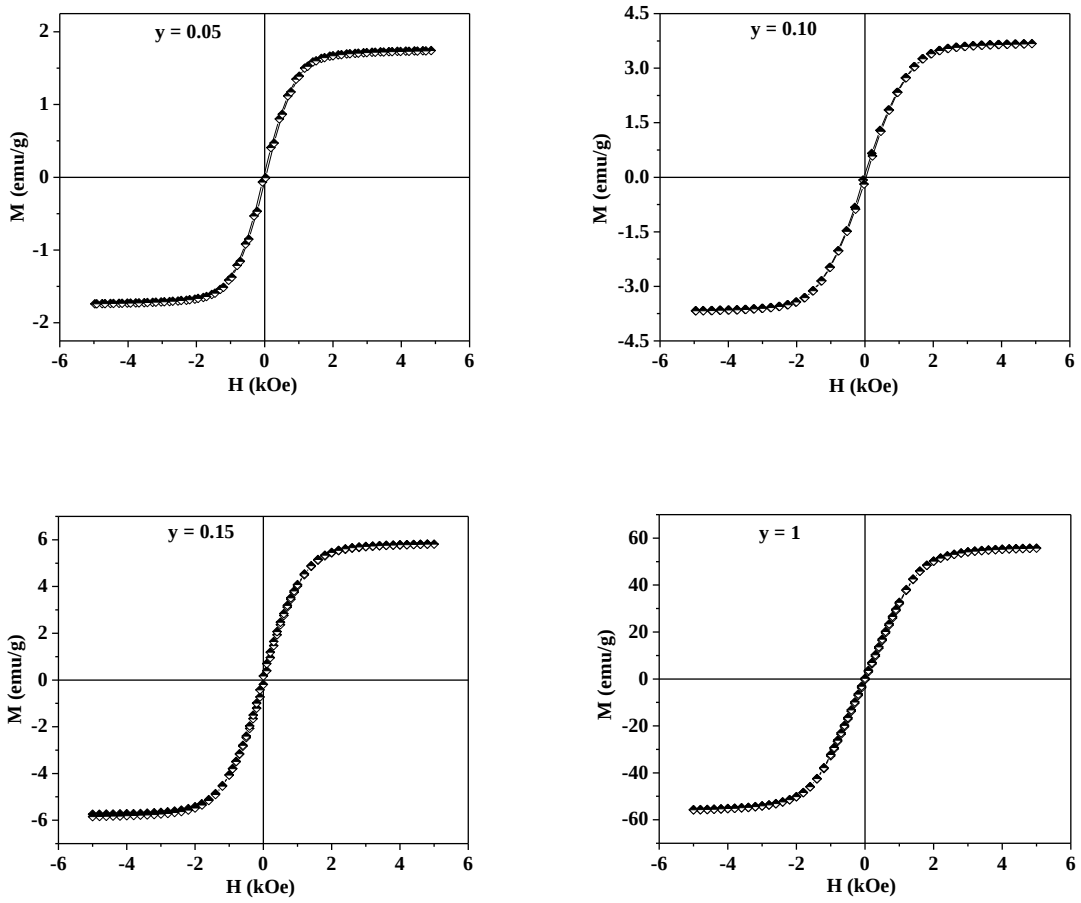

Figure 3.14 M–H hysteresis curve (a) y = 0.05 (b) y = 0.10 (c) y = 0.15 and (d) y = 1

3.3.7 Magnetoelectric Properties

To study the effect of electric poling on ferromagnetic properties in composites, two pieces from a single pellet were taken. One piece from each composite sample was electrically poled at 15 kV/cm and room temperature M–H hysteresis loops were recorded for both electrically poled and unpoled pieces of composite samples and comparison is shown in figure 3.15(b)–(d). It can easily be observed that, there is increase in remanant magnetization and saturation magnetization for electrically poled samples which is the evidence of ME coupling. This enhancement for electrically poled samples further increases with increase in ferrite content.

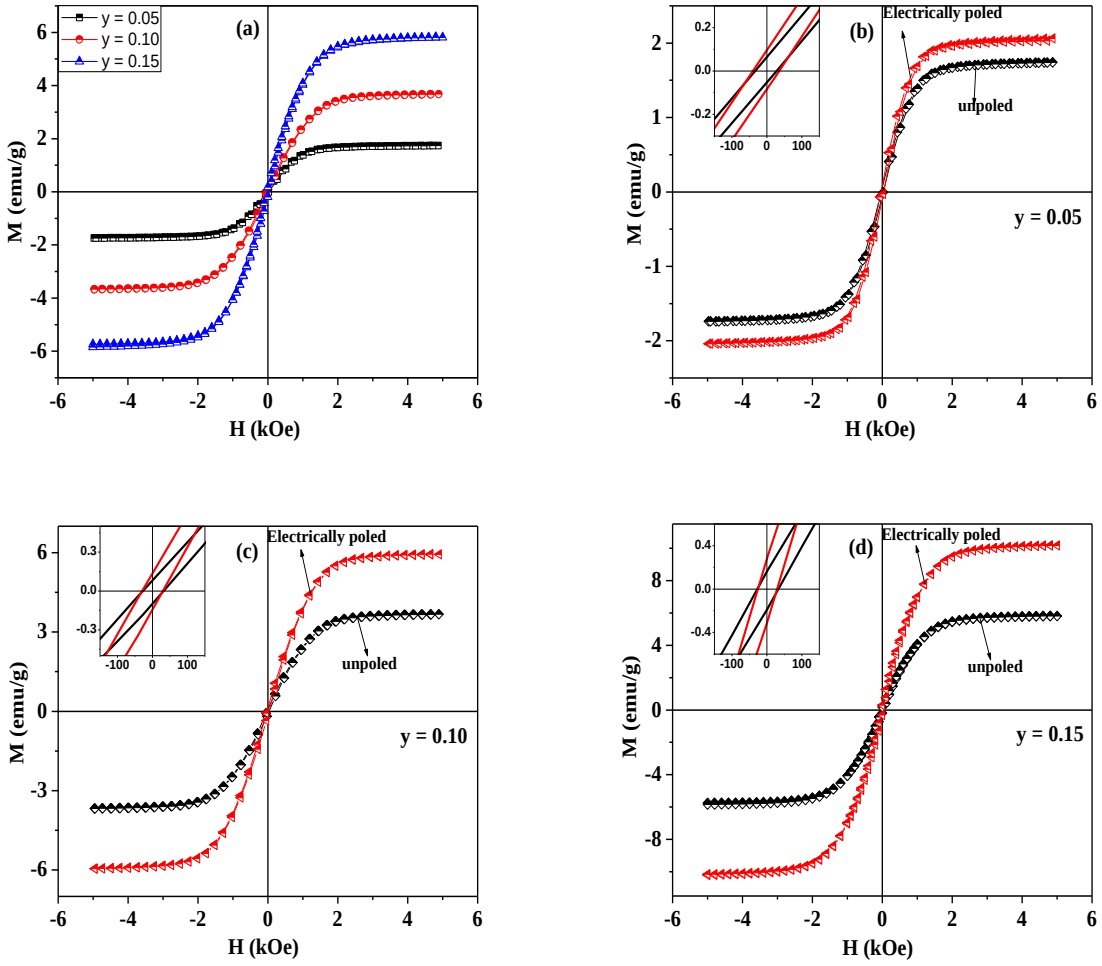

Figure 3.15 (a) Comparison of M–H loops for y = 0.05, 0.10 and 0.15, M–H loops for electrically poled and unpoled samples for (b) y = 0.05 (c) y = 0.10 and (d) y = 0.15

The coexistence of magnetostriction of NZF phase and piezoelectricity of PZT phase in composites give rise to magnetoelectric coupling which depends on the applied magnetic field and mole percentage of ferrite (NZF) and ferroelectric (PZT) phases in composites [30]. The variation of ME coupling coefficient, α (mV/(cm.Oe)) with applied DC magnetic field for all composite samples is shown in figure 3.16. The experiment was performed in the presence of AC magnetic field of 10 Oe at 1 kHz. All the samples responded well to the change in DC magnetic field. The maximum value for ME coupling coefficients appears in the range of 800–

1000 Oe. ME coupling coefficient first increases steeply for lower values of magnetic field, reaches to maximum and thereafter decreases for higher values of magnetic field for all samples. This behavior is already reported by a number of research groups [31–36].

This appearance of ME output in ferrite–ferroelectric composites by applying magnetic field is due to the strain induced in ferrite phase (magnetostriction) which results in generation of charge in ferroelectric phase (piezoelectricity). After a certain value of applied magnetic field, there is saturation in strain induced lattice distortions resulting in almost constant values of electric field in piezoelectric phase and decrease in ME coupling coefficient values [37, 38]. Further, maximum value of magnetoelectric coupling coefficient was found to be affected by compositional changes. Maximum values of 3.8 mV/(cm.Oe), 6.7 mV/(cm.Oe) and 4.1 mV/(cm.Oe) were observed for composite samples with y = 0.05, 0.10 and 0.15 respectively. Increase in α for y = 0.10 as compared to that for y = 0.05 is due to higher ferrite content (higher magnetostriction i.e. more strain induced lattice distortions) and further decrease for y = 0.15 is due to decrease in piezoelectric phase (decrease in induced charge/electric field). Also lower value of ME output for y = 0.15 may be attributed to the leakage charges developed in the ferroelectric grains due to the presence of conductive ferrite grains [39]. The maximum value of ME coefficient, α for all composite samples is given in table 3.5. The values of ME coupling coefficients obtained for given NZF–PZT composite system are comparable to those reported for ferrite–ferroelectric bulk composites [40–42].

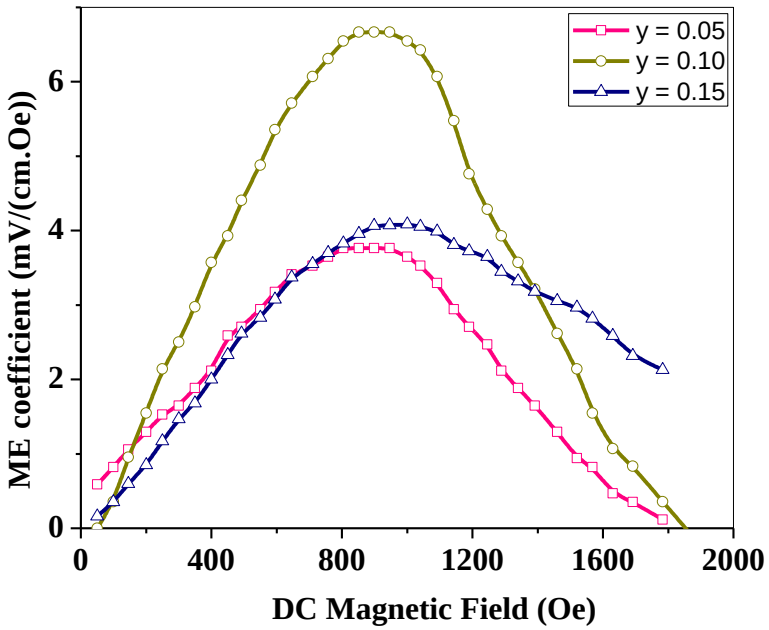

Figure 3.16 Variation of ME coupling coefficient, α (mV/(cm.Oe)) with DC magnetic field for y = 0.05, 0.10 and 0.15

Table 3.5 Piezoelectric, magnetic and magnetoelectric parameters for yNZF–(1–y)PZT (y = 0, 0.05, 0.10 and 0.15)

y	**H_c (Oe)**		**M_r (emu/g)**		**M_s (emu/g)**		**d_{33}**	**α**
	unpoled	**poled**	**unpoled**	**poled**	**unpoled**	**poled**	**(pC/N)**	**(mV/(cm.Oe))**
0	–	–	–	–	–	–	108	–
0.05	31	38	0.06	0.10	1.7	2.1	85	3.8
0.10	30	30	0.09	0.14	3.7	6.0	72	6.7
0.15	30	27	0.18	0.30	5.9	10.2	53	4.1

References

1. A.D. Sheikh and V.L. Mathe, J. Phys. Chem. Solids, **72** (2011) 1423.
2. Y. Xu, Ferroelectric Materials and their Applications, Elsevier Science Pub. Co., New York, USA (1991).
3. S.L. Swartz and T.R. Shrout, Mater. Res. Bull., **17** (1982) 1245.
4. K. Katayama, M. Abe, T. Akiba and H. Yanagida, J. Eur. Ceram. Soc., **5** (1989) 183.
5. J.V. Boomgaard and R.A.J. Born, J. Mater. Sci., **13** (1978) 1538.
6. W.E. Kramer, R.H. Hopkins and M.R. Daniel, J. Mater. Sci. Lett., **12** (1977) 409.
7. C. Prakash and O.P. Thakur, Mater. Lett., **57** (2003) 2310.
8. L.L. Hench and J.K. West, Principles of Electronics Ceramics, John Wiley and Sons, New York (1990).
9. I. Soibam, S. Phanjoubam, H.B. Sharma, H.N.K. Sarma, R. Laishram and C. Prakash, Solid State Commun., **148** (2008) 399.
10. K.K. Patankar, V.L. Mathe, A.N. Patil, Y.D. Kolekar and P.B. Joshi, J. Electroceram., **6** (2001) 115.
11. A.P. Barranco, J.D.S. Guerra, R.L. Noda and E.B. Araujo, J. Phys. D: Appl. Phys., **41** (2008) 215503.
12. S. Upadhyay, D. Kumar and O. Prakash, Bull. Mater. Sci., **19** (1996) 513.
13. S.L. Kadam, C.M. Kanamadi, K.K. Patankar and B.K. Chougule, Mater. Lett., **59** (2005) 215.
14. V.M. Latein, Sov. Tech. Phys. Lett., **18** (1997) 484.
15. K.K. Patankar, S.S. Joshi and B.K. Chougule, Phys. Lett. A, **346** (2005) 337.
16. D.C. Agrawal, Asian J. Phys., **6** (1997) 108.
17. K. Iwanchi, J. Appl. Phys., **10** (1971) 1520.
18. S.A. Mazena, S.F. Mansour, E. Dhahri, H.M. Zaki and T.A. Elmosalami, J. Alloys Compd., **470** (2009) 294.
19. R.S. Devan and B.K. Chougule, J. Appl. Phys., **101** (2007) 0141091.
20. X. Chao, Z. Yang, M. Dong and Y. Zhang, J. Magn. Magn. Mater., **323** (2011) 2012.
21. S.K. Pandey, O.P. Thakur, A. Kumar and C. Prakash, J. Appl. Phys., **100** (2006) 014104.

22. N. Ortega, P. Bhattacharya, R.S. Katiyar, P. Dutta, A. Manivannan, M.S. Seehra, I. Takeuchi and S.B. Majumder, J. Appl. Phys., **100** (2006) 126105.
23. H.C. He, J. Ma, J. Wang and C.W. Nan, J. Appl. Phys., **103** (2008) 034103.
24. W. Wersing, K. Lubitz and J. Mohaupt, IEEE Trans. on Ultrasonics, Ferroelectrics and Frequency Control, **36** (1989) 424.
25. D. Damjonvic, T.R. Gururaja and L.E. Cross, Am. Ceram. Soc. Bull., **66** (1987) 699.
26. M.J. Haun, E. Furman, S.J. Jang and L.E. Cross, IEEE Trans. On Ultrasonics, Ferroelectrics and Frequency Control, **36** (1989) 393.
27. R.A. Islam and S. Priya, Integr. Ferroelectr., **82** (2006) 1.
28. D. Wu, W. Gong, H. Deng and M. Li, J. Phys. D: Appl. Phys., **40** (2007) 5002.
29. J. Zhai, N. Cai, Z. Shi, Y. Lin and C.W. Nan, J. Phys. D: Appl. Phys., **37** (2004) 823.
30. S.Y. Tan, S.K. Shannigraphi, S.H. Tan and F.E.H. Tay, J. Appl. Phys., **103** (2008) 094105.
31. B.K. Bammannavar and L.R. Naik, J. Magn. Magn. Mater., **321** (2009) 382.
32. G. Srinivasan, D.J. Fekel, R. Hayes, V.M. Laletin, N. Puddbnaya and E.T. Rasmussen, Solid State Commun., **124** (2002) 373.
33. D.R. Patil, S.A. Lokare, R.S. Devan, S.S. Chougule, Y.D. Kolekar and B.K. Chougule, J. Phys. Chem. Solids, **68** (2007) 1522.
34. J.H. Park, M.G. Kim, S. Ryu and H.M. Jang, J. Magn. Magn. Mater., **321** (2009) 1971.
35. S.U. Durgadsimi, S.S. Chougule, B.K. Chougule, C.H. Bhosale and S.S. Bellad, Int. J. Eng. Sci. Tech., **3** (2011) 1446.
36. K. Tahmasebi, A. Barzegar, J. Ding, T.S. Herng, A. Huang and S. Shannigrahi, Mater. Design, **32** (2011) 2370.
37. J.G. Wan, X.W. Wang, Y.J. Wu, M. Zeng, Y. Wang and H. Jiang, Appl. Phys. Lett., **86** (2005) 122501.
38. G. Srinivasan, E.T. Rasmussen, J. Gallegos and R. Srinivasan, Phys. Rev. B, **64** (2001) 214408.
39. C.M. Kanamadi and B.K. Chougule, J. Electroceram., **15** (2005) 123.
40. R.P. Mahajan, K.K. Patankar, M.B. Kothale, S.C. Chaudhari, V.L. Mathe and S.A. Patil, Pramana–J. Phys., **58** (2002) 1115.
41. S. Mazuder and G.S. Bhattacharyya, Ceram. Int., **30** (2004) 389.
42. C.M. Kanamadi, L.B. Pujari and B.K. Chougule, J. Magn. Magn. Mater., **295** (2005) 139.

Chapter-IV

Characterization of NZF-PLZT Composites

Chapter–IV

Characterization of NZF–PLZT Composites

In this chapter, the studies on structural, microstructural, dielectric, ferroelectric, piezoelectric, ferromagnetic and magnetoelectric properties of composites of NiZn ferrite and La substituted lead zirconate titanate (NZF–PLZT) are discussed. Composites having general formula $yNi_{0.8}Zn_{0.2}Fe_2O_4–(1–y)Pb_{1–3x/2}La_xZr_{0.65}Ti_{0.35}O_3$ with x = 0.01, 0.02, 0.03 and y = 0, 0.05, 0.10, 0.15 (series 2) were synthesized by conventional solid state reaction route. La content (x) in ferroelectric phase was varied upto 0.03 as for higher La content in PZT, the disordering effect of La becomes important resulting in considerable decrease in the values of remanant polarization (P_r) and saturation polarization (P_s) [1, 2]. The presence of individual phases (NZF and PLZT) was confirmed by using X–ray diffraction (XRD) technique. The samples were sintered at optimized sintering temperature (1200 ^oC for 4 hrs). To study the effect of La substitution, the experimental results of NZF–PLZT samples were compared with those of NZF–PZT samples (discussed in chapter III). For this purpose, the following compositional series were prepared keeping ferrite content (y) constant:

Series 2A: yNZF–(1–y)PLZT with x = 0, 0.01, 0.02, 0.03 and y = 0

Series 2B: yNZF–(1–y)PLZT with x = 0, 0.01, 0.02, 0.03 and y = 0.05

Series 2C: yNZF–(1–y)PLZT with x = 0, 0.01, 0.02, 0.03 and y = 0.10

Series 2D: yNZF–(1–y)PLZT with x = 0, 0.01, 0.02, 0.03 and y = 0.15

X–ray diffraction analysis was carried out to confirm the coexistence of individual phases (NZF and PLZT) and to study the effect of La substitution on lattice constants corresponding to both phases and relative density values of composites. Scanning electron micrographs were taken for microstructural study of the samples. Dielectric properties were studied as a function of temperature and frequency. Decrease in ferroelectric Curie temperature (T_c) and increase in room temperature dielectric constant with increase in La substitution was observed for all series.

To study ferroelectric and magnetic ordering in composite samples, P–E and M–H hysteresis loops were recorded respectively. La substitution results in improved ferroelectric properties for all composite samples. Increase in piezoelectric charge coefficient (d_{33}) was observed with increasing La content for all series. M–H hysteresis loops were recorded for electrically poled and unpoled samples to confirm magnetoelectric coupling between the two phases (NZF and PLZT). Enhancement in magnetization for electrically poled samples was observed which shows that there is a good electromagnetic coupling between the two phases and this property can be exploited for sensor applications.

As discussed in chapter III, maximum value of ME coupling coefficient (6.7 mV/(cm.Oe)) was observed for $0.1Ni_{0.8}Zn_{0.2}Fe_2O_4–0.9PbZr_{0.65}Ti_{0.35}O_3$ composite (series 1), hence effect of La substitution (x) on magnetoelectric coupling was studied for samples with y = 0.10 (series 2C). All of the aforementioned bring us to the conclusion that La substituted magnetoelectric composites have improved dielectric, ferroelectric, piezoelectric and magnetoelectric properties as compared to unsubstituted one (x = 0) for all series.

4.1 Synthesis of Individual Phases

The ferrite phase, $Ni_{0.8}Zn_{0.2}Fe_2O_4$ (NZF) was synthesized by conventional solid state reaction route as per details given in section 3.1 (chapter III). For the synthesis of ferroelectric phase, $Pb_{1–3x/2}La_xZr_{0.65}Ti_{0.35}O_3$ (PLZT), AR grade PbO, ZrO_2, TiO_2 and La_2O_3 were used as raw materials and weighed in required molar proportions. An excess of 2% of PbO was added to compensate for lead loss during sintering. The mixing process was carried out by ball milling using distilled water (wetting media) and zirconia balls (grinding media). The dried powder was calcined at 800 ^oC for 4 hrs. After ball milling and drying, the powder mixture was re–calcined at 1000 ^oC for 4 hrs. XRD analysis was carried out for identification of both phases (ferrite and ferroelectric). XRD pattern for NZF phase is already given in figure 3.1(b) (chapter III) and for PLZT phase, $Pb_{1–3x/2}La_xZr_{0.65}Ti_{0.35}O_3$ (x = 0, 0.01, 0.02 and 0.03) are shown in figure 4.1. XRD patterns for PLZT show that all calcined samples are in pure perovskite phase. The phase formation was confirmed with standard JCPDS file no. 89–1279 of PZT.

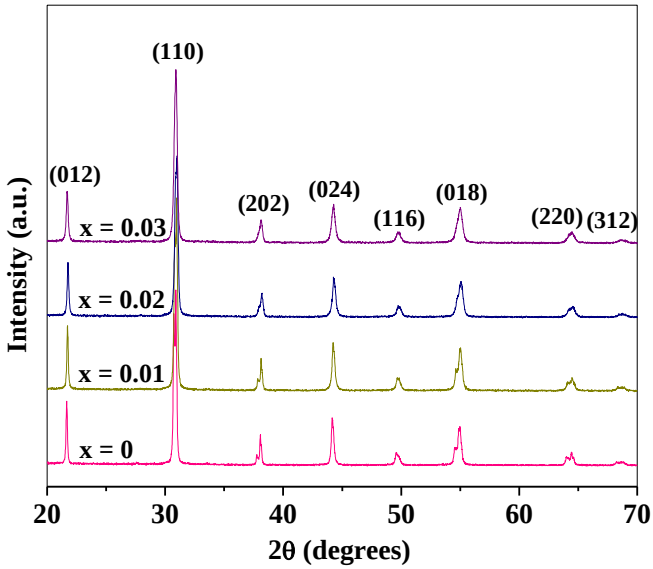

Figure 4.1 XRD patterns for PLZT calcined samples (x = 0, 0.01, 0.02 and 0.03)

4.2 Synthesis of $yNi_{0.8}Zn_{0.2}Fe_2O_4–(1–y)Pb_{1–3x/2}La_xZr_{0.65}Ti_{0.35}O_3$

NZF–PLZT composites according to the formula $yNi_{0.8}Zn_{0.2}Fe_2O_4–(1–y)Pb_{1–3x/2}La_xZr_{0.65}Ti_{0.35}O_3$ with x = 0.01, 0.02, 0.03 and y = 0, 0.05, 0.10, 0.15 were prepared by mixing the two phases in desired ratio. Powder mixture was ball milled in the same planetary ball mill using distilled water and zirconia balls. After drying, the powder was mixed with small amount of diluted polyvinyl alcohol (3% by weight) as binder. This dried mixture was uniaxially pressed into disc shaped pellets with diameter ~ 15 mm and thickness ~ 1 mm. The pellets were finally sintered in a programmable furnace at optimized temperature i.e. 1200 ^oC for 4 hrs.

4.3 Characterization of $yNi_{0.8}Zn_{0.2}Fe_2O_4–(1–y)Pb_{1–3x/2}La_xZr_{0.65}Ti_{0.35}O_3$

4.3.1 X–Ray Diffraction

X–ray diffraction patterns of the modified NZF–PLZT composite samples were recorded for phase identification and structural analysis. Figure 4.2 shows the XRD patterns for $Pb_{1–3x/2}La_xZr_{0.65}Ti_{0.35}O_3$ with x = 0, 0.01, 0.02 and 0.03 (series 2A). The patterns show well defined peaks and analysis suggests the formation of single phase compounds with rhombohedral perovskite structure. The values of lattice constant 'a' were calculated using Bragg's law by indexing the diffraction peaks using standard reference data (JCPDS card 89–1279 of PZT). There is a slight decrease in the values of lattice constant of ferroelectric phase which may be due to substitution of smaller ionic size of La at Pb site ($r(Pb^{+2})$ = 1.63 Å and $r(La^{+3})$ = 1.50 Å).

Figures 4.3–4.5 show the XRD patterns for all composite series with y = 0.05, 0.10 and 0.15 (series 2B, 2C and 2D). These XRD patterns show well defined peaks with specific indices characteristics of ferrite phase (NZF) and ferroelectric phase (PLZT). No additional/unidentified peaks were observed. Intensity and number of peaks corresponding to NZF are very small due to the lower concentration of ferrite phase (intensity of diffraction peaks corresponding to individual phases depend on their fraction in the composites). The values of lattice constant 'a' corresponding to both phases were calculated for all the samples and are given in table 4.1 for comparison. The results are in well agreement with the literature [3, 4]. Similar trend in the values of lattice constant corresponding to ferroelectric phase was observed as that for y = 0 (series 2A) with La substitution (x). This slight decrease in values of lattice constant corresponding to PLZT phase for higher La content can be explained on the same lines as in the case of pure ferroelectric series (series 2A). Random variation in lattice constant corresponding to ferrite phase were observed for all composite series. This may be due to stress induced by ferroelectric phase surrounding the ferrite phase [5].

The experimental density, X–ray density and relative density were determined for all samples of series 2A, 2B, 2C and 2D and are given in table 4.1. Comparison shows that in all the series, samples with x = 0.01 have lower relative density as compared to the samples with x = 0. For x = 0.02, there is increase in relative density whereas density decreases again for x = 0.03. Lower density for small concentration of substituents is already observed in many ferroelectric

ceramics [6, 7]. This variation in density can be explained by the number of Pb vacancies which affect volume diffusion during densification for different concentrations of substituents [8]. For unsubstituted samples (x = 0), the number of Pb vacancies are high enough to obtain sufficiently high volume diffusion resulting in higher densification. For samples with lower concentration of La content (x = 0.01), the number of Pb vacancies are partially compensated by La^{+3} ions leading to reduced volume diffusion and hence lower densification. Further, increase in La^{+3} concentration (x = 0.02) results in increase in densification which may be attributed to the decrease in unit cell volume by substituting less ionic size substituent.

4.3.2 Scanning Electron Microscope

Figures 4.6–4.9 show the SEM micrographs for all samples of series 2A, 2B, 2C and 2D respectively. It can be seen from the micrographs that grains of different sizes are densely distributed over the entire surface of the samples with well defined grain boundaries. The average grain size was calculated by line intercept method and is given in table 4.1. The average grain size of the samples is in the range 1.5–3.8 μm. With increase in substituent content (x), microstructural change is clearly observed in terms of different grain size. The average grain size for sample with x = 0.01 is larger as compared to that for sample with x = 0.03 for pure ferroelectric series (series 2A). The reason for large grain size for sample with x = 0.01 is the solubility of La in PZT lattice. For x = 0.02 and 0.03, grain size decreases which can be attributed to the segregation of La at grain boundaries resulting in inhibition of grain growth [9]. For samples of composite series (series 2B, 2C and 2D), individual phases could not be distinguished in SEM micrographs because of the small concentration of ferrite phase.

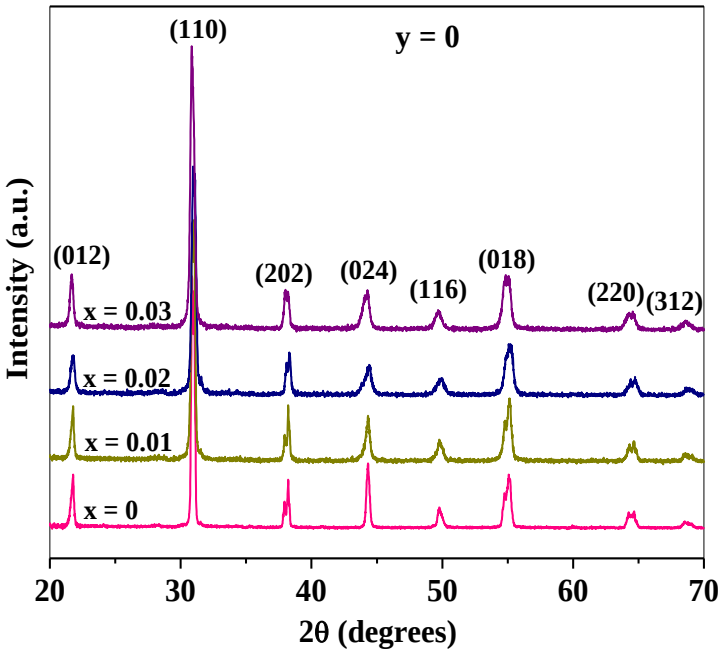

Figure 4.2 XRD patterns for all samples of series 2A

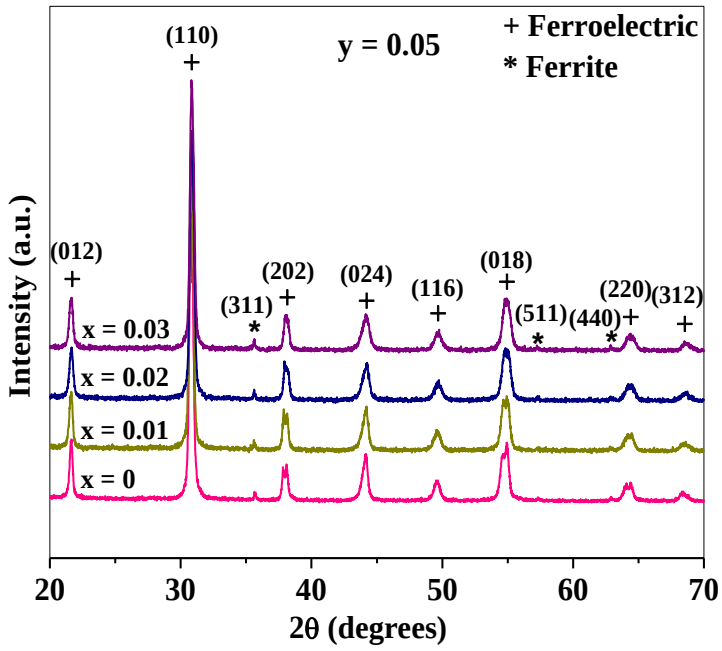

Figure 4.3 XRD patterns for all samples of series 2B

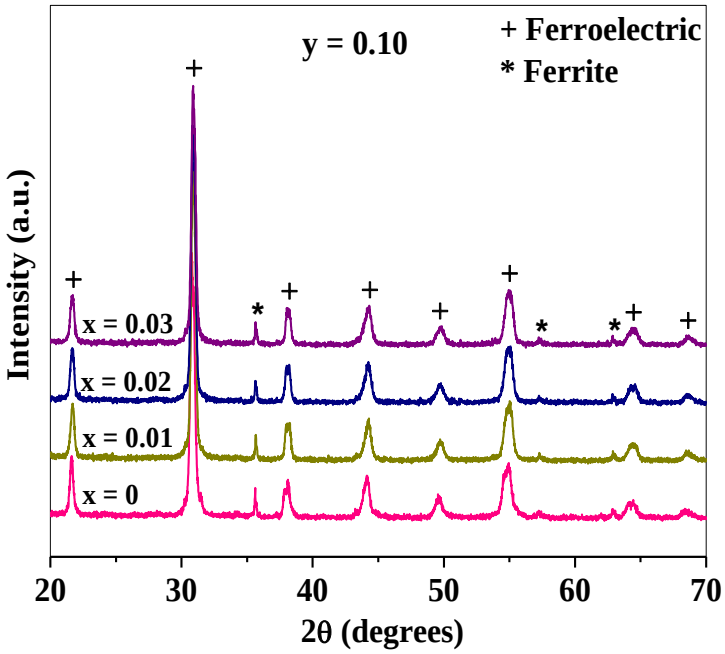

Figure 4.4 XRD patterns for all samples of series 2C

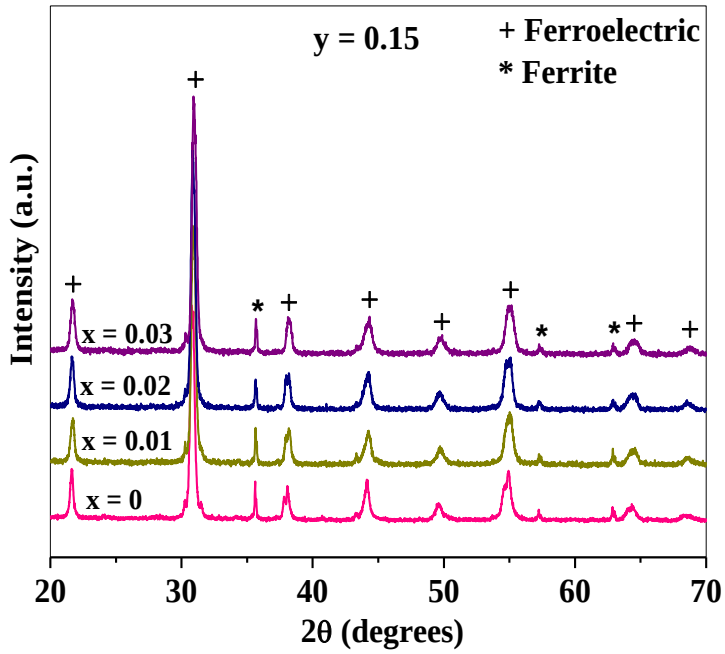

Figure 4.5 XRD patterns for all samples of series 2D

Table 4.1 Structural parameters for NZF–PLZT samples

x	Lattice Constant (Ferroelectric phase) (Å)	Lattice constant (Ferrite phase) (Å)	Exp. Density (g/cc)	X–ray Density (g/cc)	Relative Density (%)	Average grain size (µm)
Series 2A **(y = 0)**						
0	4.093	–	7.58	8.02	94.5	2.3
0.01	4.092	–	7.28	7.98	91.3	3.8
0.02	4.083	–	7.40	7.99	92.6	3.4
0.03	4.080	–	7.32	7.97	91.8	3.0
Series 2B **(y = 0.05)**						
0	4.106	8.346	7.31	7.89	92.7	2.5
0.01	4.103	8.358	7.18	7.85	91.5	2.3
0.02	4.100	8.353	7.26	7.86	92.4	1.6
0.03	4.099	8.353	7.14	7.84	91.1	1.5
Series 2C **(y = 0.10)**						
0	4.104	8.353	6.88	7.75	88.8	2.4
0.01	4.097	8.342	6.79	7.72	88.0	2.3
0.02	4.095	8.346	6.87	7.73	88.9	2.1
0.03	4.092	8.348	6.81	7.71	88.3	1.5
Series 2D **(y = 0.15)**						
0	4.108	8.353	6.78	7.62	89.0	3.2
0.01	4.097	8.348	6.41	7.59	84.5	2.5
0.02	4.095	8.346	6.78	7.60	89.2	1.8
0.03	4.087	8.342	6.75	7.58	89.1	1.5

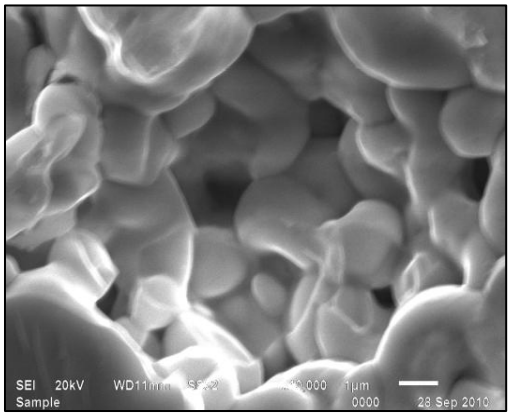

x = 0

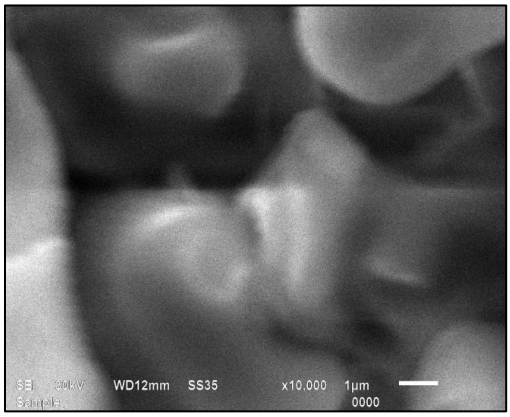

x = 0.01

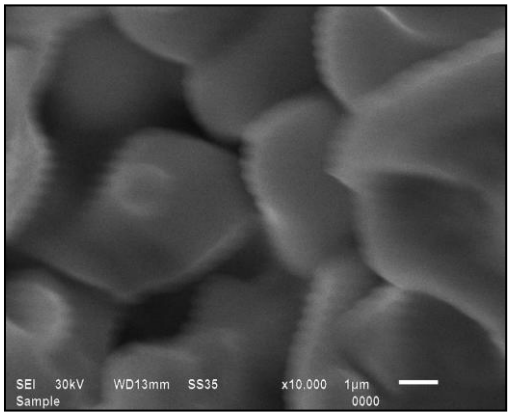

x = 0.02

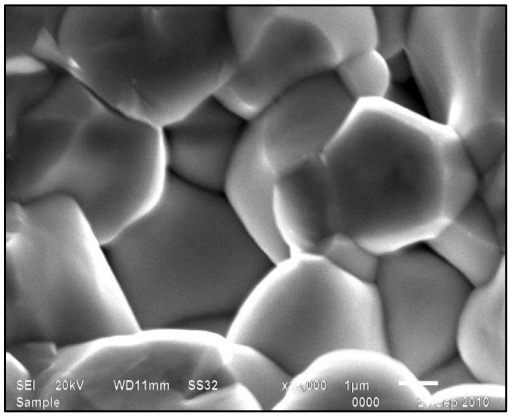

x = 0.03

Figure 4.6 SEM micrographs for all samples of series 2A

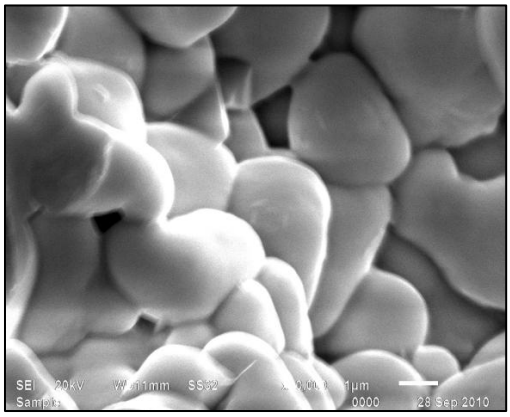

x = 0

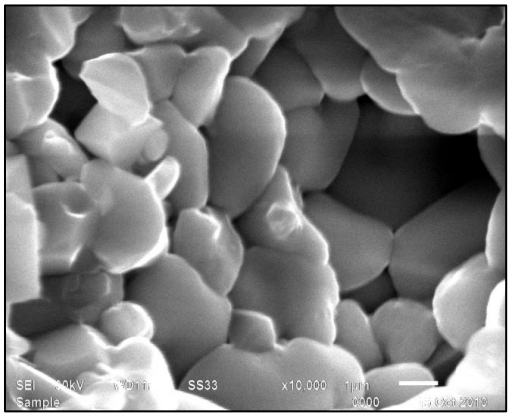

x = 0.01

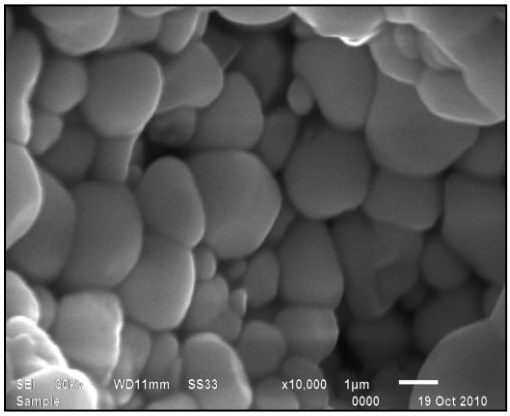

x = 0.02

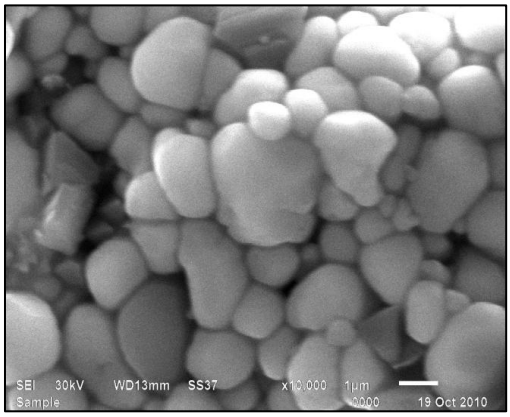

x = 0.03

Figure 4.7 SEM micrographs for all samples of series 2B

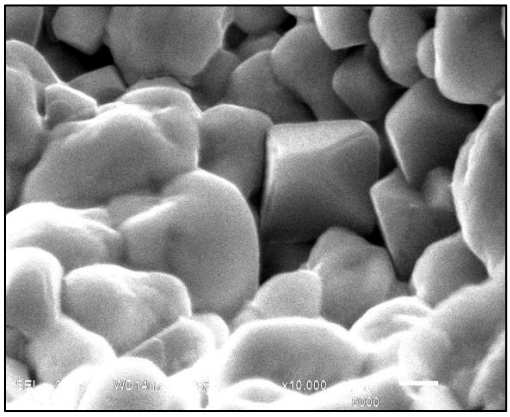

x = 0

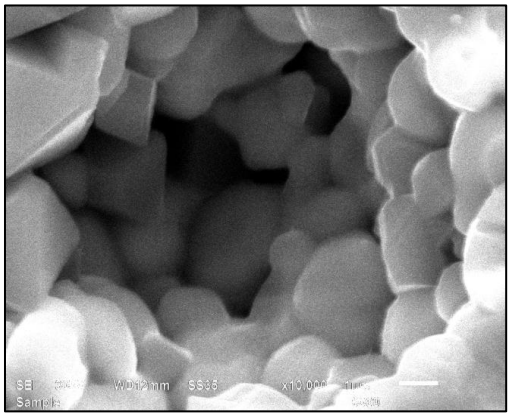

x = 0.01

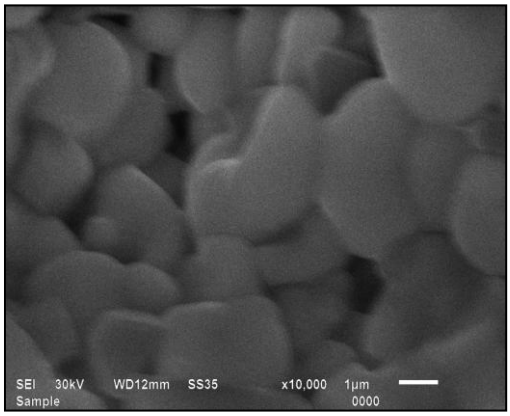

x = 0.02

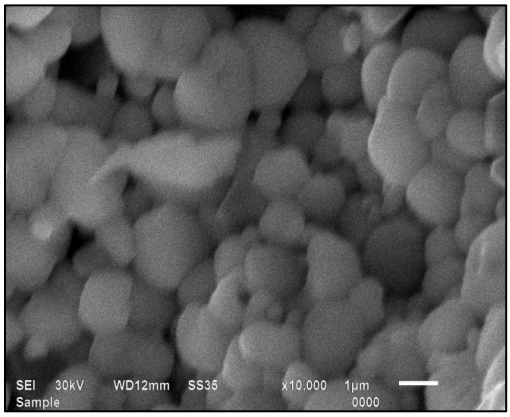

x = 0.03

Figure 4.8 SEM micrographs for all samples of series 2C

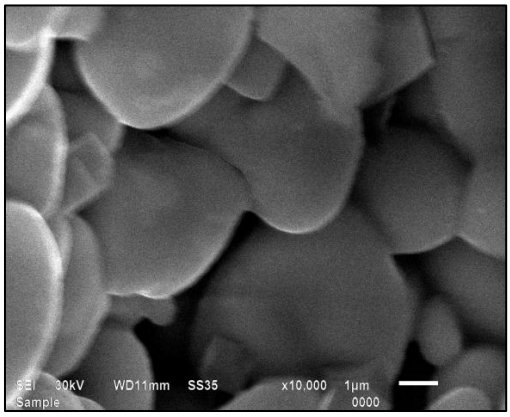

x = 0

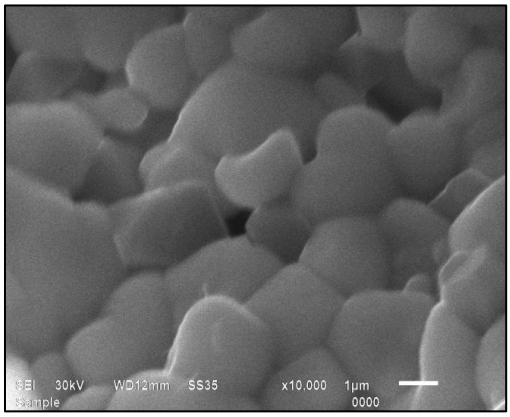

x = 0.01

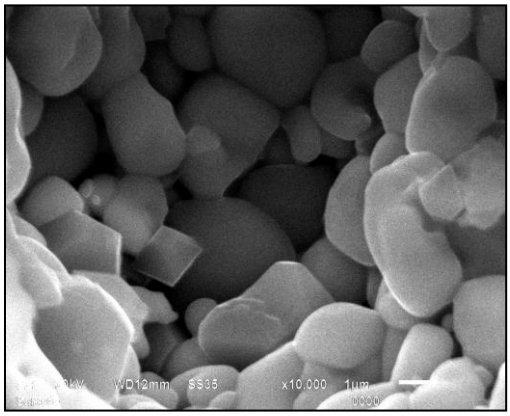

x = 0.02

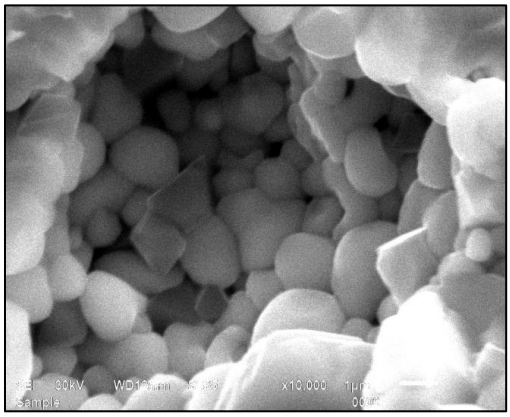

x = 0.03

Figure 4.9 SEM micrographs for all samples of series 2D

4.3.3 Dielectric Properties

The variation of dielectric constant (ε') and loss (tanδ) with temperature for the samples of series 2A, 2B, 2C and 2D is shown in figures 4.10–4.13 respectively with x = 0.01, 0.02 and 0.03. Temperature dependence was studied at discrete frequencies viz. 1, 10 and 100 kHz in the temperature range of 35–500 ^{o}C for all samples. Values of ferroelectric Curie temperature (T_c), room temperature dielectric constant (ε'_{RT}), dielectric constant at T_c (ε'_{max}), room temperature dielectric loss ($\tan\delta_{RT}$) and dielectric loss at T_c ($\tan\delta_{max}$) were determined for all samples and are given in table 4.2 for comparison. For normal ferroelectrics, dielectric constant initially increases with increase in temperature (interfacial polarization is more dominant as compared to the dipolar polarization) and reaches to a maximum value at particular temperature followed by decrease with further increase in temperature due to the transition from ferroelectric phase to paraelectric phase [10–13]. For the samples of series 2A (pure ferroelectric series), similar behavior is observed. The temperature at which ε' is maximum, corresponds to ferroelectric Curie temperature (T_c). Similar temperature dependence was observed for dielectric loss for samples of series 2A. Decrease in dielectric loss above T_c is mainly due to the reduction in the domain wall contribution to the loss. Dielectric loss values are smaller for denser samples which are in agreement with the SEM micrographs (figure 4.6).

Due to varying amount of La substitution (x), the crystal structure of different compositions do not maintain the same lattice parameters resulting in different Curie temperature [2]. The value of T_c is found to decrease whereas room temperature dielectric constant increases with increase in La substitution (x). This decrease in T_c is mainly due to shrinkage in the PZT lattice volume and substitution of smaller ionic size La^{+3} ions at Pb site [14]. Sample with x = 0.01 shows decrease in room temperature dielectric constant as compared to the unsubstituted one (x = 0). For x = 0.02 and 0.03, increase in room temperature dielectric constant is observed. These results are in consistence with the density measurements (table 4.1). Increase in dielectric constant for donor substituents in PZT is also well reported in literature [15].

Temperature dependence of dielectric constant for samples of composite series (series 2B, 2C and 2D) also show dielectric maxima corresponding to ferroelectric–paraelectric transition in ferroelectric phase (PLZT). But broadening in dielectric maxima and dielectric dispersion over a wide range of temperature around T_c is observed for all composite samples

which may be attributed to the microstructural inhomogeneity created in the samples due to the presence of ferrite phase (non–ferroelectric phase) [16, 17]. Increase in dielectric constant with increase in temperature was seen in the paraelectric region at 1 kHz for all composite samples. This increase may be due to thermally activated electron hopping in NZF phase resulting in increase in dielectric polarization proportional to temperature [18]. Higher values of dielectric loss are also observed at elevated temperatures due to thermal conductivity losses which occur as a result of electron hopping between Fe^{+2}/Fe^{+3} and Ni^{+2}/Ni^{+3} ions present due to NZF phase. Results given in table 4.2 show that La substitution not only results in improved dielectric properties of pure ferroelectric series (series 2A) but also for composite series (series 2B, 2C and 2D).

The room temperature variation of dielectric constant (ε') and loss (tanδ) of all NZF–PLZT samples as a function of frequency (10^2–10^6 Hz) is also studied and depicted in figures 4.14–4.17. For all samples, it is observed that dielectric constant decreases with increase in frequency for all series. Higher values of dielectric constant at lower frequencies are due to simultaneous presence of all types of polarizations (interfacial, dipolar, ionic and electronic). As frequency is increased, contribution from interfacial and dipolar polarization decreases resulting in decrease in the dielectric constant [19]. At higher frequencies, the main contribution to dielectric constant comes from ionic and electronic polarization. Similar type of frequency dependent dielectric behavior is found in many ferroelectric ceramics and ferrite–ferroelectric composites [20–23].

On comparing the frequency dispersion for unsubstituted samples (x = 0) with that for substituted ones (x = 0.01, 0.02 and 0.03), we observe that dispersion is more in case of unsubstituted ones for all series. This behavior can be explained on the basis of electronic charge carriers generated due to Pb^{+2} vacancies [24]. Further with increase in La substitution, this low–frequency dispersion is decreasing which may be due to decrease in concentration of Pb^{+2} vacancies (La^{+3} ions substitute Pb^{+2} ions) and donor effect of La substitution that counteracts the p–type conduction [3]. Similar behavior is observed for the frequency dependence of dielectric loss. Increase in dielectric loss at higher frequencies is observed for samples of series 2A and 2B which may be attributed to some extrinsic losses [25, 26].

Table 4.2 Dielectric parameters for NZF–PLZT samples at 100 kHz

x	T_c (^oC)	ε'_{RT}	ε'_{max}	$\tan\delta_{RT}$	$\tan\delta_{max}$
Series 2A **(y = 0)**					
0	422	820	19585	0.02	0.10
0.01	398	570	42645	0.07	0.17
0.02	365	1030	41260	0.04	0.13
0.03	342	1270	32890	0.04	0.06
Series 2B **(y = 0.05)**					
0	394	625	10760	0.03	0.15
0.01	390	800	10945	0.06	0.19
0.02	369	845	9710	0.07	0.12
0.03	362	925	8560	0.02	0.14
Series 2C **(y = 0.10)**					
0	408	590	7635	0.03	0.22
0.01	400	520	7035	0.02	0.19
0.02	377	610	8135	0.05	0.21
0.03	375	670	6945	0.06	0.16
Series 2D **(y = 0.15)**					
0	407	405	5275	0.12	0.31
0.01	406	420	4230	0.02	0.31
0.02	395	575	6315	0.01	0.25
0.03	354	595	6175	0.04	0.29

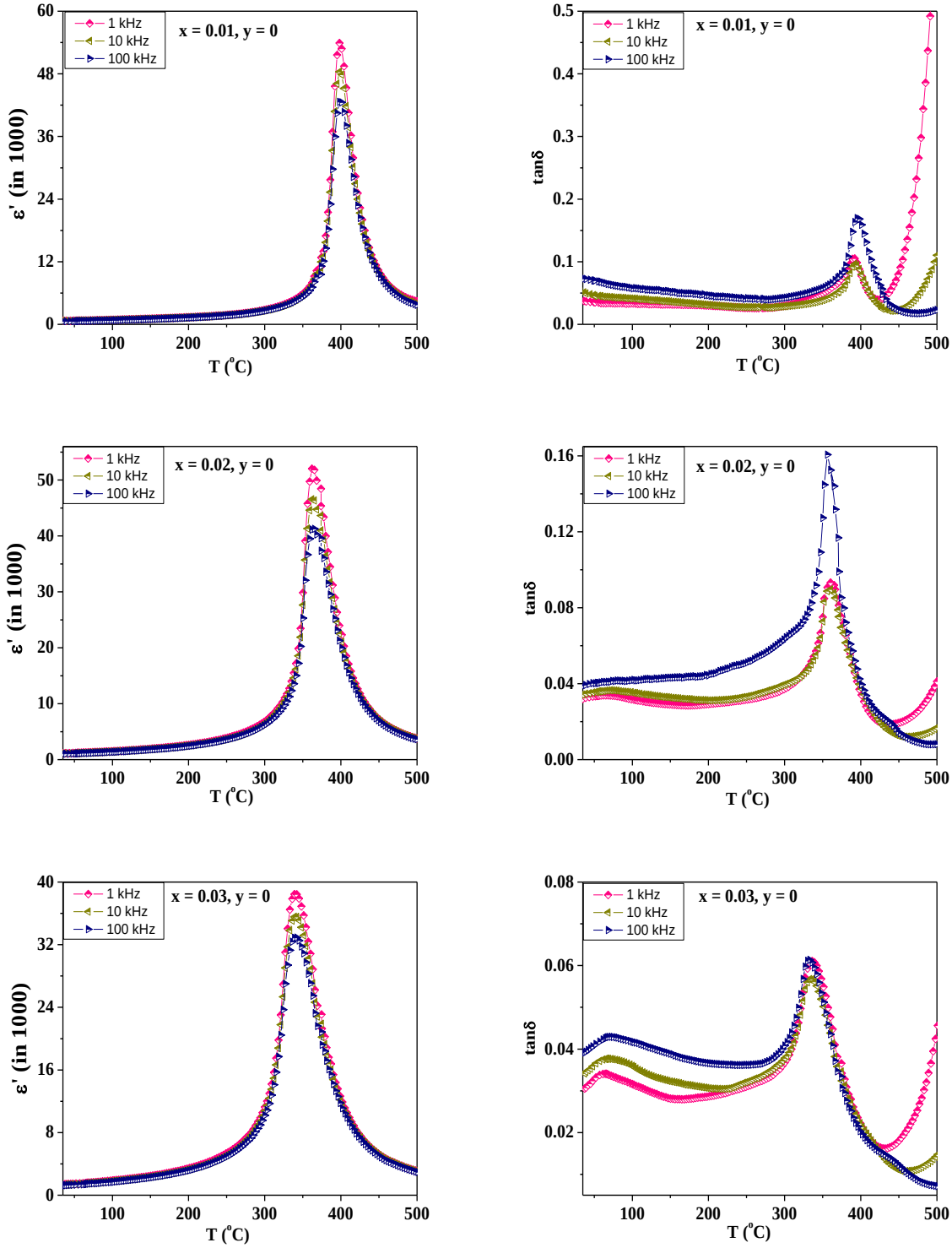

Figure 4.10 Variation of dielectric constant (ε') and loss (tanδ) with temperature for the samples of series 2A (x = 0.01, 0.02 and 0.03) at 1, 10 and 100 kHz

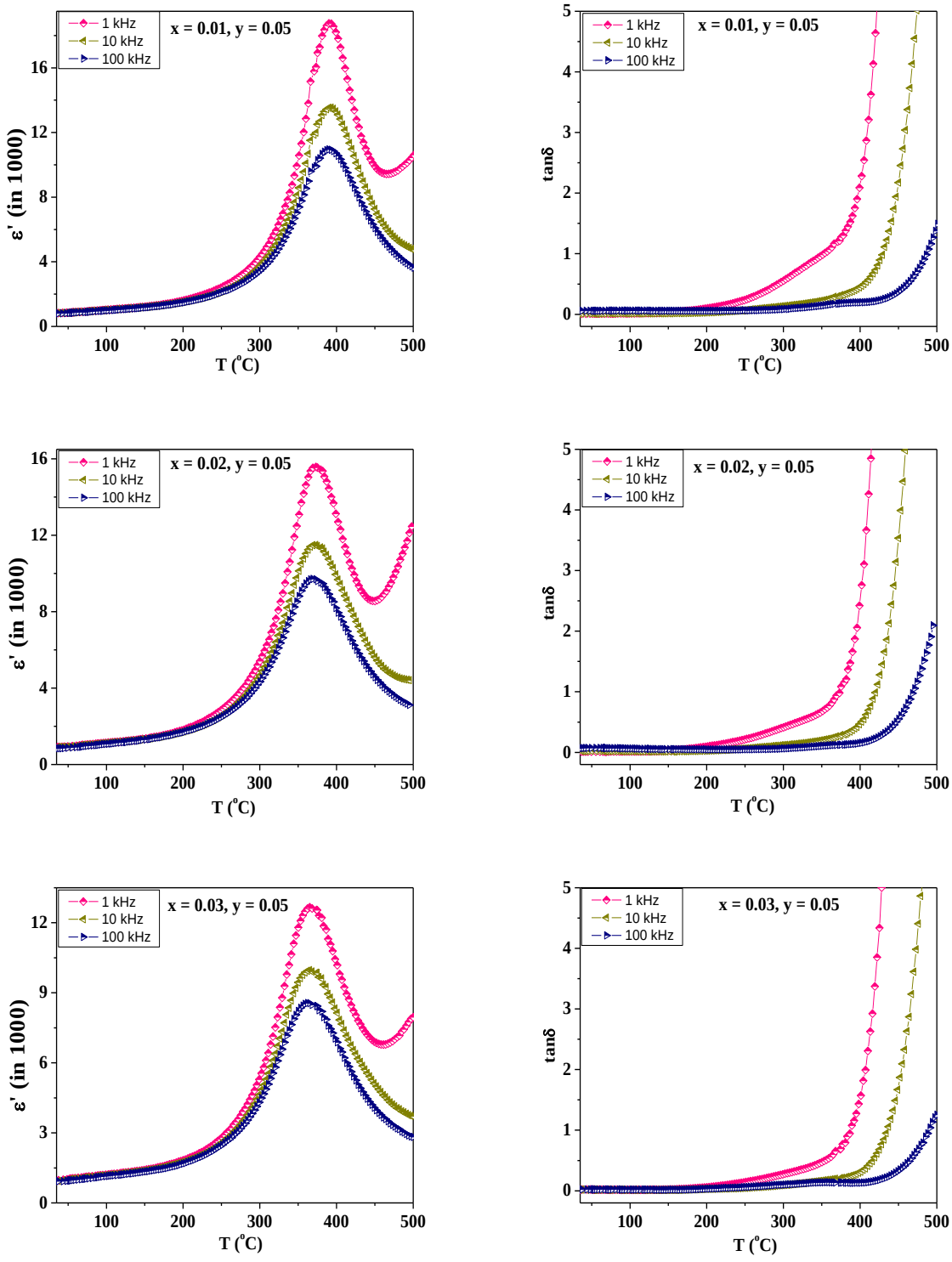

Figure 4.11 Variation of dielectric constant (ε') and loss (tanδ) with temperature for the samples of series 2B (x = 0.01, 0.02 and 0.03) at 1, 10 and 100 kHz

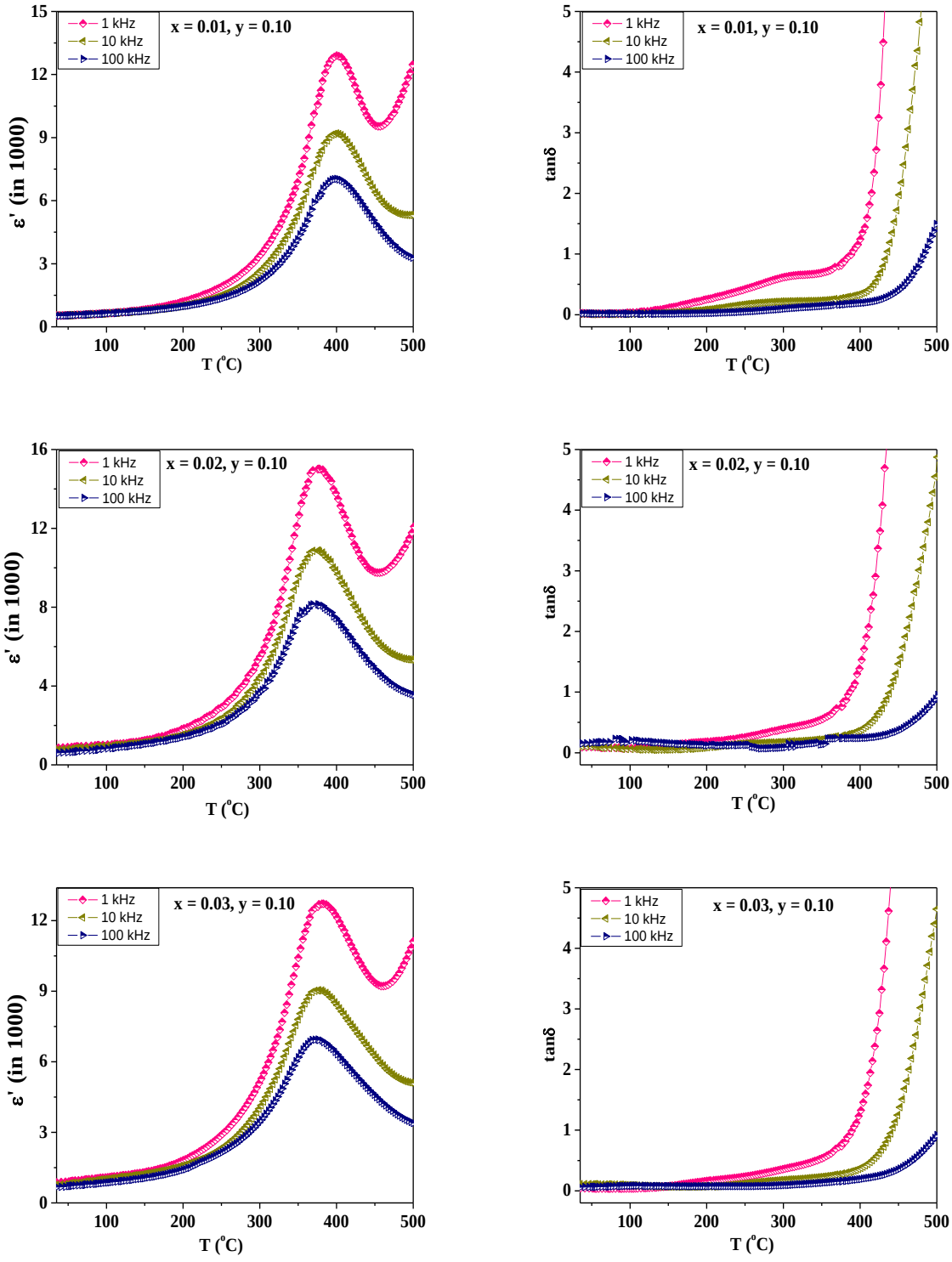

Figure 4.12 Variation of dielectric constant (ε') and loss (tanδ) with temperature for the samples of series 2C (x = 0.01, 0.02 and 0.03) at 1, 10 and 100 kHz

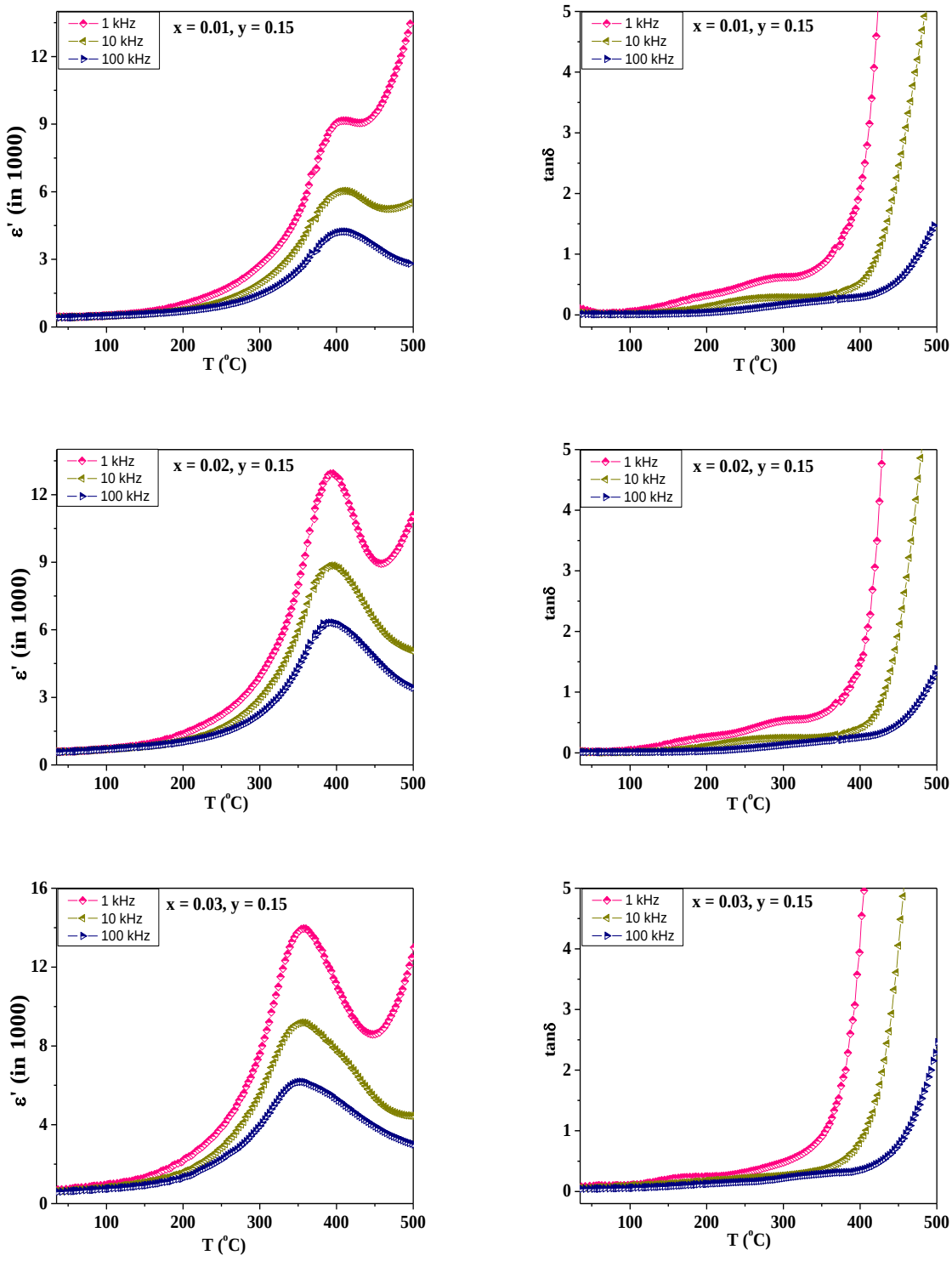

Figure 4.13 Variation of dielectric constant (ε') and loss (tanδ) with temperature for the samples of series 2D (x = 0.01, 0.02 and 0.03) at 1, 10 and 100 kHz

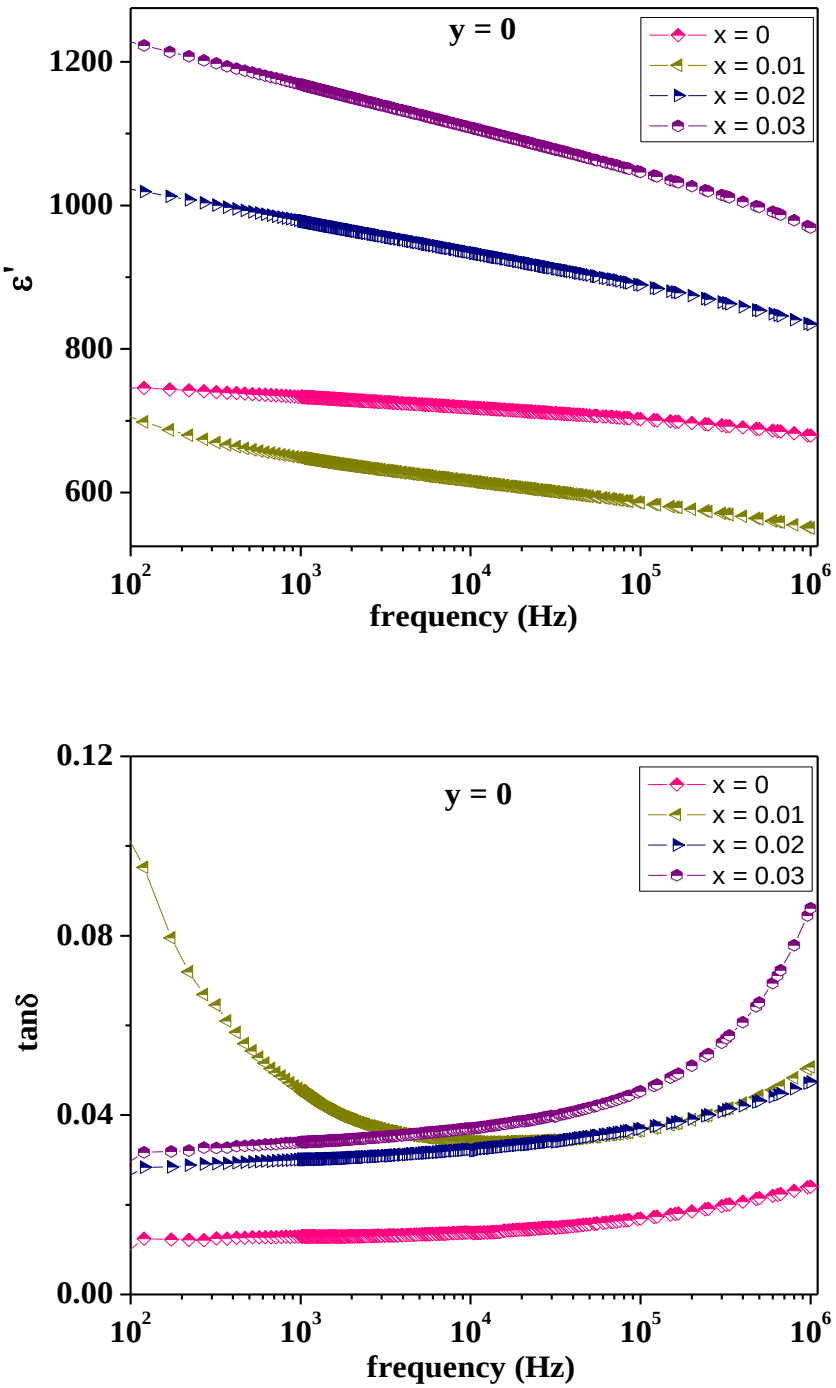

Figure 4.14 Variation of dielectric constant (ε') and loss (tanδ) with frequency for all samples of series 2A at room temperature

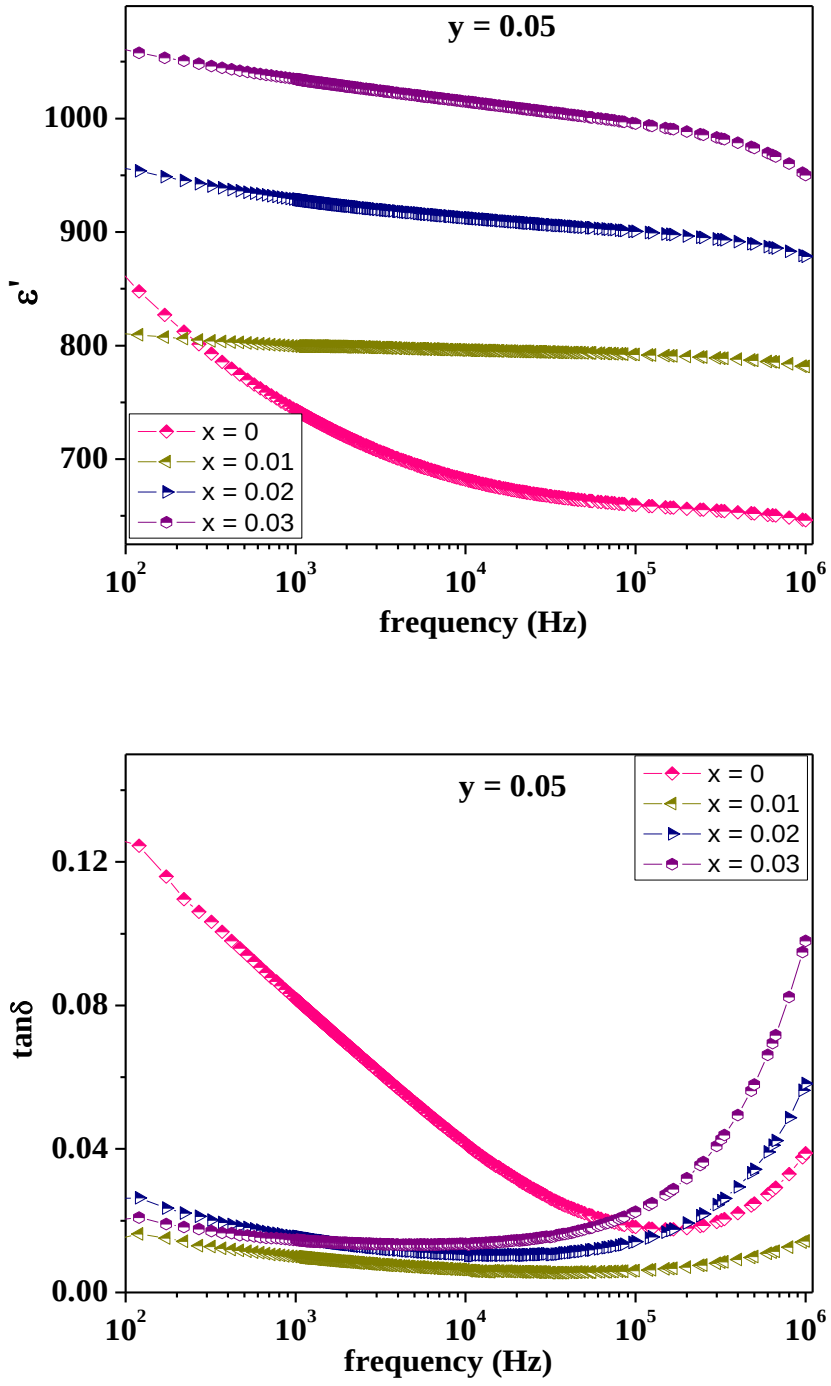

Figure 4.15 Variation of dielectric constant (ε') and loss (tanδ) with frequency for all samples of series 2B at room temperature

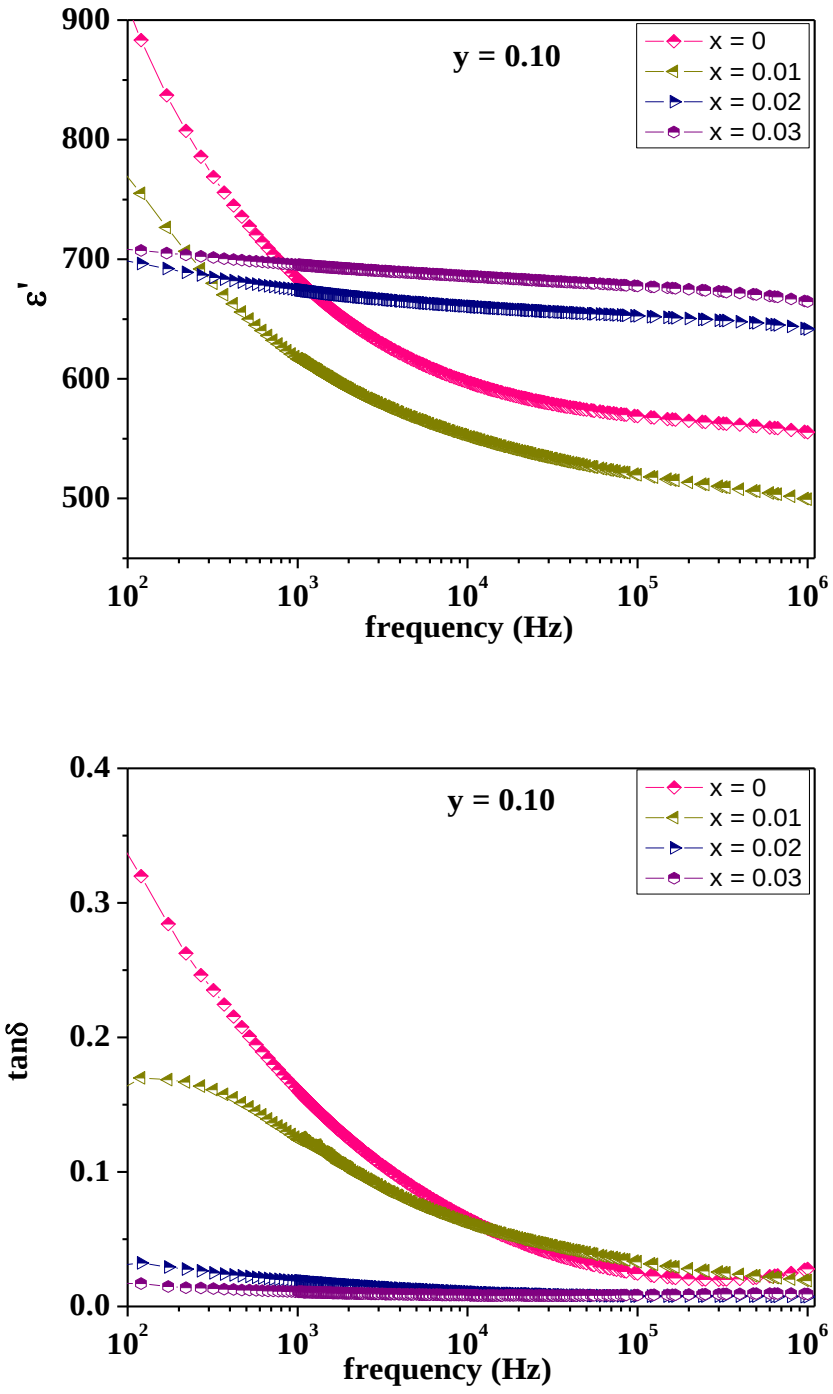

Figure 4.16 Variation of dielectric constant (ε') and loss (tanδ) with frequency for all samples of series 2C at room temperature

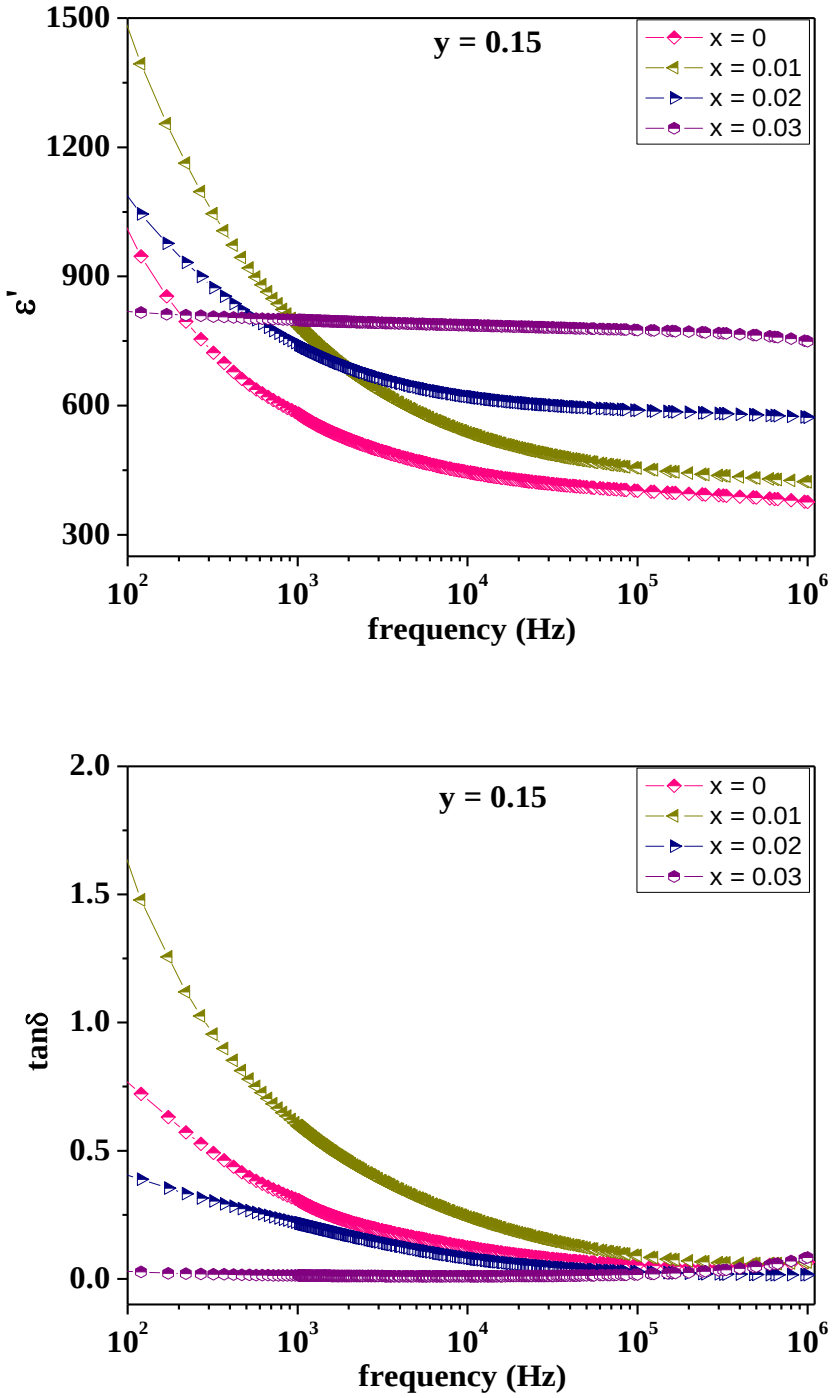

Figure 4.17 Variation of dielectric constant (ε') and loss (tanδ) with frequency for all samples of series 2D at room temperature

4.3.4 Ferroelectric Properties

To study ferroelectric ordering in NZF–PLZT system, room temperature P–E hysteresis loops were recorded for all samples at 20 Hz frequency and are shown in figures 4.18–4.21. The values of remanant polarization (P_r) and coercive field (E_c) were determined from the P–E loops and are given in table 4.3. In series 2A, well defined ferroelectric behavior is observed for all samples. Electric field ~ 15 kV/cm was sufficient to obtain saturation polarization (P_s). A comparison of P–E loops (figure 4.18) shows that as the substitution of La (x) increases, there is increase in remanant polarization (P_r) and saturation polarization (P_s). As x increases from 0 to 0.03, P_r and P_s are found to increase from ~ 8 μC/cm^2 to 32 μC/cm^2 and from ~ 17 μC/cm^2 to 39 μC/cm^2 respectively. It is due to the softening effect of donor substituent (La^{+3} at Pb^{+2} site) which results in higher multi–domain polarizations as is evident from increase in P_r and P_s. These results are in consistence with the literature [27–32]. It is also well reported in literature that donor substituents result in decrease in coercive field (E_c) but increase in squareness [33]. Though in present case, E_c is increasing with increase in La substitution (x), but increase in E_c (from ~ 5 kV/cm to 7 kV/cm) is much smaller as compared to increase in P_r (from ~ 8 μC/cm^2 to 32 μC/cm^2). Squareness of the P–E loops is found to increase with increase in amount of La substitution which is an important feature for the material selection for memory devices.

In series 2B and 2C, unsaturated and asymmetric (P_r and E_c values observed in positive and negative quadrants are not same) P–E hysteresis loops (figure 4.19 and 4.20) are observed for all samples. P–E hysteresis loops obtained for all samples of series 2B and 2C are due to the presence of NZF as non–ferroelectric phase and PLZT as ferroelectric phase, hence no saturation is observed. Similar loops are already reported by many research groups [34–36]. Further, more asymmetric behavior is seen for all samples of series 2C as compared to that of series 2B i.e. asymmetry increases with increase in ferrite content (discussed in section 3.3.4, chapter III). The values of P_r and E_c determined from P–E loops are listed in table 4.3. La substitution results in increase in P_r as well as E_c for samples of both series. There is not much effect on the values of P_r and E_c for composite samples (series 2B and 2C) as in case of pure ferroelectric samples (series 2A).

In series 2D, all composite samples show lossy loop i.e. more wide as compared to that for samples of series 2B and 2C and broader at tip. It may be due to the presence of high ferrite

content having high conductivity as compared to that for ferroelectric phase and resulting in high leakage current. Lossy loop for the sample with x = 0.01 and y = 0.15 is shown in figure 4.21.

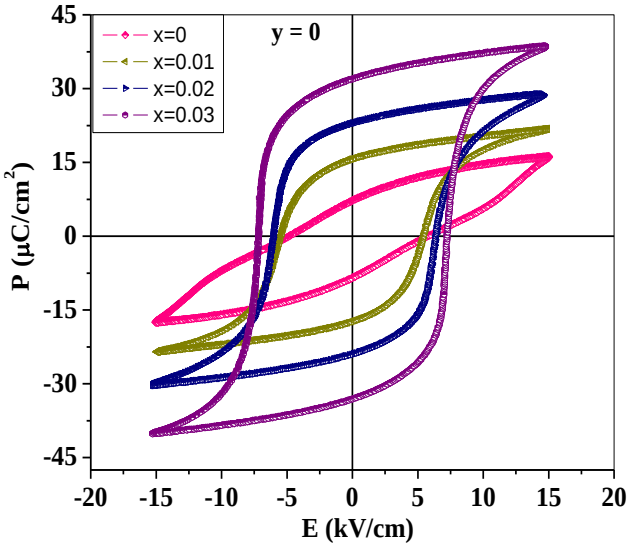

Figure 4.18 Room temperature P–E hysteresis loop for all samples of series 2A (x = 0, 0.01, 0.02 and 0.03) at 20 Hz

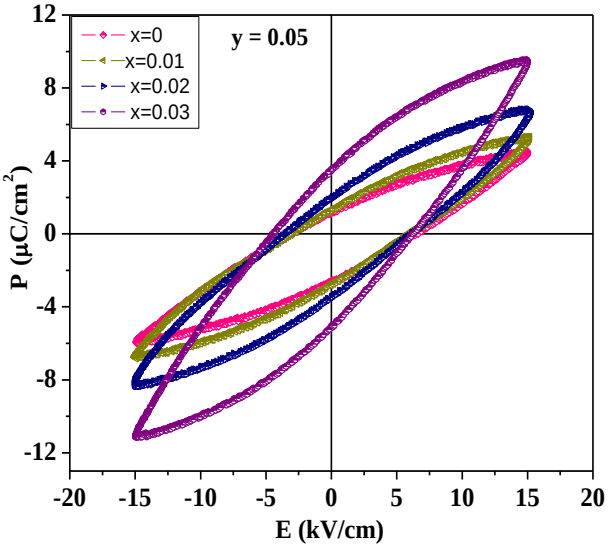

Figure 4.19 Room temperature P–E hysteresis loop for all samples of series 2B (x = 0, 0.01, 0.02 and 0.03) at 20 Hz

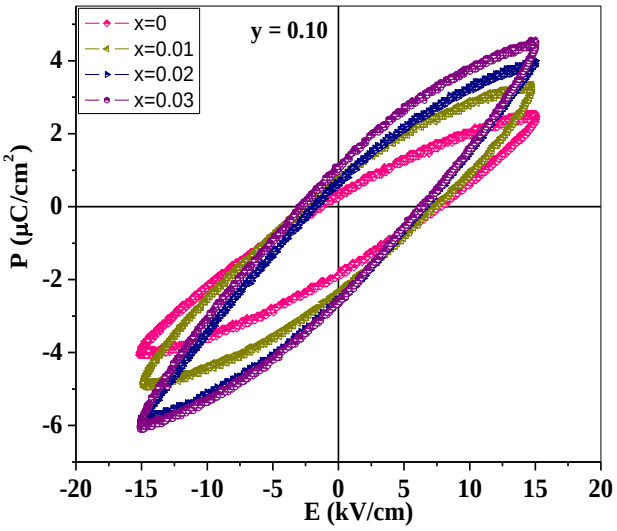

Figure 4.20 Room temperature P–E hysteresis loop for all samples of series 2C (x = 0, 0.01, 0.02 and 0.03) at 20 Hz

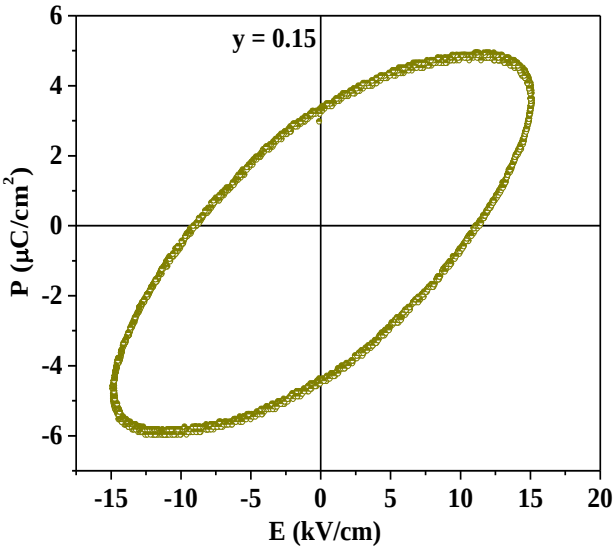

Figure 4.21 Room temperature P–E hysteresis loop for samples of series 2D (x = 0.01) at 20 Hz

4.3.5 Piezoelectric Properties

The values of piezoelectric charge coefficient, d_{33}, measured for all NZF–PLZT samples (series 2A, 2B, 2C and 2D) are given in table 4.3 for comparison. Prior to piezoelectric measurement, all samples were poled under a DC field of 15 kV/cm for 1 hr in a silicon oil bath at 150 ^{o}C. The d_{33} values are found to be compositional dependent because the composition influences the dielectric permittivity, electrostrictive constant and spontaneous polarization [37]. These parameters play an important role in determining the piezo–coefficients and are directly related to d_{33} coefficients [38]. In series 2A, the gradual increase in d_{33} values from ~ 108 pC/N to 139 pC/N is observed with increase in La substitution (x = 0 to 0.03). The highest value of d_{33} ~ 139 pC/N for x = 0.03 is due to high spontaneous polarization of ~ 39 μC/cm^2. This suggests that domain wall contribution is increasing with increase in La substitution [2]. The d_{33} values observed for all samples of series 2B, 2C and 2D are in the range of 85–120 pC/N, 72–89 pC/N and 53–68 pC/N respectively.

4.3.6 Ferromagnetic Properties

The magnetic properties of the composites are studied from their M–H hysteresis behavior. The typical room temperature M–H hysteresis loops for all samples of composite series (series 2B, 2C and 2D) are shown in figures 4.22–4.24 respectively. All the samples show well defined ferromagnetic behavior which confirms the existence of magnetic ordering in mixed ferrite–ferroelectric composite system. Magnetic field of strength ~ 2 kOe was sufficient to obtain saturation in M–H loops for all samples. The estimated values of remanant magnetization (M_r), saturation magnetization (M_s) and coercive field (H_c) for all samples are given in table 4.3. Values of M_r, M_s and H_c observed for samples of series 2A, 2B and 2C are in the range of ~ 0–0.2 emu/g, 0.8–6.9 emu/g and 30–40 Oe respectively. As expected, the magnetic parameters are dependent on the concentration of NZF phase in NZF–PLZT composites. Remanant magnetization (M_r) and saturation magnetization (M_s) increase with increase in NZF content (y) i.e. these values obey the rule of mixtures and go on increasing with increase in ferrite content. Small coercivity, H_c (~ 30–40 Oe) obtained for all composite samples indicate their soft magnetic behavior. These results are in fair agreement with the literature [39–41].

Further, with La substitution (x), random values of magnetic parameters (M_r, M_s and H_c) are observed for all samples of composite series (series 2B, 2C and 2D). This behavior can be understood in terms of the fact that M–H hysteresis loops in composites (NZF–PLZT) are obtained mainly due to the presence of NZF as magnetic phase while La is substituted in ferroelectric phase, PLZT (non–magnetic phase). Similar random variation in values of lattice constant corresponding to ferrite phase is observed with La substitution in ferroelectric phase (section 4.3.1).

4.3.7 Magnetoelectric Properties

To study magnetoelectric behavior, two pieces from a single pellet were taken. One piece was electrically poled at 15 kV/cm. M–H hysteresis loops were recorded for both poled and unpoled samples and the data was compared. M–H hysteresis loops at room temperature for both (poled and unpoled) samples are shown in figure 4.25 for composites with x = 0.02 and y = 0.05, 0.10, 0.15. For all studied samples, there is an enhancement in magnetization for poled samples, which confirms the magnetoelectric coupling between NZF and PLZT phases in these composite samples [42]. It is also observed from plots (figure 4.25) that the enhancement in magnetization (magnetoelectric coupling) increases with increase in y i.e. ferrite content, which is expected. For the sample with 15% ferrite (y = 0.15), an enhancement of approximately 100% is observed. This property shows that there is a good magnetoelectric coupling between the two phases.

Further, effect of La substitution on ME coupling coefficient (measure of changes in the induced electric field in magnetoelectric composites due to applied DC magnetic field) is also studied. As discussed in chapter III, maximum ME coupling coefficient of 6.7 mV/(cm.Oe) is observed for $0.1Ni_{0.8}Zn_{0.2}Fe_2O_4$–$0.9PbZr_{0.65}Ti_{0.35}O_3$ composite (y = 0.10, series 1), hence in this chapter, effect of La substitution (x) was studied for samples with y = 0.10 i.e. for series 2C. The variation of ME coupling coefficient (α) as a function of DC magnetic field in the presence of AC magnetic field of 10 Oe at 1 kHz for samples of series 2C is shown in figure 4.26. Initially α increases with increase in magnetic field, reaches to a maximum and then starts decreasing for higher values of magnetic field for all samples. This initial rise in α is attributed to the increase in magnetostriction induced strain in NZF phase and decrease in α for higher magnetic field values

is due to saturation in magnetostriction values of NZF phase. The maximum value of α is observed in the range of ~ 750–900 Oe for all samples.

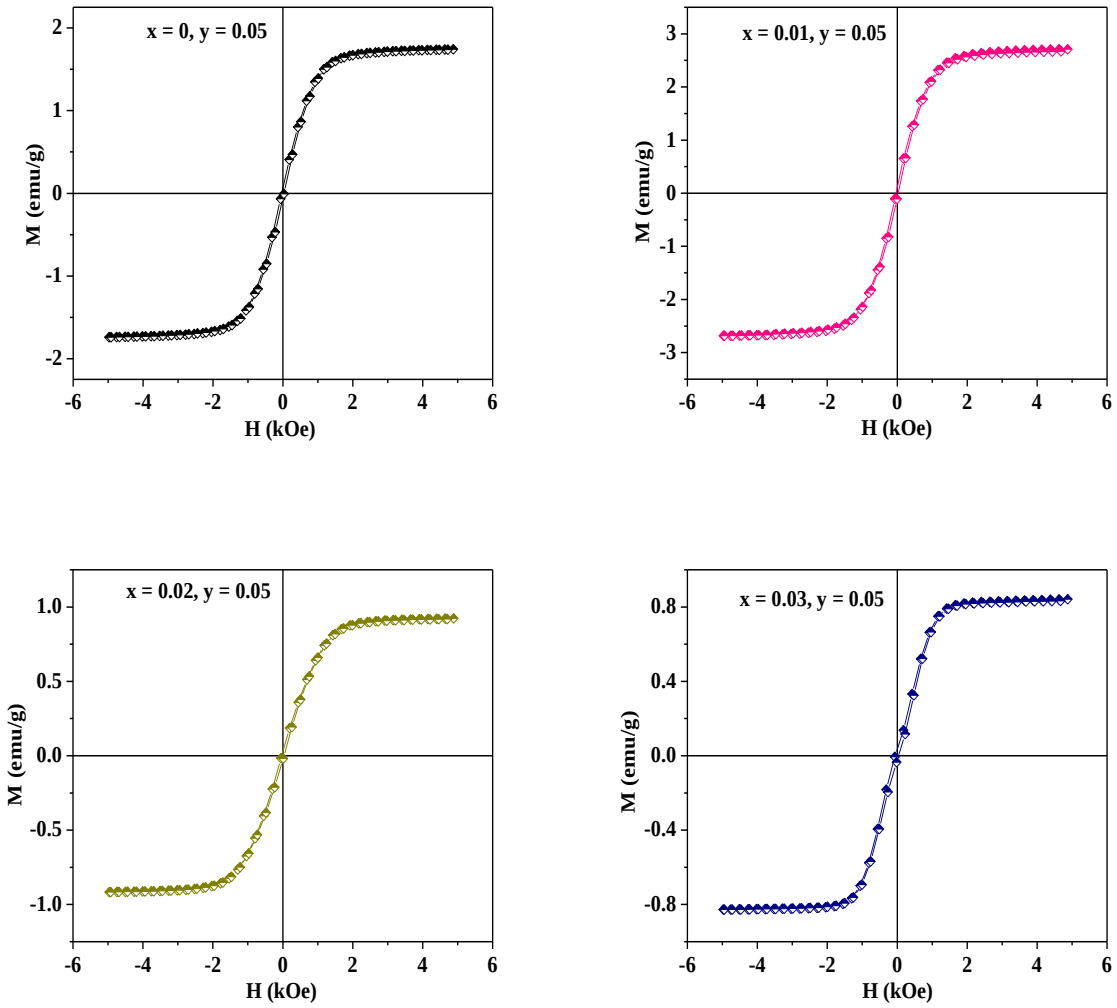

Figure 4.22 M–H hysteresis loop for all samples of series 2B at room temperature

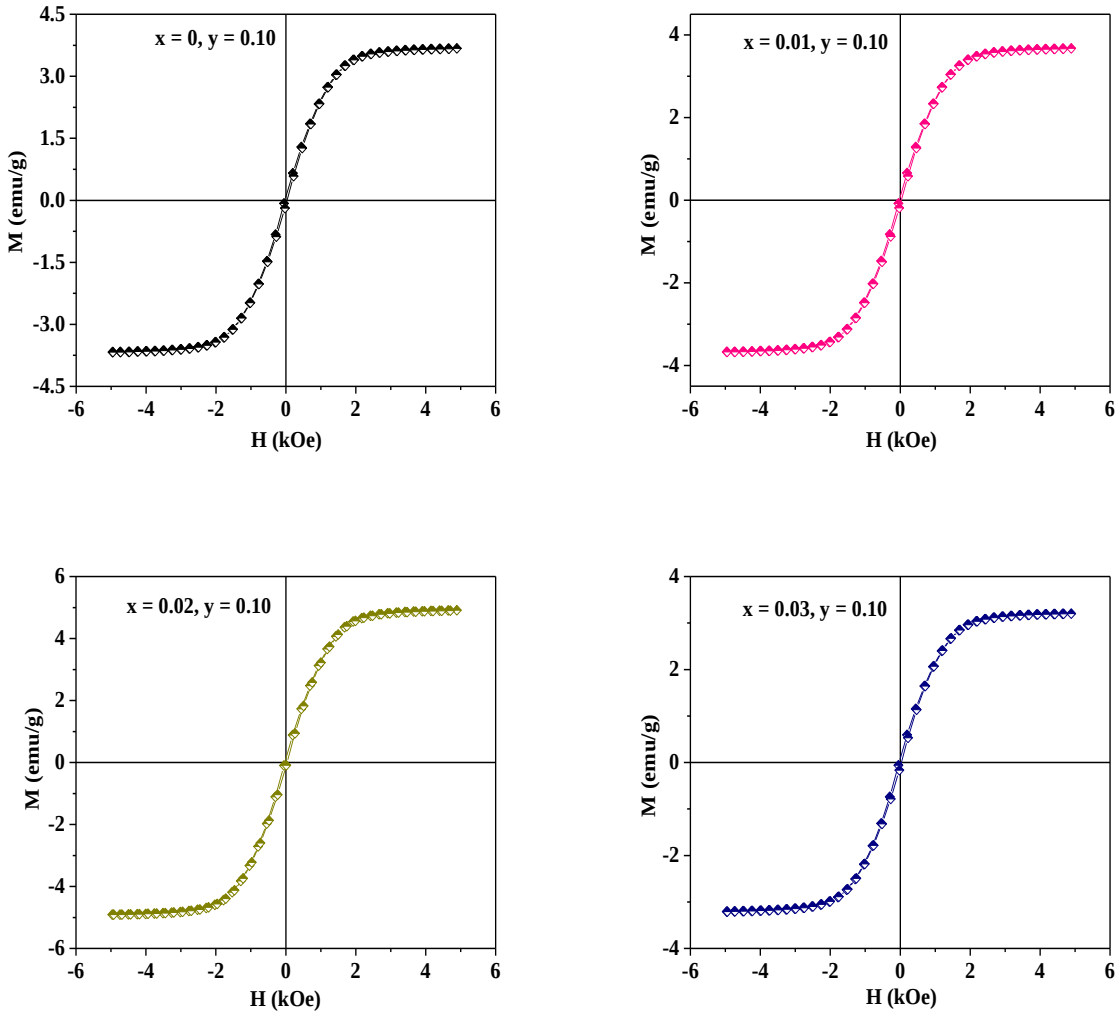

Figure 4.23 M–H hysteresis loop for all samples of series 2C at room temperature

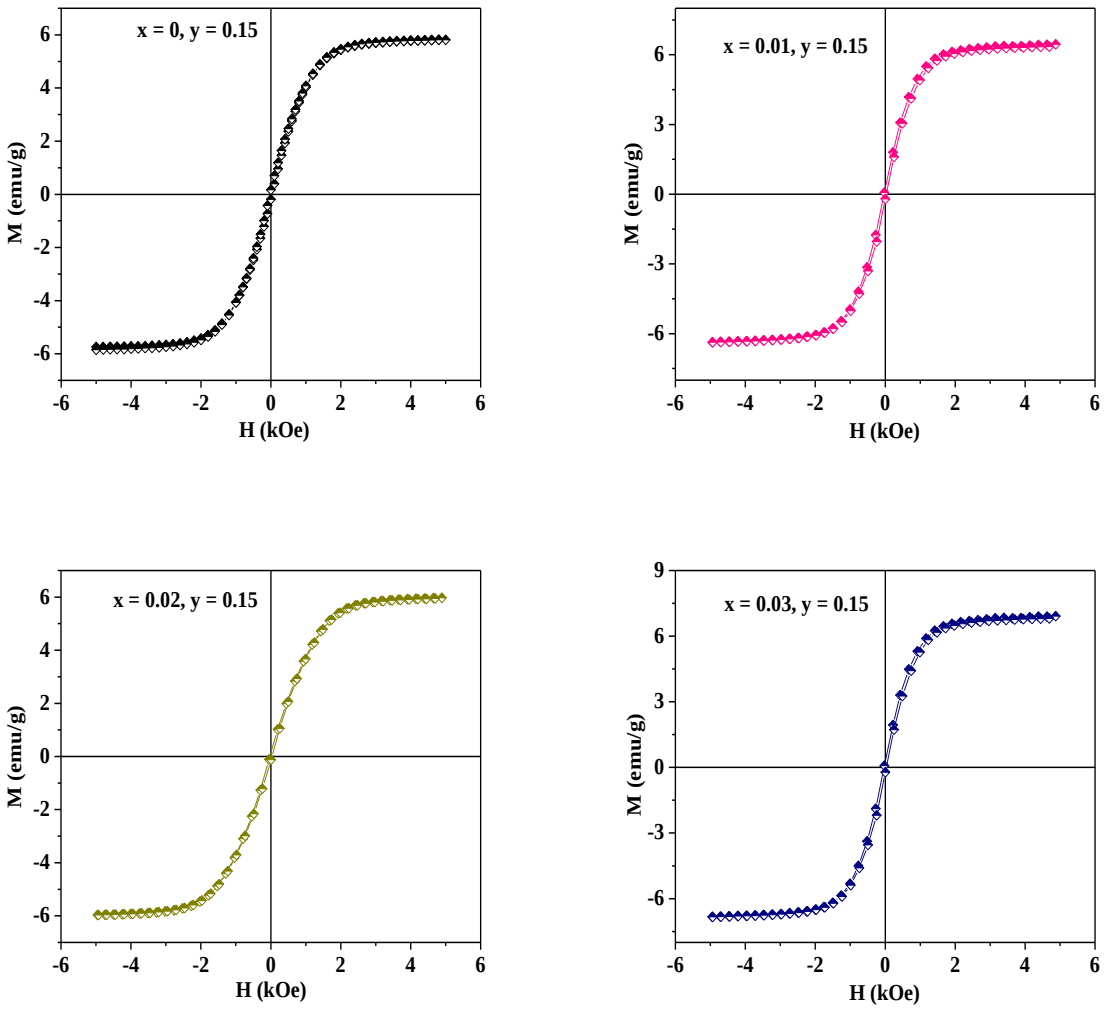

Figure 4.24 M–H hysteresis loop for all samples of series 2D at room temperature

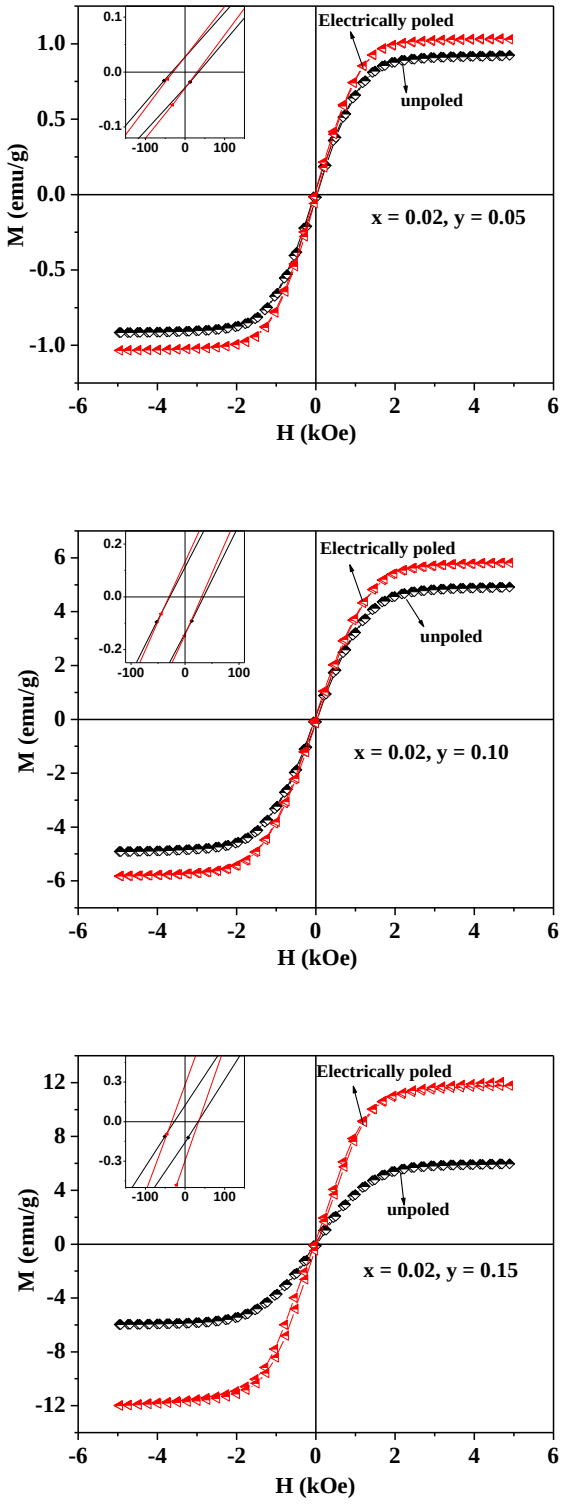

Figure 4.25 M–H hysteresis loops for electrically poled and unpoled samples with x = 0.02 and y = 0.05, 0.10, 0.15 at room temperature

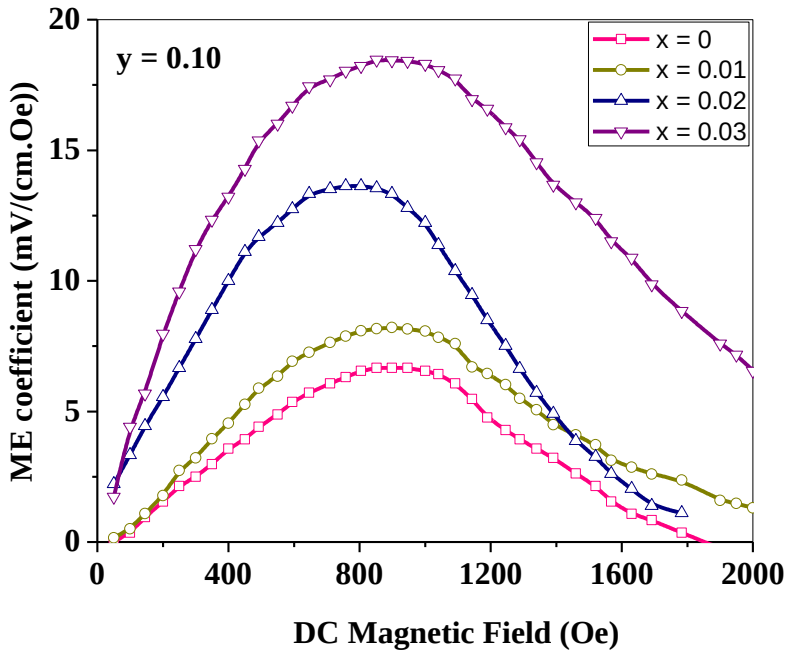

Figure 4.26 Variation of ME coupling coefficient, α (mV/(cm.Oe)) with DC magnetic field for series 2C

Maximum value of α for samples of series 2C was determined from curves and listed in table 4.3 for comparison. Increase in maximum value of α with increase in La substitution (x) is observed. It is known that ME coupling in ferrite–ferroelectric composites depends on the magnetostriction of the ferrite phase and piezoelectricity of the ferroelectric phase [43]. For the present case, increase in piezoelectric charge coefficient (d_{33}) with increase in La substitution is observed (section 4.3.5), hence increase in ME coupling coefficient, α is expected. Maximum coupling coefficient of 18.5 mV/(cm.Oe) is observed for x = 0.03 and due to higher d_{33} value of ~ 89 pC/N as compared to others. The maximum values of α obtained for x = 0, 0.01 and 0.02 are 6.7 mV/(cm.Oe), 8.2 mV/(cm.Oe) and 13.6 mV/(cm.Oe) respectively. As expected, these values are higher to those reported for bulk ferrite–ferroelectric composites in literature [44–47] because of the La substitution.

Table 4.3 Values of P_r, E_c, M_r, M_s, H_c, d_{33} and α for NZF–PLZT samples

Parameters x	**P_r ($\mu C/cm^2$)**	**E_c (kV/cm)**	**M_r (emu/g)**	**M_s (emu/g)**	**H_c (Oe)**	**d_{33} (pC/N)**	**α mV/(cm.Oe)**
***Series 2A* (y = 0)**							
0	7.9	5.3	–	–	–	108	–
0.01	16.6	5.5	–	–	–	116	–
0.02	23.5	6.2	–	–	–	129	–
0.03	32.5	7.2	–	–	–	139	–
***Series 2B* (y = 0.05)**							
0	1.9	4.7	0.05	1.7	30	85	3.8
0.01	2.1	4.4	0.09	2.7	30	90	–
0.02	2.8	4.8	0.03	0.9	30	108	–
0.03	4.3	5.3	0.03	0.8	40	120	–
***Series 2C* (y = 0.10)**							
0	1.1	4.6	0.09	3.7	30	72	6.7
0.01	1.5	4.9	0.09	3.7	30	76	8.2
0.02	1.6	4.2	0.12	4.9	30	80	13.6
0.03	1.8	4.5	0.09	3.2	30	89	18.5
***Series 2D* (y = 0.15)**							
0	lossy		0.09	5.7	30	53	4.1
0.01	lossy		0.22	6.5	30	56	–
0.02	lossy		0.14	6.0	30	58	–
0.03	lossy		0.24	6.9	30	68	–

References

1. X. Dai, Z. Xu, J.F. Li and D. Viehland, J. Mater. Res., **11** (1996) 618.
2. P. Singh, Ph.D. Thesis, Thapar University, Punjab, India (2011).
3. B. Jaffe, W.R. Cook and H. Jaffe, Piezoelectric Ceramics, Academic Press, New York (1971).
4. L. Pdungsap, N. Udomkan, S. Boonyuen and P. Winotai, Sens. Actuators A, **122** (2005) 250.
5. A.S. Fawzi, A.D. Sheikh and V.L. Mathe, Physica B, **405** (2010) 340.
6. W. Robner, Ph.D. Thesis, University of Erlangen, Erlangen, Germany (1985).
7. K. Carl and K.H. Hardtl, Ber. Dtsch. Keram. Ges., **47** (1970) 687.
8. C. Prakash and O.P. Thakur, Mater. Lett., **57** (2003) 2310.
9. L. Zivkovic, V. Paunovic, M. Miljkovic and M.M. Rustic, Mater. Sci. Forum, **518** (2006) 229.
10. G.H. Haertling, J. Am. Ceram. Soc., **82** (1999) 797.
11. X. Feng and X. Yao, J. Appl. Phys., **92** (2002) 2709.
12. L. Mitoseriu and V. Buscaglia, Phase Transitions, **79** (2006) 1.
13. J. Chen, Z. Xu and X. Lu, Ferroelectr. Lett., **410** (2011) 29.
14. R. Rani, P. Kumar, J.K. Juneja, K.K. Raina and C. Prakash, Adv. Condens. Matter Phys., **2011** (2011) 637170.
15. A.J. Moulson and J.M. Herbert, Electroceramics: Materials, Properties, Applications, Chapman and Hall, London (1990).
16. K.K. Patankar, S.A. Patil, K.V. Sivakumar, Y.D. Kolekar and M.B. Kothale, Mater. Chem. Phys., **65** (2000) 97.
17. K.K. Patankar, V.L. Mathe, A.N. Patil, Y.D. Kolekar and P.B. Joshi, J. Electroceram., **6** (2001) 115.
18. R.C. Kambale, P.A. Shaikh, K.Y. Rajpure, P.B. Joshi and Y.D. Kolekar, Integr. Ferroelectr., **121** (2010) 1.
19. L.L. Hench and J.K. West, Principles of Electronics Ceramics, John Wiley and Sons, New York (1990).
20. M. Zivkovic, D. Stojanovic, C.R. Foschini, V. Paunovic and D. Mancic, Sci. Sinter., **35** (2003) 133.

21. S.B. Narang and D. Kaur, Ferroelectr. Lett., **36** (2009) 20.
22. J.Y. Zhai, N. Cai, L. Liu, Y.H. Lin and C.W. Nan, Mater. Sci. Eng. B, **99** (2003) 329.
23. D.R. Patil and B.K. Chougule, J. Alloys Compd., **470** (2009) 531.
24. J.S. Kim, B.C. Choi, H.K. Yang and J.H. Jeong, J. Korean Phys. Soc., **52** (2008) 415.
25. S. Singh, O.P. Thakur, C. Prakash and K.K. Raina, Phase Transitions, **78** (2005) 655.
26. L.I. Maissel and R. Glang, Handbook of Thin Film Technology, McGraw–Hill, New York (1970).
27. S.R. Shannigrahi, R.N.P. Choudhary and H.N. Acharaya, J. Mater. Sci., **35** (2000) 1737.
28. H. Ouchi, J. Am. Ceram. Soc., **51** (1968) 169.
29. L.E. Cross, Ferroelectrics, **76** (1987) 241.
30. S. Li, J.A. Eastman, R.E. Newnham and L.E. Cross, Phys. Rev. B, **55** (1997) 12067.
31. R. Yimnirun, S. Ananta and P. Loaratanakul, Mater. Sci. Eng. B, **112** (2004) 79.
32. S.L. Swartz, T.R. Shrout, W.A. Schulze and L.E. Cross, J. Am. Ceram. Soc., **67** (1984) 311.
33. J.D. Mackenzie and Y. Xu, J. Sol–Gel Sci. Technol., 8 (1997) 673.
34. X. Chao, Z. Yang, M. Dong and Y. Zhang, J. Magn. Magn. Mater., **323** (2011) 2012.
35. D. Pandey, N. Singh and S.K. Mishra, Indian J. Pure Appl. Phys., **32** (1994) 616.
36. H.J. Hagemann, J. Phys. C, **11** (1978) 3333.
37. M.J. Haun, E. Furman, S.J. Jang and L.E. Cross, IEEE T. Ultrason. Ferr., **36** (1989) 393.
38. W. Wersing, K. Lubitz and J. Mohaupt, IEEE T. Ultrason. Ferr., **36** (1989) 424.
39. D. Wu, W. Gong, H. Deng and M. Li, J. Phys. D: Appl. Phys., **40** (2007) 5002.
40. C.M. Kanamadi, J.S. Kim, H.K. Yang, B.K. Moon, B.C. Choi and J.H. Jeong, Appl. Phys. A, **97** (2009) 575.
41. R.S. Devan, S.B. Deshpande and B.K. Chougule, J. Phys. D: Appl. Phys., **40** (2007) 1864.
42. A. Singh and R. Chatterjee, Appl. Phys. Lett., **93** (2008) 182908.
43. C.W. Nan, Phys. Rev. B, **50** (1994) 6082.
44. G.V. Duong and R. Groessingera, J. Magn. Magn. Mater., **316** (2007) e624.
45. C.M. Kanamadi, J.S. Kim, H.K. Yang, B.K. Moon, B.C. Choi and J.H. Jeong, J. Alloys Compd., **481** (2009) 781.
46. A. Gupta and R. Chatterjee, J. Magn. Magn. Mater., **322** (2010) 1020.
47. V.M. Laletin and V.M. Petrov, Solid State Commun., **151** (2011) 1806.

Chapter-V

Characterization of NZF-PSZT Composites

Chapter–V

Characterization of NZF–PSZT Composites

Detailed studies on NZF–PLZT composite series (chapter IV) show that the substitution of La in ferroelectric phase (PZT) results in significant improvement in properties of pure ferroelectric samples (series 2A) as well as of composite samples (series 2B, 2C and 2D). Samples with 15% ferrite content (y = 0.15) show lossy ferroelectric (P–E) loops due to high leakage current and lower ME output due to decrease in piezoelectric phase (decrease in induced charge). Though La substitution results in improved properties for y = 0.15 (series 2D) but the results are still better for y = 0.05 and 0.10 (series 2B and 2C).

Effect of Sm substitution in PZT phase is also studied and the experimental results of composites of NiZn ferrite and Sm substituted lead zirconate titanate (NZF–PSZT) are discussed in this chapter. Composites having general formula $yNi_{0.8}Zn_{0.2}Fe_2O_4–(1–y)Pb_{1–3x/2}Sm_xZr_{0.65}Ti_{0.35}O_3$ with x = 0.01, 0.02, 0.03 and y = 0.05, 0.10 (series 3) were synthesized and characterized for their structural, dielectric, ferroelectric, piezoelectric, ferromagnetic and magnetoelectric properties. The following compositional series have been prepared for detailed investigations:

Series 3A: yNZF–(1–y)PSZT with x = 0, 0.01, 0.02, 0.03 and y = 0.05

Series 3B: yNZF–(1–y)PSZT with x = 0, 0.01, 0.02, 0.03 and y = 0.10

5.1 Synthesis of Individual Phases

The ferrite phase, $Ni_{0.8}Zn_{0.2}Fe_2O_4$ (NZF) and ferroelectric phase, $Pb_{1–3x/2}Sm_xZr_{0.65}Ti_{0.35}O_3$ (PSZT with x = 0, 0.01, 0.02 and 0.03) were synthesized by conventional solid state reaction route (details given in section 3.1, chapter III). X–ray diffraction analysis was carried out for identification of both phases (ferrite and ferroelectric). XRD patterns for NZF phase and PZT are

already given in figure 3.1 (chapter III) and for PSZT phase, $Pb_{1-3x/2}Sm_xZr_{0.65}Ti_{0.35}O_3$ (x = 0.01, 0.02 and 0.03) are shown in figure 5.1. The patterns for PSZT show that all calcined samples are in pure perovskite phase. The phase formation was confirmed with standard JCPDS file no. 89–1279 of PZT.

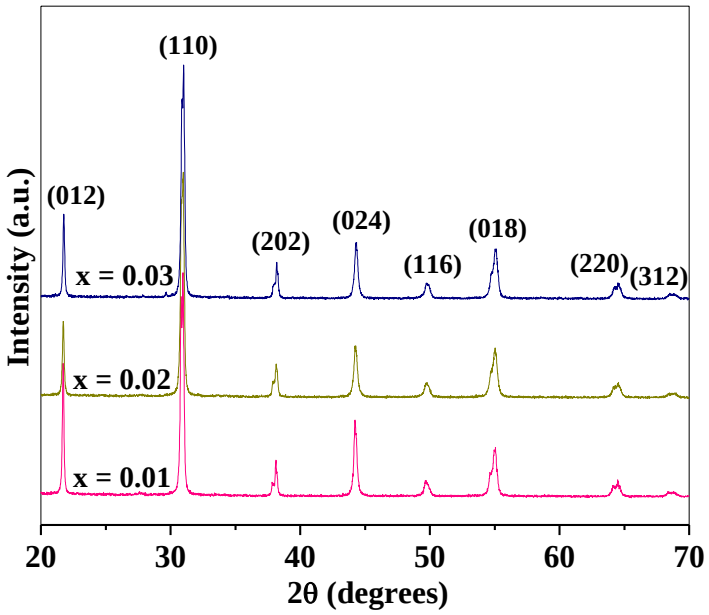

Figure 5.1 XRD patterns for PSZT calcined samples (x = 0.01, 0.02 and 0.03)

5.2 Synthesis of $yNi_{0.8}Zn_{0.2}Fe_2O_4–(1–y)Pb_{1–3x/2}Sm_xZr_{0.65}Ti_{0.35}O_3$

NZF–PSZT composites according to the formula $yNi_{0.8}Zn_{0.2}Fe_2O_4–(1–y)Pb_{1–3x/2}Sm_xZr_{0.65}Ti_{0.35}O_3$ with x = 0.01, 0.02, 0.03 and y = 0.05, 0.10 were prepared by mixing the two phases in desired ratio. Powder mixture was ball milled in the same planetary ball mill using distilled water and zirconia balls. After drying, the powder was mixed with small amount of diluted polyvinyl alcohol (3% by weight) as binder. This dried mixture was uniaxially pressed into disc shaped pellets with diameter ~ 15 mm and thickness ~ 1 mm. The pellets were finally sintered in a programmable furnace at optimized temperature i.e. 1200 ^oC for 4 hrs.

5.3 Characterization of $yNi_{0.8}Zn_{0.2}Fe_2O_4–(1–y)Pb_{1–3x/2}Sm_xZr_{0.65}Ti_{0.35}O_3$

5.3.1 X–Ray Diffraction

Figures 5.2 and 5.3 show the XRD patterns for NZF–PSZT series 3A and 3B respectively. The analysis shows that all samples are polycrystalline and composed by mixtures of cubic spinel NZF phase and rhombohedral perovskite PSZT phase. No extra peak other than diffraction peaks corresponding to pure phases (NZF and PSZT) was found indicating that no chemical reaction occurred between the constituent phases during sintering of NZF–PSZT composites. The peak intensities and their angular positions match fairly with the diffraction peaks of individual phases indicating that constituent phases retained their structure in composites even after the sintering.

The ionic radii of Sm^{+3} (1.38 Å) is smaller than that of Pb^{+2} (1.63 Å), hence slight shifting in diffraction peaks corresponding to ferroelectric phase (PSZT) towards higher angle side is observed with higher Sm content for both series. This indicates the decrease in lattice constant corresponding to ferroelectric phase due to substitution of less ionic size substituent at Pb site, as shown in table 5.1.

The values of lattice constant corresponding to ferrite phase were also calculated and given in table 5.1. The values are found to be random which may be due to stress induced by non–ferrite phase (PSZT) on ferrite phase (NZF) [1]. The experimental density, X–ray density and relative density values were determined for all samples of series 3A and 3B and given in table 5.1. Such variation in density values is expected [2–4] and already observed for NZF–PLZT samples (discussed in chapter IV).

5.3.2 Scanning Electron Microscope

The scanning electron microscope (SEM) micrographs of the freshly broken surfaces for the samples of series 3A and 3B with x = 0, 0.01 and 0.03 are shown in figures 5.4 and 5.5 respectively. The micrographs show closely packed and well oriented grains. The shape, size and distribution of grains confirm the polycrystalline nature for all the samples. The average grain size was calculated by using line intercept method and is given in table 5.1. The average grain

size of the samples was in the range 1.3–2.5 μm. The grain size is strongly influenced by the substituent content (x). Average grain size of the samples was found to decrease with increase in Sm substitution (x) for both series. The possible reason for the decrease in grain sizes with increase in Sm substitution can be attributed to the segregation of Sm around the grain boundaries [5].

Table 5.1 Structural parameters for NZF–PSZT samples

x	***Series 3A* (y = 0.05)**				***Series 3B* (y = 0.10)**			
	0	**0.01**	**0.02**	**0.03**	**0**	**0.01**	**0.02**	**0.03**
Lattice Constant (Å) (Ferroelectric phase)	4.106	4.105	4.095	4.083	4.104	4.096	4.089	4.088
Lattice Constant (Å) (Ferrite phase)	8.346	8.353	8.350	8.359	8.353	8.342	8.341	8.334
Exp. Density (g/cc)	7.31	7.18	7.33	7.16	6.88	6.91	6.89	7.04
X–ray Density (g/cc)	7.89	7.85	7.84	7.82	7.75	7.72	7.71	7.69
Relative Density (%)	92.7	91.5	93.5	91.6	88.8	88.2	89.4	91.5
Average grain size (μm)	2.5	1.7	–	1.3	2.4	1.9	–	1.5

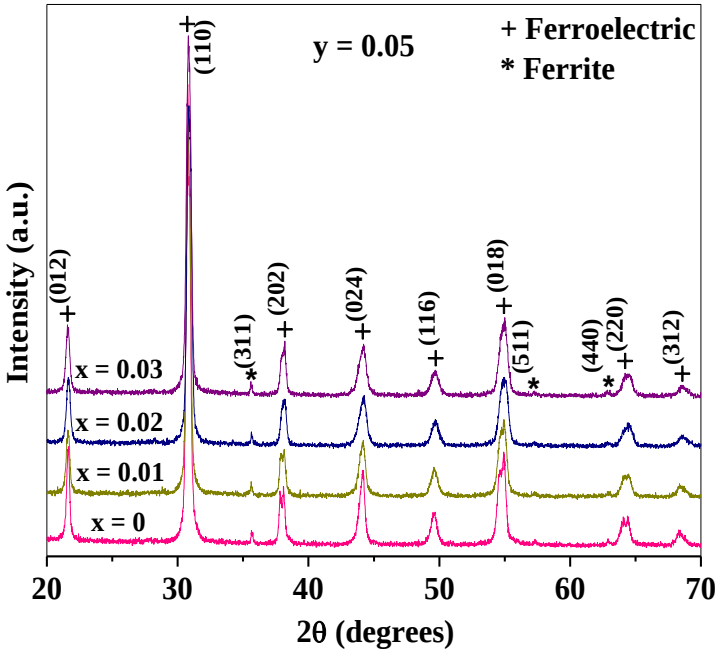

Figure 5.2 XRD patterns for all samples of series 3A

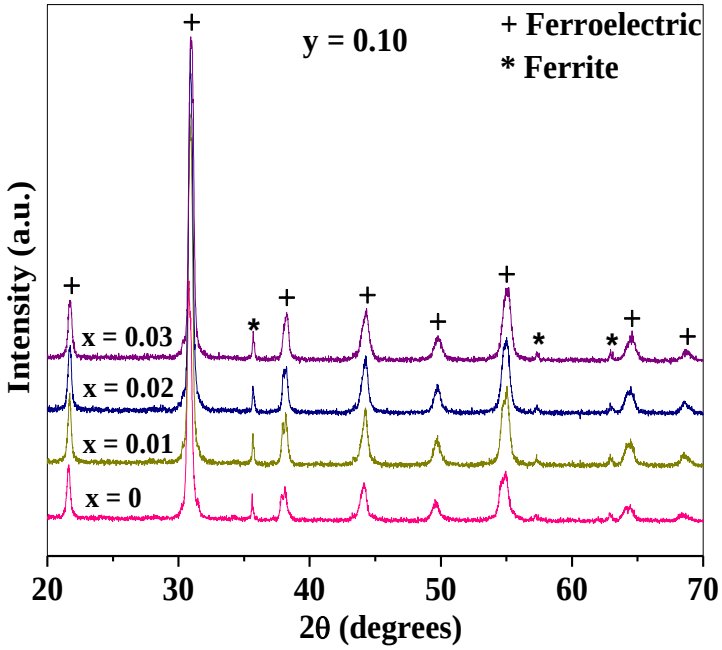

Figure 5.3 XRD patterns for all samples of series 3B

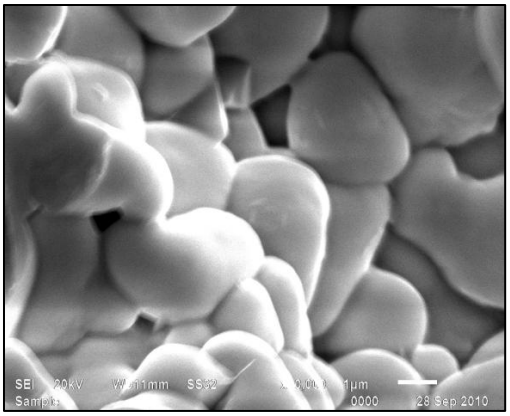

x = 0

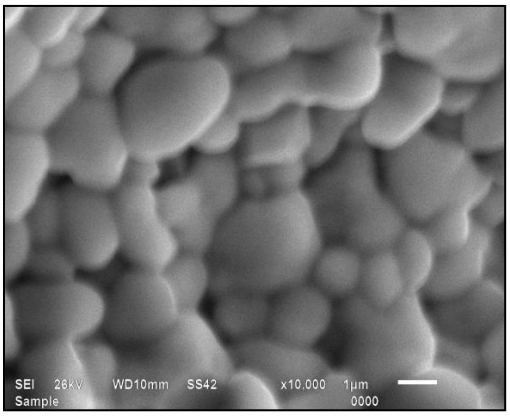

x = 0.01

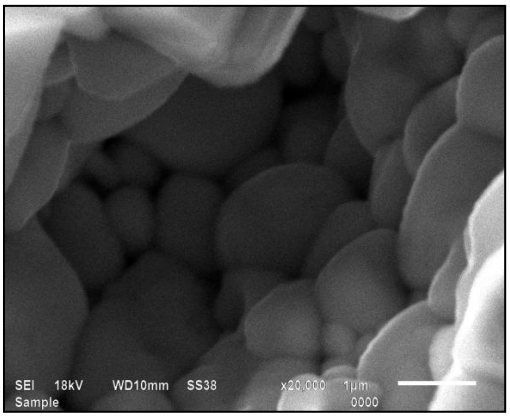

x = 0.03

Figure 5.4 SEM micrographs for the samples of series 3A (x = 0, 0.01 and 0.03)

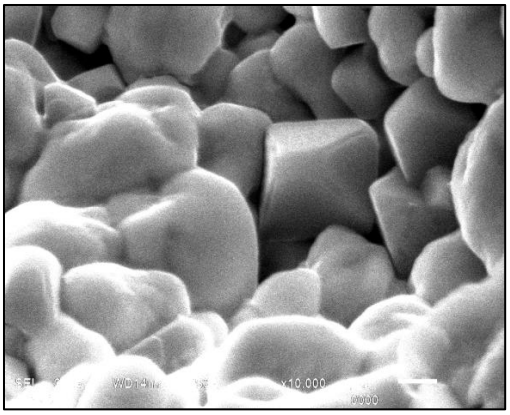

x = 0

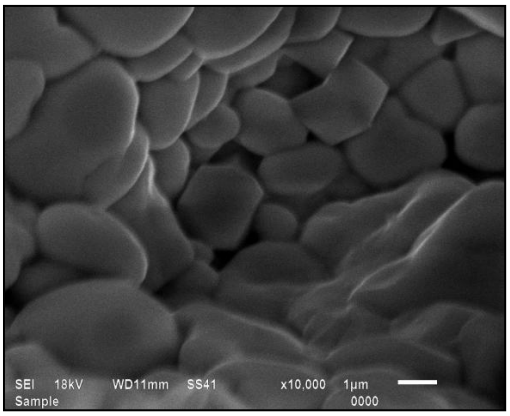

x = 0.01

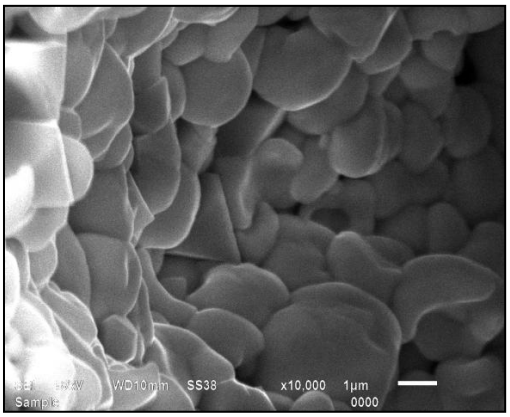

x = 0.03

Figure 5.5 SEM micrographs for the samples of series 3B (x = 0, 0.01 and 0.03)

5.3.3 Dielectric Properties

The temperature variation of dielectric constant (ε') and loss (tanδ) for NZF–PSZT composite system represented by series 3A and 3B is shown in figures 5.6 and 5.7 respectively with x = 0.01, 0.02 and 0.03. Temperature dependence was studied at three selected frequencies (1, 10 and 100 kHz) in the temperature range 35–500 ^{o}C. The graphs show an expected behavior and such variation in dielectric properties have already been reported by many research groups [6–12]. As temperature increases, initially the value of dielectric constant increases, attains a maximum at certain temperature (ferroelectric–paraelectric transition in PSZT phase) and then decreases for further increase in temperature for all composite samples. In the paraelectric region, an increase in dielectric constant with increase in temperature is observed at 1 kHz which is a result of thermally activated electron exchange interactions ($Fe^{+2} \leftrightarrow Fe^{+3}$ and $Ni^{+2} \leftrightarrow Ni^{+3}$) due to the presence of NZF phase [13]. High values of dielectric loss in paraelectric region are attributed to thermal conductivity losses at elevated temperatures due to the presence of NZF phase.

The values of ferroelectric Curie temperature (T_c), room temperature dielectric constant (ε'_{RT}), dielectric constant at T_c (ε'_{max}), room temperature dielectric loss ($\tan\delta_{RT}$) and dielectric loss at T_c ($\tan\delta_{max}$) for all samples are given in table 5.2. Decrease in T_c is observed with increase in Sm substitution for both series which is due to shrinkage in PZT lattice volume and substitution of smaller ionic size Sm (r = 1.38 Å) at Pb (r = 1.63 Å) site. There is significant increase in room temperature dielectric constant (ε'_{RT}) from ~ 625 to ~ 1175 and from ~ 590 to ~ 825 with increase in x from 0 to 0.03 for series 3A and 3B respectively. The values of ε' and tanδ given in table 5.2 show that Sm substitution results in improved dielectric properties for given NZF–PSZT composite system. Further, if we compare the dielectric properties for series of Sm (series 3A and 3B) and series of La (series 2B and 2C) with each other, it is observed that change in dielectric properties (ε' and tanδ) is more significant for Sm substituted series as compared to that for La substituted series. This may be due to more lattice anisotropy created in case of Sm substitution, as is evident from X–ray diffraction study (section 5.3.1).

The typical room temperature variation of dielectric constant (ε') and loss (tanδ) of Sm substituted composite samples (series 3A and 3B) as function of frequency (10^2–10^6 Hz) is depicted in figures 5.8 and 5.9. It is found that as frequency increases, dielectric constant

decreases which accounts for the normal behavior of dielectric materials. For series 3A, increase in tanδ at higher frequencies is observed which may be due to some extrinsic loss phenomenon [14, 15] or may be due to the fast increase in ohmic component of the current than the reactive component [16]. Further, if we compare the variation of ε' and tanδ with frequency for unsubstituted sample (x = 0) with that for substituted ones (x = 0.02 and 0.03), it is observed that the dispersion is decreasing with increase in Sm substitution (x) for both series (series 3A and 3B). This behavior can be explained on the same lines as in case of NZF–PLZT samples (discussed in section 4.3.3, chapter IV). Sm substitution reduces the number of Pb vacancies and counteracts the p–type conduction in PSZT phase resulting in decrease in low–frequency dispersion [17, 18]. Similar trends in variation of dielectric properties with frequency are observed for many ferrite–ferroelectric bulk composites [19–21]. The investigated samples with x = 0.02 and 0.03 are suitable for low loss applications in this frequency range (10^2–10^6 Hz).

Table 5.2 Dielectric parameters for NZF–PSZT samples at 100 kHz

x	***Series 3A* (y = 0.05)**				***Series 3B* (y = 0.10)**			
	0	**0.01**	**0.02**	**0.03**	**0**	**0.01**	**0.02**	**0.03**
$\mathbf{T_c\ (^oC)}$	394	393	382	368	408	401	375	362
$\mathbf{\varepsilon'_{RT}}$	625	775	975	1175	590	550	740	825
$\mathbf{\varepsilon'_{max}}$	10760	9805	9120	8260	7635	5740	7025	5950
$\mathbf{tan\delta_{RT}}$	0.03	0.01	0.01	0.02	0.03	0.01	0.01	0.02
$\mathbf{tan\delta_{max}}$	0.15	0.16	0.11	0.08	0.22	0.21	0.15	0.11

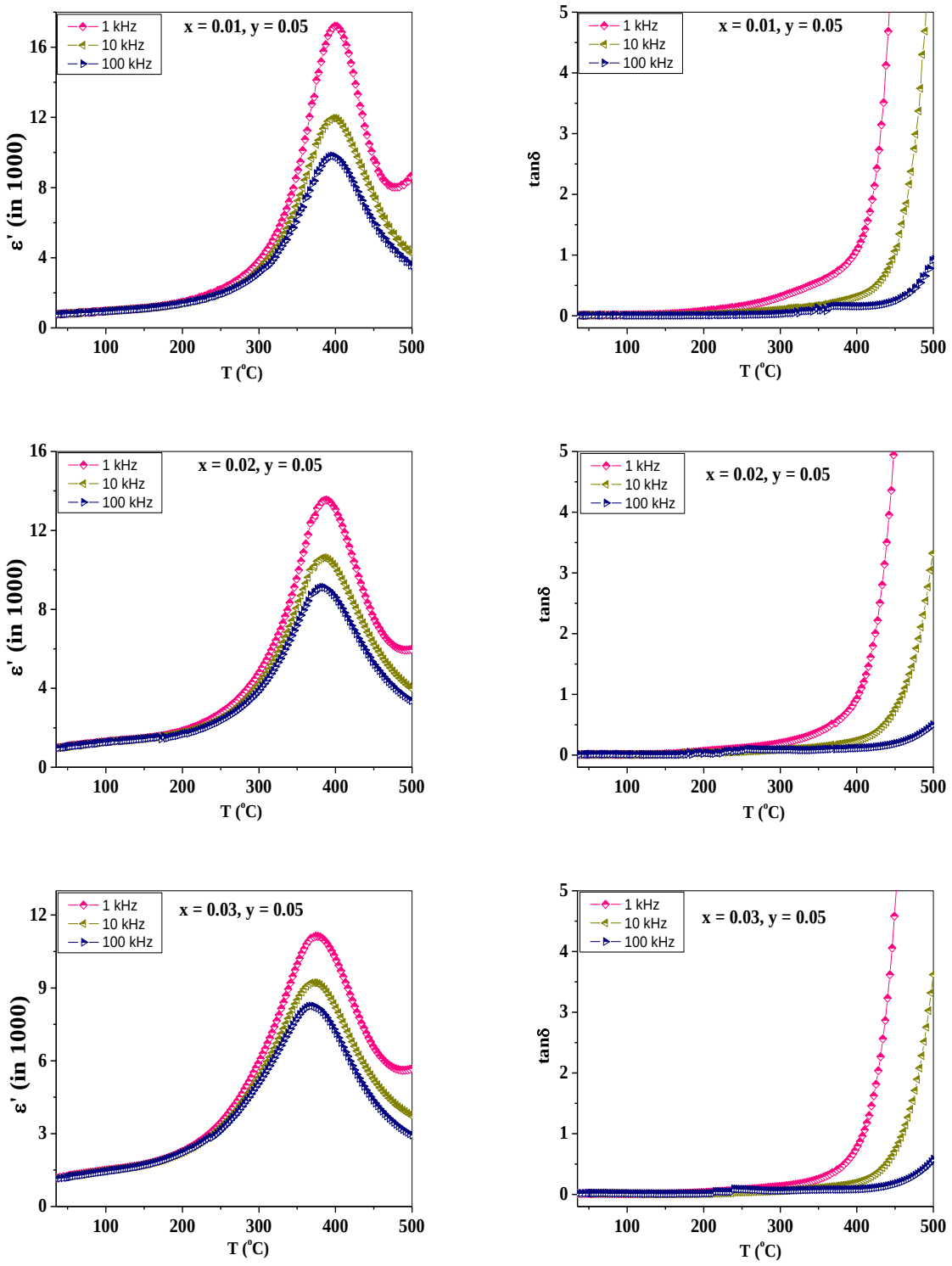

Figure 5.6 Variation of dielectric constant (ε') and loss (tanδ) with temperature for the samples of series 3A (x = 0.01, 0.02 and 0.03) at 1, 10 and 100 kHz

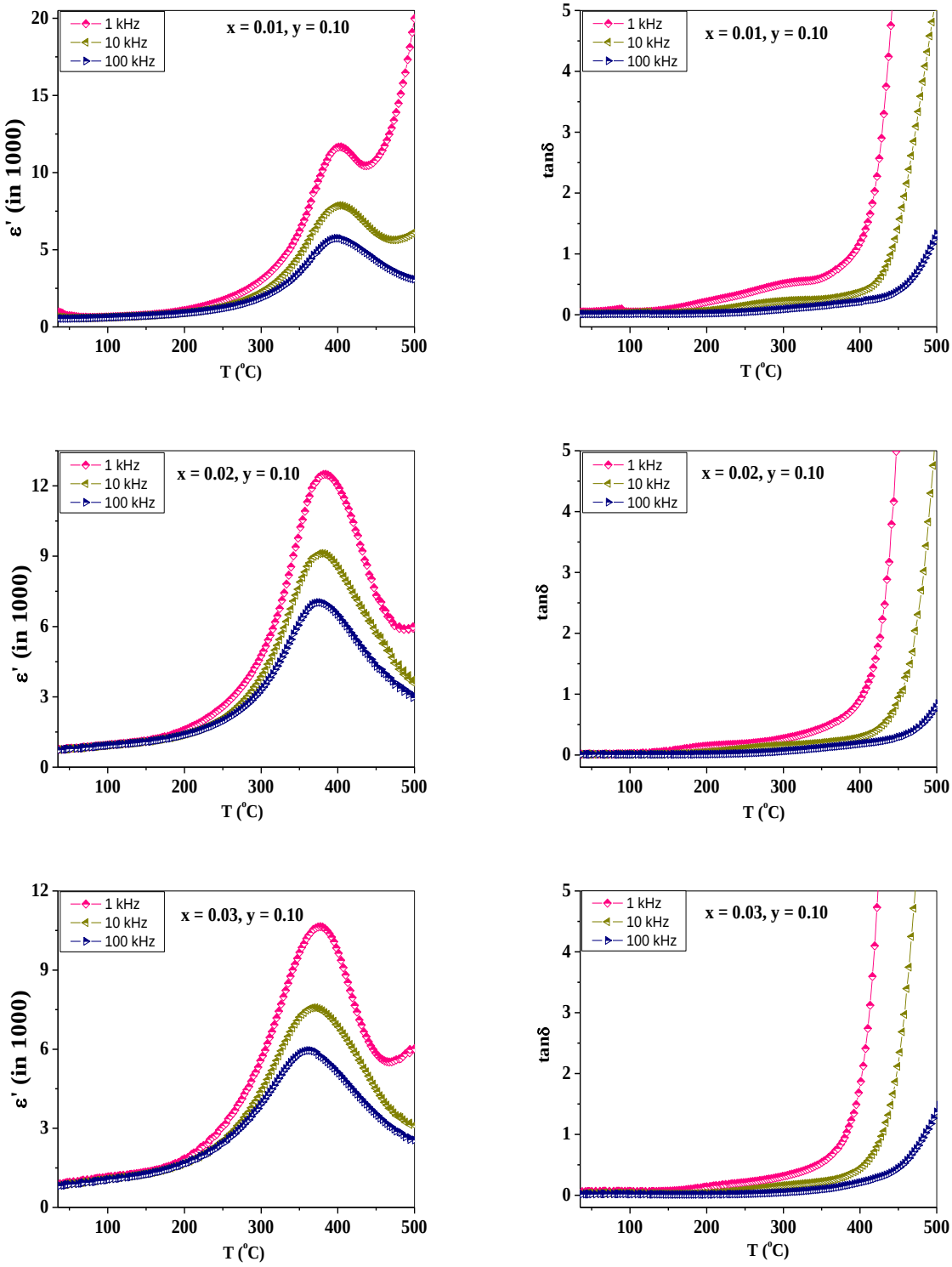

Figure 5.7 Variation of dielectric constant (ε') and loss (tanδ) with temperature for the samples of series 3B (x = 0.01, 0.02 and 0.03) at 1, 10 and 100 kHz

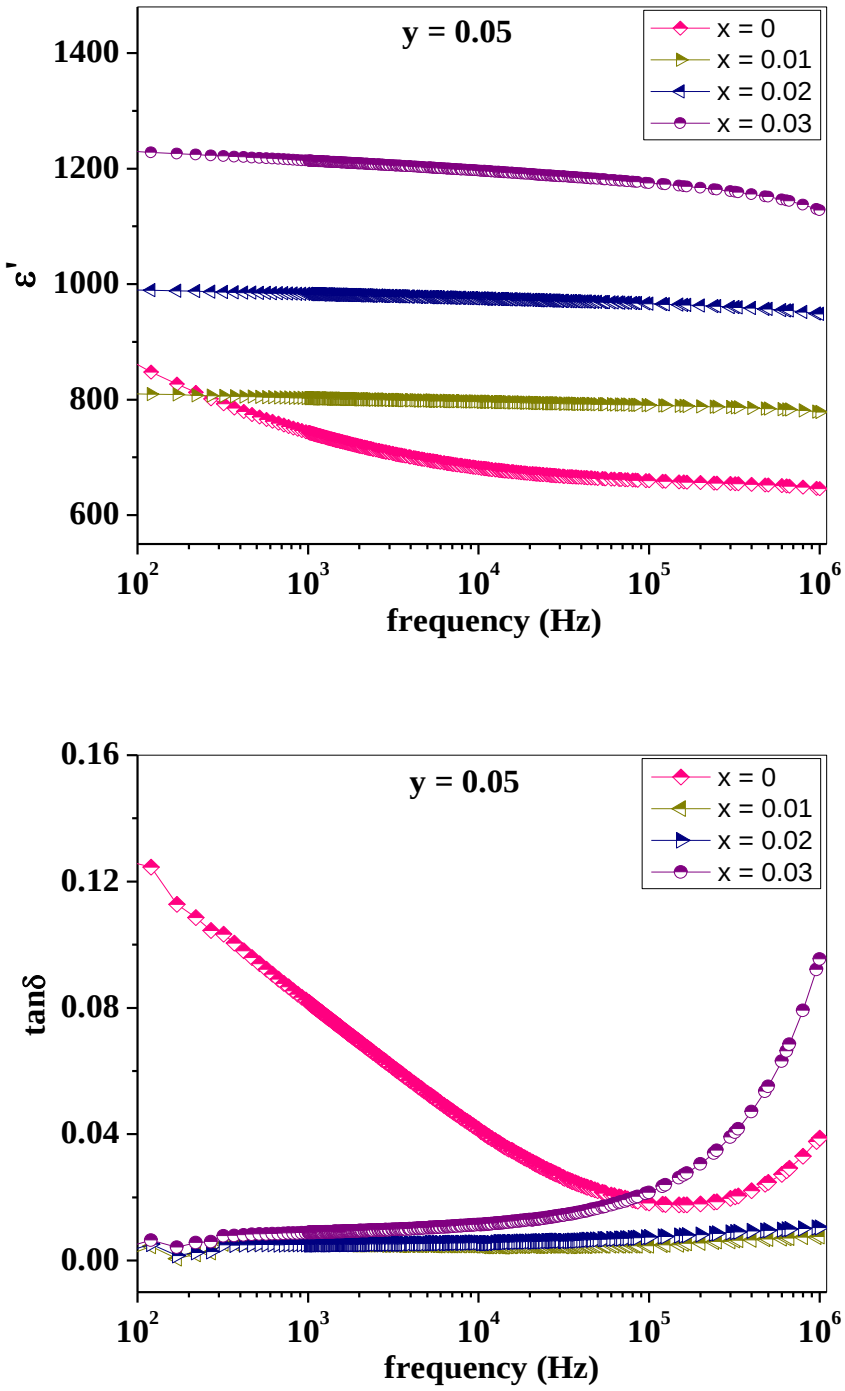

Figure 5.8 Variation of dielectric constant (ε') and loss (tanδ) with frequency for all samples of series 3A at room temperature

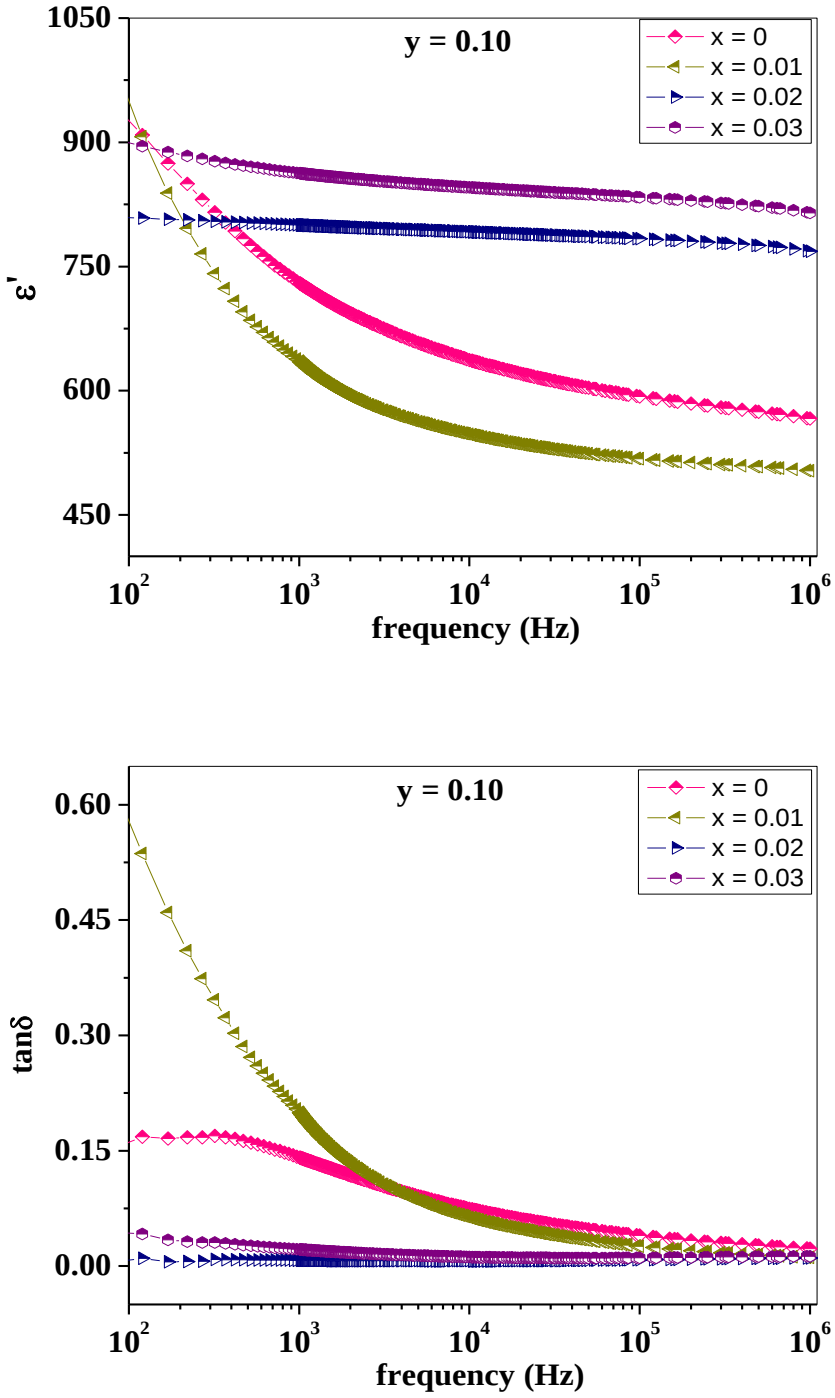

Figure 5.9 Variation of dielectric constant (ε') and loss (tanδ) with frequency for all samples of series 3B at room temperature

5.3.4. Ferroelectric Properties

To study ferroelectric behavior of NZF–PSZT composite samples, room temperature P–E hysteresis loops were recorded for all the samples (series 3A and 3B) at 20 Hz and are shown in figures 5.10 and 5.11. P–E loops obtained for all composite samples are unsaturated and asymmetric. This may be due to the defects created by NZF phase (ferrite phase) because the P–E loops obtained in composites are due to the presence of PSZT as ferroelectric phase and NZF as non–ferroelectric phase. Similar loops were obtained by X. Chao et al. [22], Pandey et al. [23] and Hagemann [24]. It is also observed that positive values of E_c, P_r and their counterparts are asymmetric about the origin which may be attributed to the internal bias field developed in the ferroelectric phase, electrode/PZT interface or due to defects [1, 25] present in samples for both series (series 3A and 3B).This asymmetry is higher for series 3B having higher ferrite content (y).

Values of remanant polarization (P_r) and coercive field (E_c) were determined from P–E loops for all the samples and are given in table 5.3. With increase in Sm substitution (x), increase in P_r and decrease in E_c was observed except for x = 0.03. The reason for increase in P_r and decrease in E_c is due to the softening effect of Sm^{+3} resulting in creation of A–site vacancies. It is also well reported in literature that substituents like La and Sm make the materials more soft i.e. increase in P_r and decrease in E_c [26]. If we compare these results with that obtained for NZF–PLZT samples of series 2B and 2C, it can be seen that Sm^{+3} substitution makes the materials more soft resulting in higher P_r, P_s and lower E_c as compared to that for La^{+3} substitution which may be due to the significant change in lattice anisotropy in case of Sm substitution as is evident from X–ray diffraction study.

5.3.5 Piezoelectric Properties

The values of piezoelectric charge coefficient (d_{33}) for NZF–PSZT composites (series 3A and 3B) are listed in table 5.3. As Sm substitution (x) increases from 0 to 0.03, the d_{33} values increase from ~ 85 to ~ 125 pC/N and from ~ 72 to ~ 92 pC/N for series 3A and 3B respectively. This behavior can be explained on the basis of the fact that composition influences the dielectric

permittivity, electrostriction coefficient and spontaneous polarization. These parameters are directly related to the d_{33} values as in case of NZF–PLZT composite system (section 4.3.5).

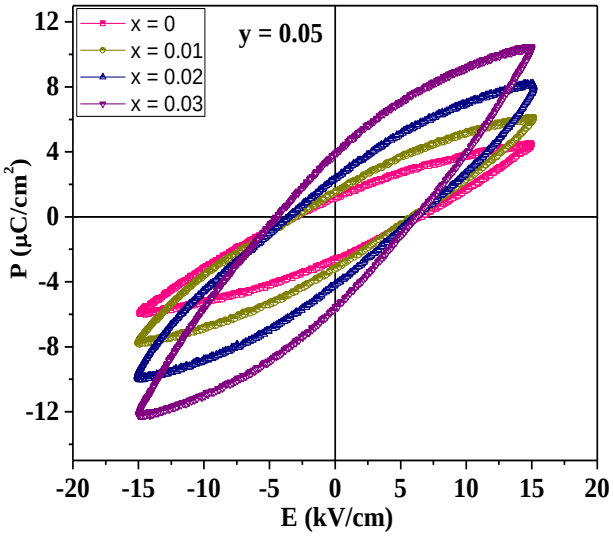

Figure 5.10 Room temperature P–E hysteresis loop for all samples of series 3A (x = 0, 0.01, 0.02 and 0.03) at 20 Hz

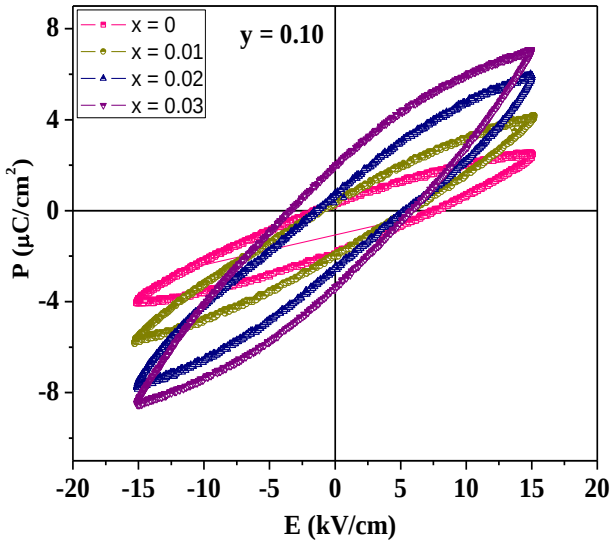

Figure 5.11 Room temperature P–E hysteresis loop for all samples of series 3B (x = 0, 0.01, 0.02 and 0.03) at 20 Hz

5.3.6 Ferromagnetic Properties

To study magnetic behavior of NZF–PSZT composite samples, room temperature M–H hysteresis loops were recorded for series 3A and 3B with x = 0.01, 0.02 and 0.03 and are shown in figures 5.12 and 5.13 respectively. All the samples show well defined ferromagnetic behavior and confirm the existence of magnetic ordering in the mixed spinel–perovskite (ferrite–ferroelectric) composite system. Values of remanant magnetization (M_r), saturation magnetization (M_s) and coercive field (H_c) were determined from M–H hysteresis loops for all samples and are given in table 5.3. Small values of H_c for these samples indicate their soft magnetic behavior. One can easily observe that the values of remanant magnetization (M_r) and saturation magnetization (M_s) are higher for samples of series 3B with higher ferrite content, as expected and are in fair agreement with the literature [27–30]. The reason is that in given composite system, NZF (ferrite) grains are connected with neighbouring PSZT (ferroelectric) grains and with increase in NZF content, magnetic contacts should increase [31] resulting in higher values for samples of series 3B.

5.3.7 Magnetoelectric Properties

To study magnetoelectric behavior in NZF–PSZT composite sample of series 3A with x = 0.02, two pieces from single pellet were taken. One piece was electrically poled at 15 kV/cm. M–H hysteresis loops were recorded for both poled and unpoled samples and the data was compared. M–H hysteresis loops at room temperature for both samples are shown in figure 5.14. An enhancement in saturation magnetization (from 1.9 to 2.3 emu/g) for poled sample was observed, which confirms the magnetoelectric coupling between NZF phase and PSZT phase for this sample. An enhancement of approximately 20 % was observed which can be exploited for sensor applications.

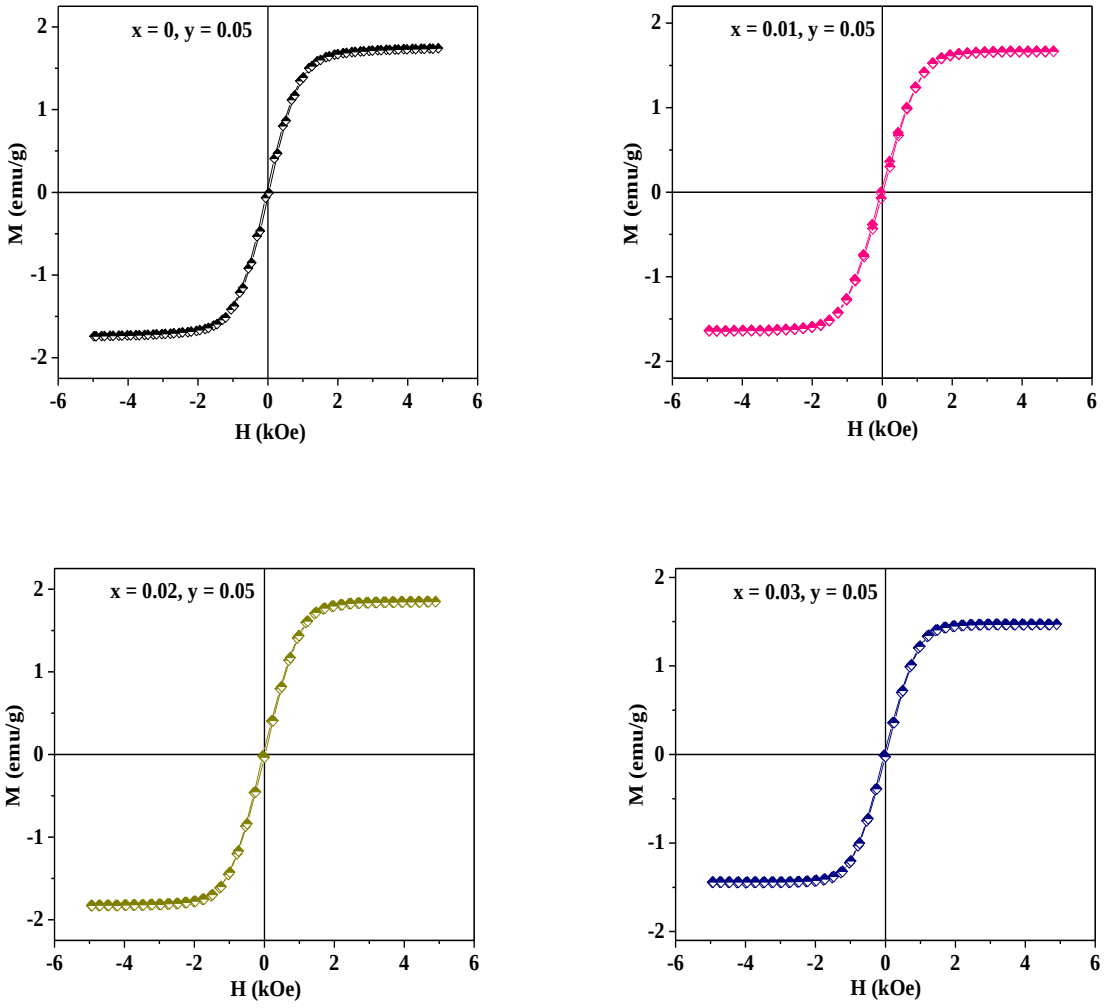

Figure 5.12 M–H hysteresis loop for all samples of series 3A at room temperature

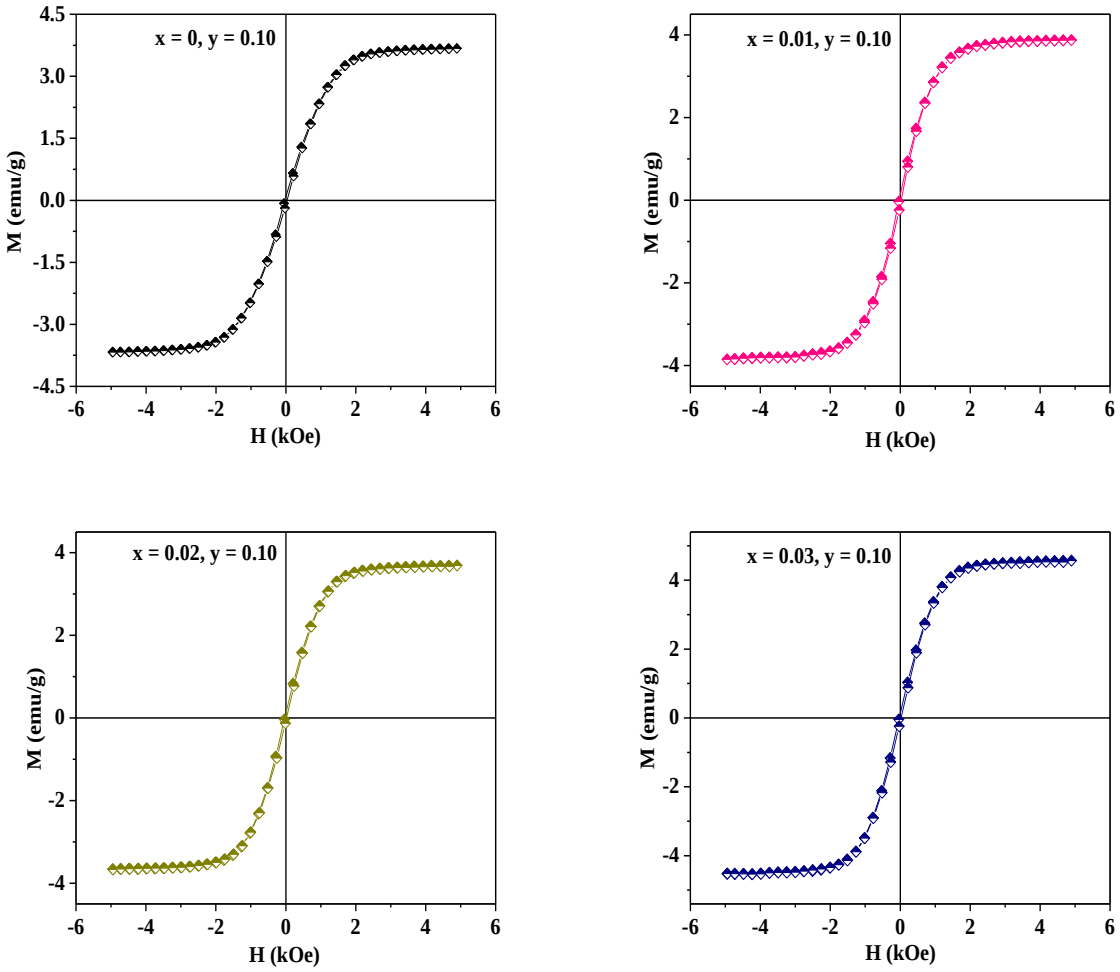

Figure 5.13 M–H hysteresis loop for all samples of series 3B at room temperature

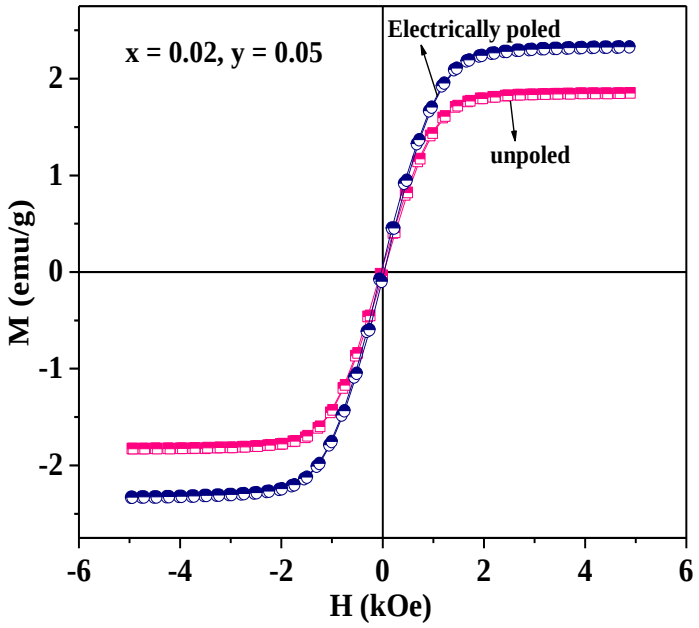

Figure 5.14 M–H hysteresis loops for electrically poled and unpoled samples with x = 0.02 and y = 0.05 at room temperature

Effect of Sm substitution on ME coupling coefficient is also studied for y = 0.10 i.e. for samples of series 3B. Figure 5.15 shows the typical variation of ME coupling coefficient (α) with applied DC magnetic field for all samples. The experiment was performed in the presence of AC magnetic field of strength 10 Oe at 1 kHz. The appearance of ME signal in NZF–PSZT composites is due to the strain induced in ferrite phase (NZF) by applied magnetic field which leads to polarization in the piezoelectric phase (PSZT). The trend of changing α with applied magnetic field is similar to as observed for NZF–PLZT composites. Initially α increases for lower magnetic field values, reaches to maximum and then starts decreasing for higher magnetic field values for all samples. The curves show a maximum at DC magnetic field in the range of ~ 800–950 Oe.

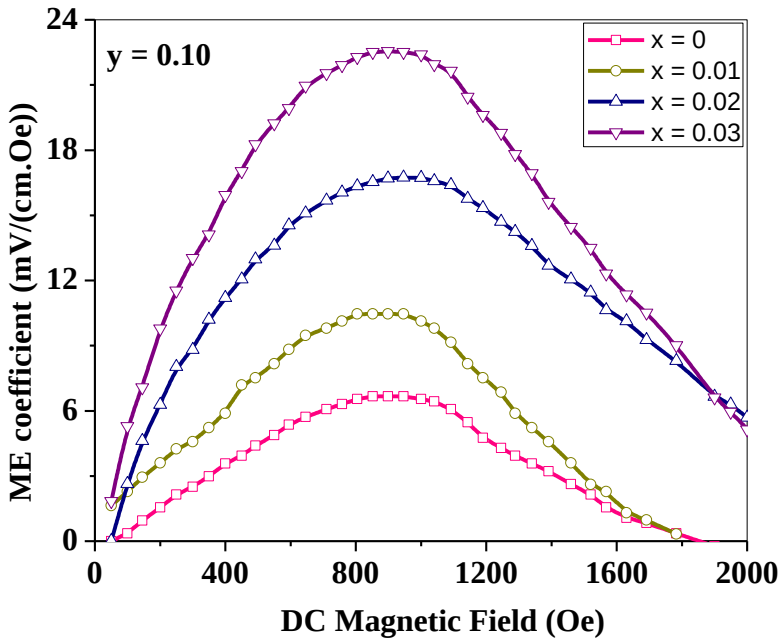

Figure 5.15 Variation of ME coupling coefficient, α (mV/(cm.Oe)) with DC magnetic field for all samples of series 3B

The maximum value of α is given in table 5.3 for all samples. As Sm substitution (x) increases, increase in α is observed which could be attributed to the piezoelectric properties. Sample with x = 0.03 exhibited the highest ME coupling coefficient due to the fact that its piezoelectric charge coefficient (d_{33}) is higher as compared to other samples. These results are in fair agreement with the theoretical prediction [32]. Maximum α of 22.5 mV/(cm.Oe) is observed for the composite sample with x = 0.03 and y = 0.10 and is higher as compared to those reported for bulk ferrite–ferroelectric composites in literature [33–35] because of Sm substitution.

Table 5.3 Values of P_r, E_c, M_r, M_s, H_c, d_{33} and α for NZF–PSZT samples

x	***Series 3A*** **(y = 0.05)**				***Series 3B*** **(y = 0.10)**			
	0	**0.01**	**0.02**	**0.03**	**0**	**0.01**	**0.02**	**0.03**
P_r (μC/cm^2)	1.9	2.3	3.3	4.7	1.1	1.3	1.7	2.7
E_c (kV/cm)	4.7	4.4	4.7	5.3	4.6	3.4	3.3	4.6
M_r (emu/g)	0.05	0.05	0.05	0.04	0.09	0.11	0.10	0.12
M_s (emu/g)	1.7	1.7	1.9	1.5	3.7	3.9	3.7	4.6
H_c (Oe)	30	30	30	30	30	30	30	30
d_{33} (pC/N)	85	92	115	125	72	75	83	92
α (mV/(cm.Oe))	3.8	–	–	–	6.7	10.5	16.7	22.5

References

1. A.S. Fawzi, A.D. Sheikh and V.L. Mathe, Phys. B, **405** (2010) 340.
2. W. Robner, Ph.D. Thesis, University of Erlangen, Erlangen, Germany (1985).
3. K. Carl and K.H. Hardtl, Ber. Dtsch. Keram. Ges., **47** (1970) 687.
4. C. Prakash and O.P. Thakur, Mater. Lett., **57** (2003) 2310.
5. L. Zivkovic, V. Paunovic, M. Miljkovic and M.M. Rustic, Mater. Sci. Forum, **518** (2006) 229.
6. Y.H. Tang, X.M. Chen, Y.J. Li and X.H. Zheng, Mater. Sci. Eng. B, **116** (2005) 150.
7. S.R. Kulkarni, C.M. Kanamadi and B.K. Chougule, J. Phys. Chem. Solids, **67** (2006) 1607.
8. T. Bonaedy, K.M. Song, K.D. Sung, N. Hur and J.H. Jung, Solid State Commun., **148** (2008) 424.
9. J.H. Park, M.G. Kim, S.J. Ahn, S. Ryu and H.M. Jang, J. Magn. Magn. Mater., **321** (2009) 1971.
10. J. Kulawik, P. Guzdek, D. Szwagierczak and A. Stoch, Compos. Struct., **92** (2010) 2153.
11. A. Gupta and R. Chatterjee, J. Magn. Magn. Mater., **322** (2010) 1020.
12. A.D. Sheikh and V.L. Mathe, J. Phys. Chem. Solids, **72** (2011) 1423.
13. A.P. Barranco, J.D.S. Guerra, R.L. Noda and E.B. Araujo, J. Phys. D: Appl. Phys., **41** (2008) 215503.
14. S. Singh, O.P. Thakur, C. Prakash and K.K. Raina, Phase Transitions, **78** (2005) 655.
15. L.I. Maissel and R. Glang, Handbook of Thin Film Technology, McGraw–Hill, New York (1970).
16. S. Chopra, S. Sharma, T.C. Goel and R.G. Mendiratta, Solid State Commun., **127** (2003) 299.
17. J.S. Kim, B.C. Choi, H.K. Yang and J.H. Jeong, J. Korean Phys. Soc., **52** (2008) 415.
18. B. Jaffe, W.R. Cook and H. Jaffe, Piezoelectric Ceramics, Academic Press, New York (1971).
19. M. Zivkovic, D. Stojanovic, C.R. Foschini, V. Paunovic and D. Mancic, Sci. Sinter., **35** (2003) 133.
20. S.B. Narang and D. Kaur, Ferroelectr. Lett., **36** (2009) 20.
21. J.Y. Zhai, N. Cai, L. Liu, Y.H. Lin and C.W. Nan, Mater. Sci. Eng. B, **99** (2003) 329.

22. X. Chao, Z. Yang, M. Dong and Y. Zhang, J. Magn. Magn. Mater., **323** (2011) 2012.
23. D. Pandey, N. Singh and S.K. Mishra, Indian J. Pure Appl. Phys., **32** (1994) 616.
24. H.J. Hagemann, J. Phys. C, **11** (1978) 3333.
25. A.R. James, J. Subrahmanyam and K.L. Yadav, Smart Mater. Struct., **39** (2006) 2259.
26. J.D. Mackenzie and Y. Xu, J. Sol–Gel Sci. Technol., **8** (1997) 673.
27. D. Wu, W. Gong, H. Deng and M. Li, J. Phys. D: Appl. Phys., **40** (2007) 5002.
28. C.M. Kanamadi, J.S. Kim, H.K. Yang, B.K. Moon, B.C. Choi and J.H. Jeong, Appl. Phys. A, **97** (2009) 575.
29. R.S. Devan, S.B. Deshpande and B.K. Chougule, J. Phys. D: Appl. Phys., **40** (2007) 1864.
30. J.A.M. Aquino, M.E.B. Zubiate, V.C. Flores, J.D. Frutos, F. Cebollada, E. Menendez, F.J. Jimenez and A.M. Gonzalez, Integr. Ferroelectr., **101** (2008) 22.
31. B.K. Bammannavar and L.R. Naik, J. Magn. Magn. Mater., **324** (2012) 944.
32. C.W. Nan, Phys. Rev. B, **50** (1994) 6082.
33. G.V. Duong and R. Groessingera, J. Magn. Magn. Mater., **316** (2007) e624.
34. C.M. Kanamadi, J.S. Kim, H.K. Yang, B.K. Moon, B.C. Choi and J.H. Jeong, J. Alloys Compd., **481** (2009) 781.
35. V.M. Laletin and V.M. Petrov, Solid State Commun., **151** (2011) 1806.

Chapter-VI

Characterization of Microwave Processed NZF-PZT Composites

Chapter–VI

Characterization of Microwave Processed NZF–PZT Composites

Synthesis of NZF–PZT composite system (series 4) using novel microwave sintering technique and detailed investigations of the structural, dielectric, ferroelectric, magnetic and magnetoelectric properties are given in this chapter. Also a comparison between the properties of conventionally sintered (CS) and microwave sintered (MS) samples is discussed in this chapter.

6.1 X–Ray Diffraction

Figure 6.1 shows XRD patterns for MS pure NZF sample (y = 1), pure PZT sample (y = 0) and NZF–PZT composite (y = 0.10). The patterns for y = 0 and 1 show well–defined peaks characteristic of rhombohedral perovskite structure and cubic spinel structure respectively. The diffraction peaks for y = 0.10 confirm the perovskite structure in the ferroelectric phase (PZT) and the cubic spinel structure in the ferrite phase (NZF). No extra peaks other than the constituent phases were observed in XRD pattern of y = 0.10 confirming that no chemical reaction took place between the two phases (NZF and PZT) during microwave sintering. The MS samples sintered at 1150 ^{o}C for 10 min showed XRD patterns that are similar to those of CS samples sintered at 1200 ^{o}C for 4 hrs (figure 3.6, chapter III).

The lattice constants for both phases are given in table 6.1 and values are compared with those for CS samples. The values of lattice constants corresponding to the constituent phases are found to be slightly different for CS and MS samples. The experimental density, X–ray density and relative density were calculated and values are compared in table 6.1. Comparison shows that density values are comparable to those obtained for CS samples.

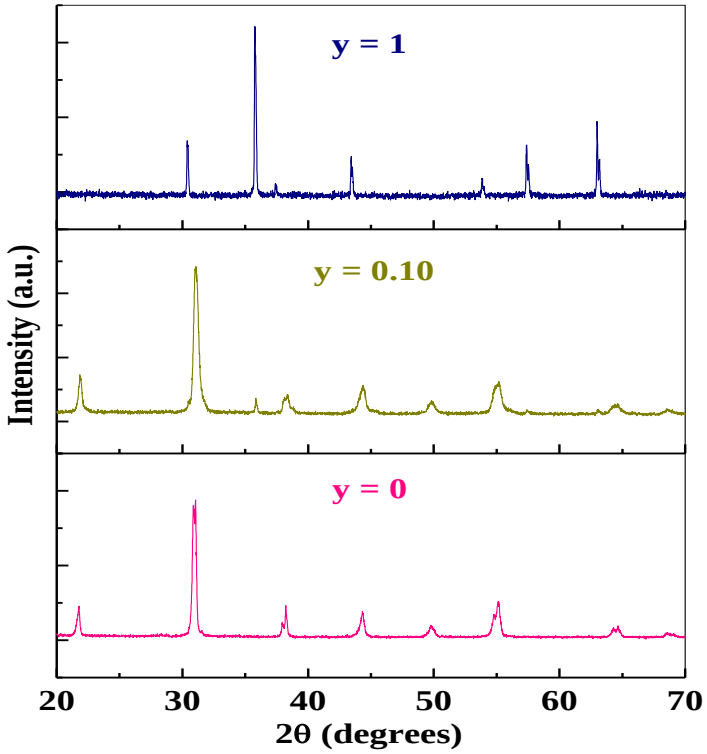

Figure 6.1 XRD patterns for MS NZF–PZT samples (y = 0, 0.10 and 1) at room temperature

6.2 Scanning Electron Microscope

The SEM micrographs of the freshly broken surfaces of CS and MS samples for y = 0, 0.10 and 1 are shown in figure 6.2. All micrographs show closely packed and well oriented grains. Comparison of micrographs shows that the MS samples are less porous than the CS samples. The average grain size was calculated by using line intercept method and is given in table 6.1. Average grain size is smaller for MS samples which may be due to rapid heating and very small processing time required in microwave sintering. Microwave sintering resulted in more uniform and finer microstructure which is an attractive feature for the processing of electroceramics [1–6].

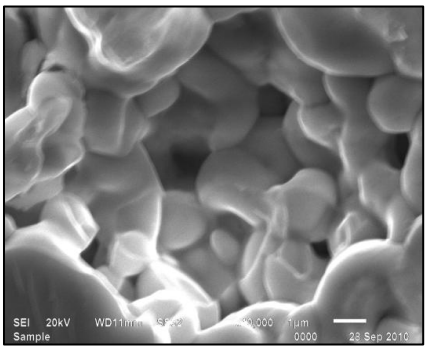

CS

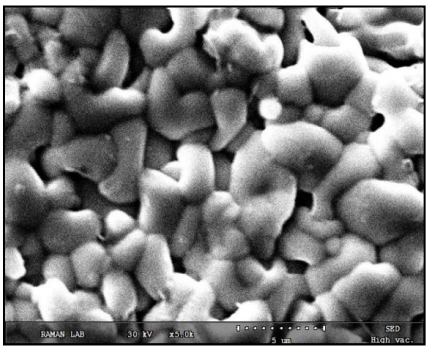

MS

y = 0

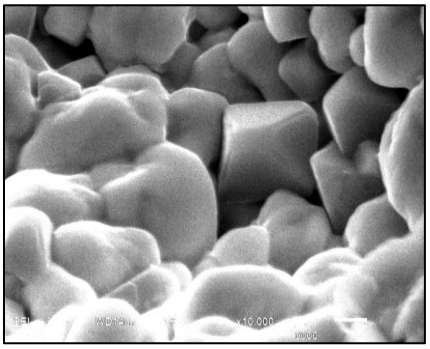

CS

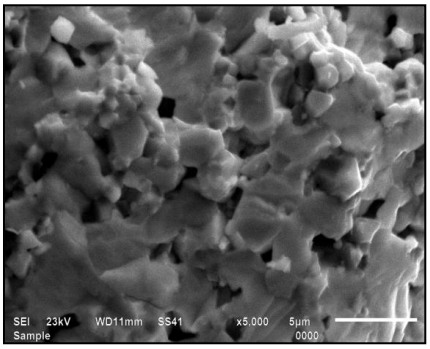

MS

y = 0.10

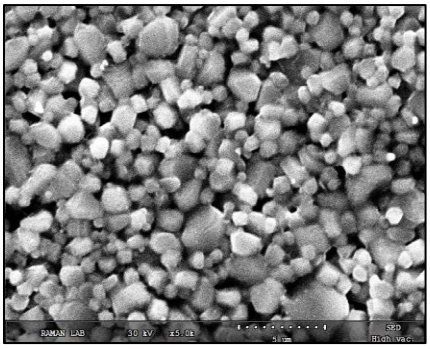

CS

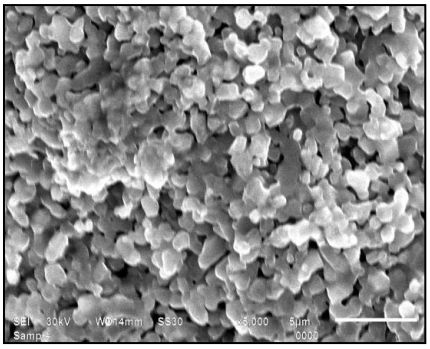

MS

y = 1

Figure 6.2 SEM micrographs for CS and MS NZF–PZT samples (y = 0, 0.10 and 1)

Table 6.1 Structural parameters for NZF–PZT samples

y	**0**		**0.10**		**1**	
	CS	**MS**	**CS**	**MS**	**CS**	**MS**
Lattice constant (Å) (Ferroelectric phase)	4.093	4.092	4.104	4.072	–	–
Lattice constant (Å) (Ferrite phase)	–	–	8.353	8.332	8.361	8.321
Exp. Density (g/cc)	7.58	7.70	6.88	7.01	4.63	4.79
X–ray Density (g/cc)	8.02	8.03	7.75	7.88	5.36	5.44
Relative Density (%)	94.5	95.9	88.8	88.9	86.4	88.1
Average grain size (µm)	2.3	2.2	2.4	1.3	1.2	1.0

6.3 Dielectric Properties

The variation of dielectric constant (ε') with temperature for MS samples (series 4) at discrete frequencies viz. 1, 10 and 100 kHz is shown in figure 6.3. The results obtained for MS samples are quite similar to those obtained for CS samples (series 1). For y = 0, initially the dielectric constant increases with increase in temperature and attains a maximum value (dielectric maxima, ε'_{max}) at the ferroelectric Curie temperature (T_c) and then decreases with further increase in the temperature. The position of dielectric maxima does not change with frequency indicating characteristics of normal ferroelectrics [7].

For MS NZF–PZT composites (y = 0.05, 0.10 and 0.15), dielectric maxima is observed at all frequencies which corresponds to ferroelectric–paraelectric transition in ferroelectric phase (PZT). In the paraelectric region, it is observed that there is an increase in the dielectric constant with increase in the temperature for y = 0.05, 0.10 and 0.15. But with an increase in the measurement frequency this observed behavior gradually reduces showing that it could be related to a low frequency relaxation process [8]. This behavior can be explained on the same lines as in case of CS composite samples.

For y = 1, an increase in the value of dielectric constant is observed with increase in temperature which is typical behavior of ferrites [9]. Further, this increase is quite significant at lower frequency (1 kHz).

Figure 6.4 shows the comparison of temperature dependence of the dielectric constant and loss for CS and MS NZF–PZT samples (y = 0, 0.05, 0.10, 0.15 and 1) at 100 kHz. The higher values of the loss are observed at high temperatures which may be attributed to the thermal conductivity losses. The values of ferroelectric Curie temperature (T_c), room temperature dielectric constant (ε'_{RT}), room temperature dielectric loss ($\tan\delta_{RT}$), dielectric constant at T_c (ε'_{max}) and dielectric loss at T_c ($\tan\delta_{max}$) at 100 kHz for all the samples are given in table 6.2. The comparison reveals that the rapid heating in microwave resulted in comparable dielectric properties as those obtained from conventional heating for the studied system.

Table 6.2 Dielectric parameters for NZF–PZT samples at 100 kHz

y	**0**		**0.05**		**0.10**		**0.15**		**1**	
	CS	**MS**	**CS**	**MS**	**CS**	**MS**	**CS**	**MS**	**CS**	**MS**
T_c (^oC)	422	442	394	408	408	412	407	422	–	–
ε'_{RT}	820	725	625	605	590	675	405	450	30	25
ε'_{max}	19585	23460	10760	9450	7635	7620	5275	5570	–	–
$\tan\delta_{RT}$	0.02	0.02	0.03	0.04	0.03	0.02	0.12	0.02	0.25	0.40
$\tan\delta_{max}$	0.10	0.07	0.15	0.29	0.22	0.33	0.31	0.23	–	–

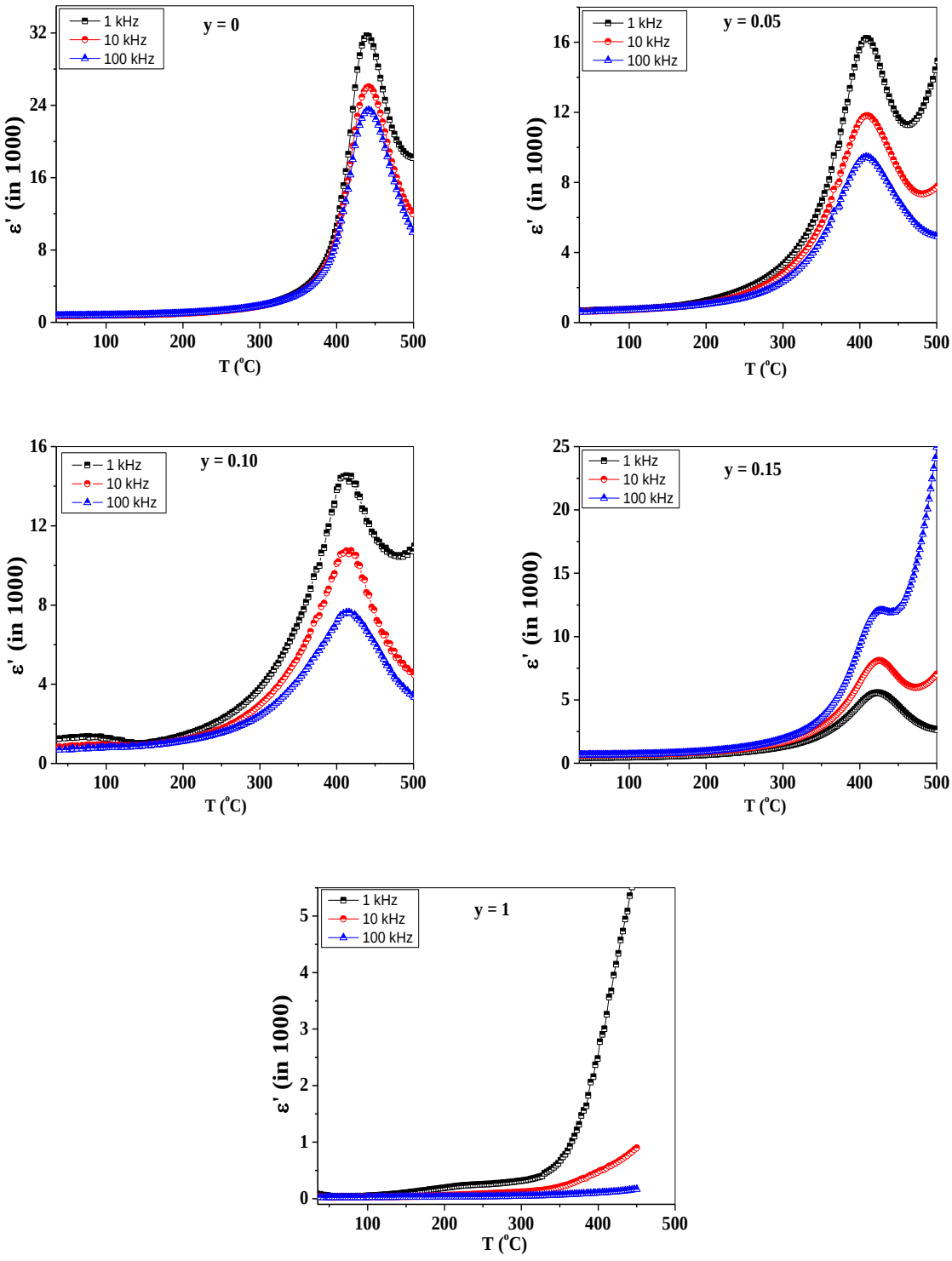

Figure 6.3 Temperature dependence of dielectric constant (ε') for MS NZF–PZT samples (y = 0, 0.05, 0.10, 0.15 and 1) at 1, 10 and 100 kHz

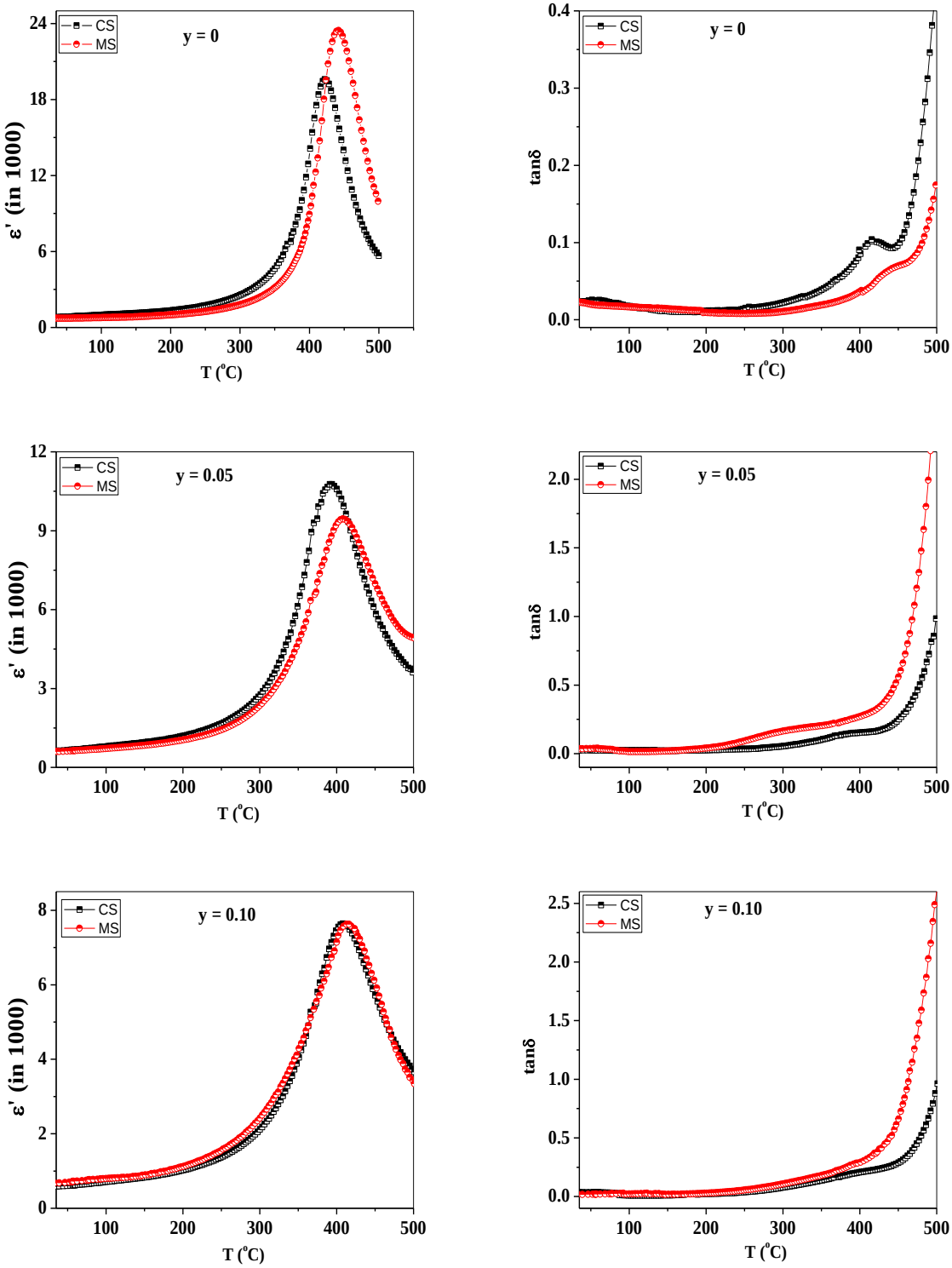

Figure 6.4 Comparison of temperature dependence of dielectric constant (ε') and loss (tanδ) for CS and MS NZF–PZT samples (y = 0, 0.05, 0.10, 0.15 and 1) at 100 kHz (continued)

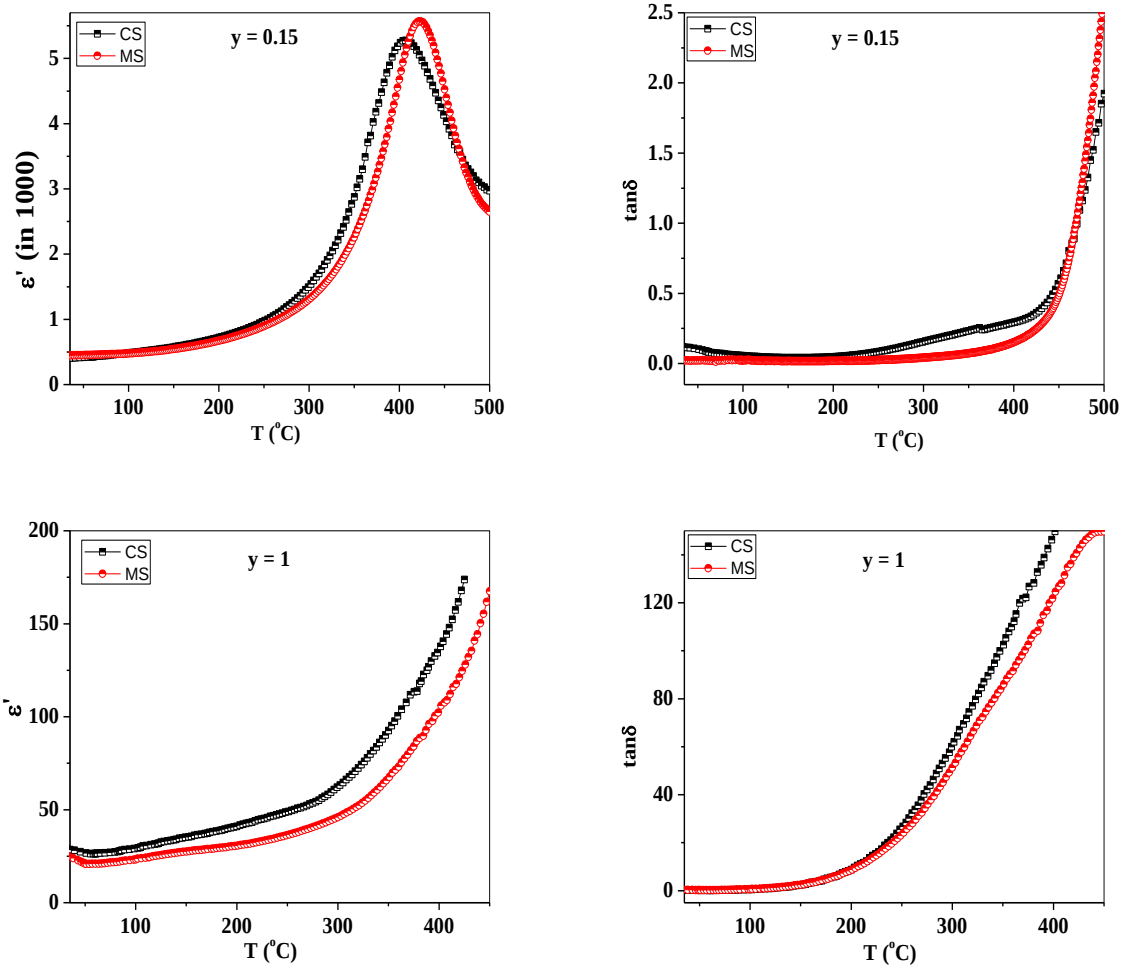

Figure 6.4 Comparison of temperature dependence of dielectric constant (ε') and loss (tanδ) for CS and MS NZF–PZT samples (y = 0, 0.05, 0.10, 0.15 and 1) at 100 kHz

6.4 Ferroelectric Properties

Room temperature P–E hysteresis loops were recorded for CS and MS samples (y = 0, 0.05 and 0.10) at 20 Hz frequency and results are shown in figure 6.5. The ferroelectric properties of conventionally sintered NZF–PZT composites (series 1) have already been discussed in detail (chapter III). The hysteresis loops confirm well defined ferroelectric behavior for all compositions. Remanant polarization (P_r), saturation polarization (P_s) and coercive field (E_c) were determined from the loops and are listed in table 6.3. Both the remanant polarization (P_r) and saturation polarization (P_s) were found to decrease with increase in ferrite content (y) i.e. ferroelectric behavior is weakening because ferrite (non–ferroelectric) grains are distributed along the circumference of ferroelectric phase resulting in low polarization values. Increase in the values of coercive field was observed with increase in y which is due to clamping effect derived from the ferrite phase (non–ferroelectric) [10]. P_r and P_s values are higher for MS samples which may be due to the change in the microstructure in case of MS samples as is evident from SEM micrographs.

Table 6.3 Ferroelectric parameters for NZF–PZT samples at 20 Hz

y	**0**		**0.05**		**0.10**	
	CS	**MS**	**CS**	**MS**	**CS**	**MS**
P_r ($\mu C/cm^2$)	25.7	32.5	10.4	12.3	9.2	13.9
P_s ($\mu C/cm^2$)	44.7	51.4	22.3	23.3	17.3	19.9
E_c (kV/cm)	7.2	7.2	8.6	9.5	11.3	11.3

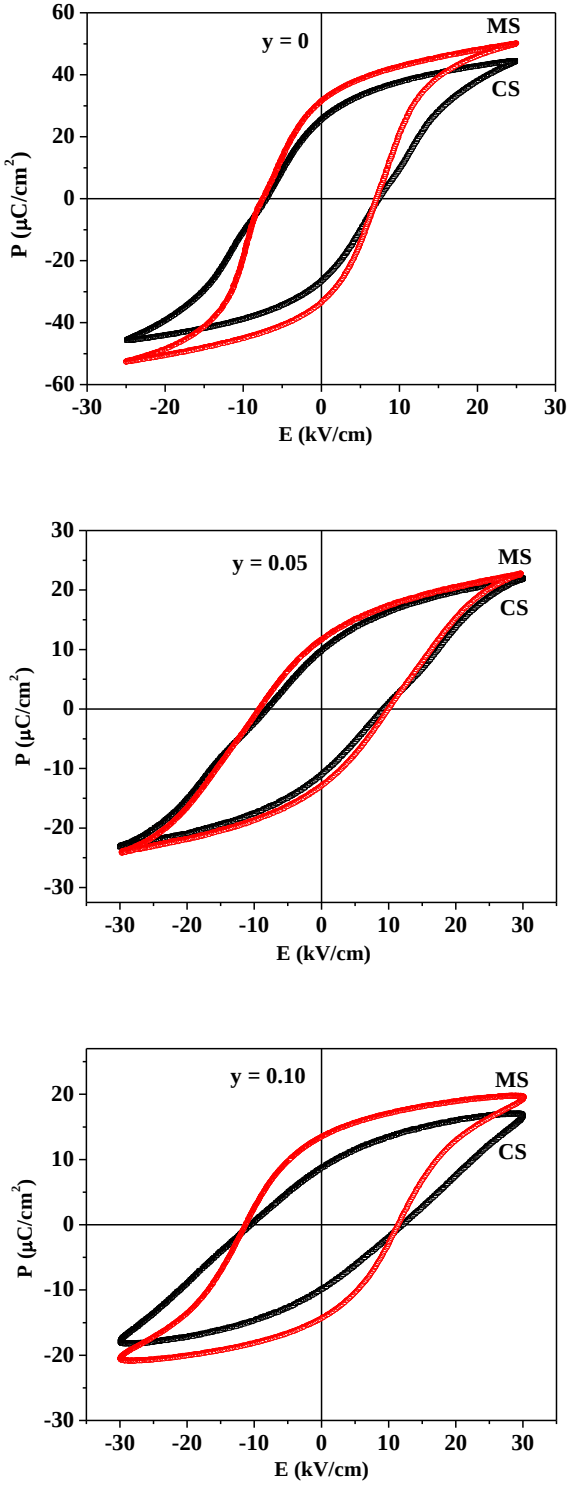

Figure 6.5 Room temperature P–E hysteresis loops for CS and MS NZF–PZT samples (y = 0, 0.05 and 0.10)

6.5 Ferromagnetic Properties

To study magnetic behavior, room temperature M–H hysteresis loops were recorded for composites (y = 0.05, 0.10 and 0.15) and pure NZF (y = 1). Comparison of M–H loops for CS and MS samples is shown in figure 6.6. All the samples show well defined ferromagnetic behavior confirming the existence of magnetic ordering in pure NZF sample as well as in mixed ferrite–ferroelectric (NZF–PZT) composite samples. All samples exhibit small coercive field values, which is typical behavior of soft ferrites. The values of remanant magnetization (M_r), saturation magnetization (M_s) and coercive field (H_c) determined from the loops are given in table 6.4.

For both CS and MS samples, an increasing trend in remanant magnetization (M_r) and saturation magnetization (M_s) with increase in ferrite content (y) was observed, as expected and is in well agreement with the literature [11–14]. The comparison of M–H loops for CS and MS samples shows that there is a significant increase in magnetization values for MS samples. This may be due to the interaction between 2.45 GHz microwave field with charged cations resulting in alteration of Zn^{2+} and Fe^{3+} arrangements [15] and these variations may contribute to the uncoupling effect [16, 17] resulting in higher values of magnetization for MS samples.

Table 6.4 Ferromagnetic parameters for NZF–PZT samples

y	**0.05**		**0.10**		**0.15**		**1**	
	CS	**MS**	**CS**	**MS**	**CS**	**MS**	**CS**	**MS**
M_r (emu/g)	0.06	0.09	0.09	0.15	0.18	0.29	0.25	0.67
M_s (emu/g)	1.7	3.1	3.7	5.6	5.9	9.6	56	63
H_c (Oe)	30	30	30	30	30	30	15	20

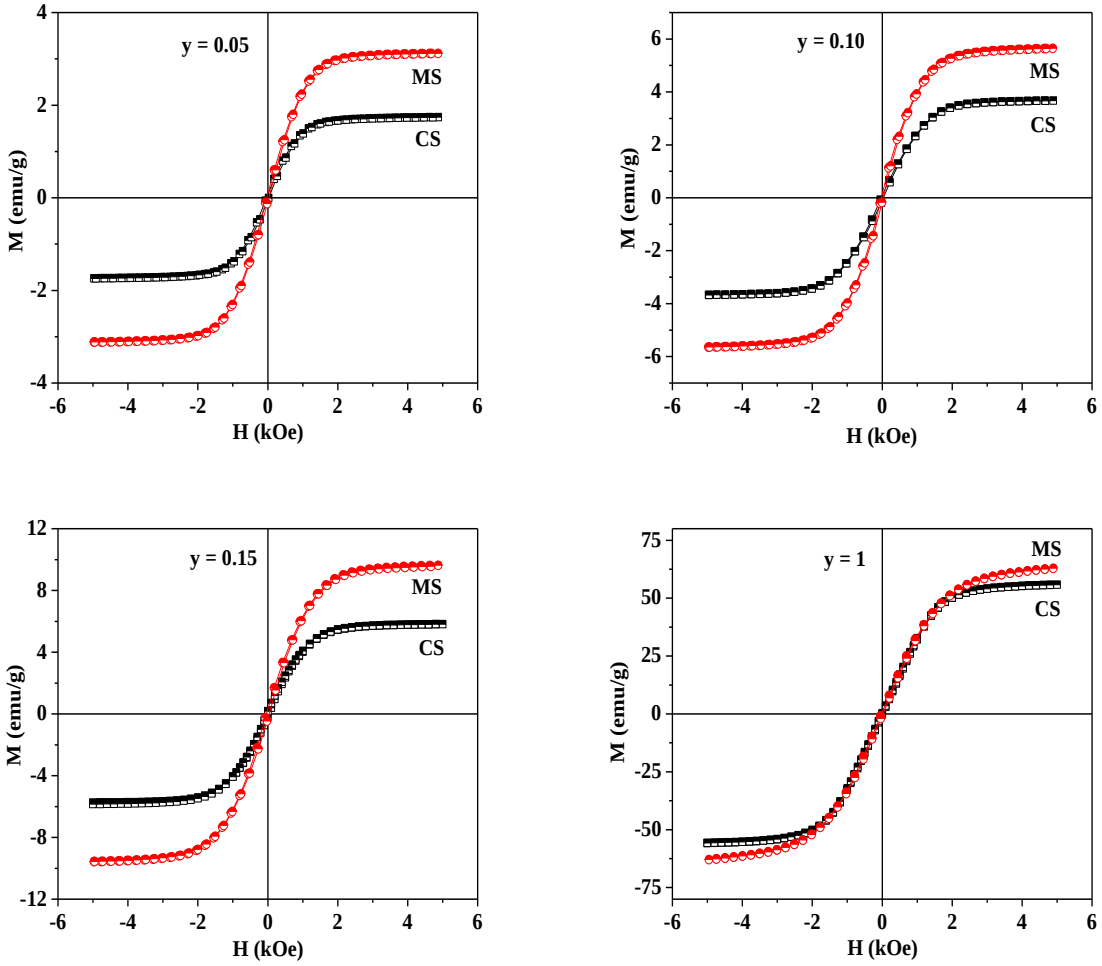

Figure 6.6 Room temperature M–H hysteresis loops for CS and MS samples (y = 0.05, 0.10, 0.15 and 1)

6.6 Magnetoelectric Properties

As discussed in chapter III, maximum ME coupling coefficient of 6.7 mV/(cm.Oe) was observed for y = 0.10 (series 1). Hence, in this chapter, magnetoelectric coupling is studied for microwave sintered NZF–PZT composite sample with y = 0.10. To confirm magnetoelectric coupling, two pieces from a single pellet were taken. One piece was electrically poled at 15 kV/cm. M–H hysteresis loops were recorded for both poled and unpoled samples and the data was compared. M–H hysteresis loops at room temperature for both samples are shown in figure

6.7. An enhancement in saturation magnetization (from 5.6 to 6.4 emu/g) for poled sample was observed, which confirms the magnetoelectric coupling between NZF phase and PZT phase for MS sample.

Figure 6.8 shows the typical variation of ME coupling coefficient (α) with applied DC magnetic field for CS and MS sample with y = 0.10. The experiment was performed in the presence of AC magnetic field of strength 10 Oe at 1 kHz. We have already discussed in detail (chapter III), the trend of changing α with applied DC magnetic field for conventionally sintered NZF–PZT composite samples. MS sample shows the quite similar trend with applied DC magnetic field. The values of coupling coefficient, α, are slightly higher for MS sample. The difference in ME coupling coefficients can be attributed to the difference in magnetic properties for CS and MS sample. This slight increase may be due to its higher saturation magnetization [18] as compared to that for CS sample. Maximum ME coupling coefficient of 7.0 mV/(cm.Oe) is observed for MS sample.

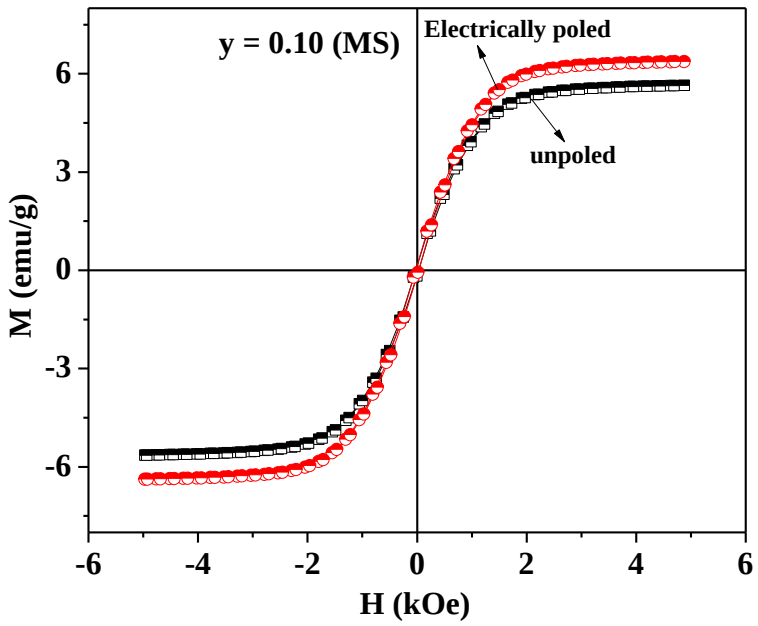

Figure 6.7 Room temperature M–H hysteresis loops for electrically poled and unpoled MS sample with y = 0.10 (series 4)

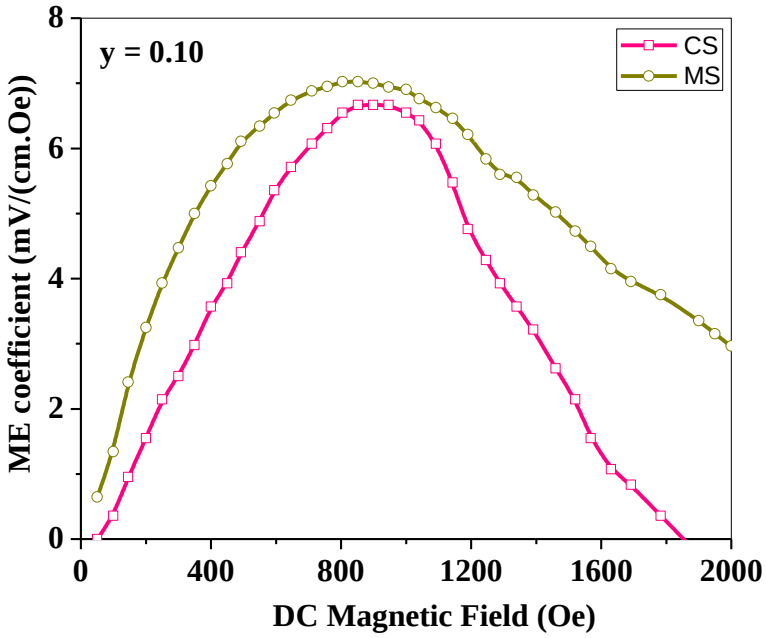

Figure 6.8 Variation of ME coupling coefficient, α (mV/(cm.Oe)) with DC magnetic field for CS and MS sample with y = 0.10

References

1. Z. Xie, Z. Gui, L. Li, T. Su and Y. Huang, Mater. Lett., **36** (1998) 191.
2. Z. Xie, J. Yang, X. Huang and Y. Huang, J. Eur. Ceram. Soc., **19** (1999) 381.
3. B. Vaidhyanathan, D.K. Agrawal, T.R. Shrout and Y. Fang, Mater. Lett., **42** (2000) 207.
4. B. Vaidhyanathan, A.P. Singh, D.K. Agrawal, T.R. Shrout and R. Roy, J. Am. Ceram. Soc., **84** (2001) 1197.
5. S. Rhee, D.K. Agrawal, T.R. Shrout and M. Thumm, Ferroelectrics, **261** (2001) 15.
6. O.P. Thakur, C. Prakash and D. Agrawal, Int. J. Ceram. Process. Res., **3** (2002) 75.
7. C. Prakash and O.P. Thakur, Mater. Lett., **57** (2003) 2310.
8. A.P. Barranco, J.D.S. Guerra, R.L. Noda and E.B. Araujo, J. Phys. D: Appl. Phys., **41** (2008) 215503.
9. L.L. Hench and J.K. West, Principles of Electronics Ceramics, John Wiley and Sons, New York (1990).
10. A.R. James, J. Subrahmanyam and K.L. Yadav, Smart Mater. Struct., **39** (2006) 2259.
11. D. Wu, W. Gong, H. Deng and M. Li, J. Phys. D: Appl. Phys., **40** (2007) 5002.
12. C.M. Kanamadi, J.S. Kim, H.K. Yang, B.K. Moon, B.C. Choi and J.H. Jeong, Appl. Phys. A, **97** (2009) 575.
13. R.S. Devan, S.B. Deshpande and B.K. Chougule, J. Phys. D: Appl. Phys., **40** (2007) 1864.
14. J.A.M. Aquino, M.E.B. Zubiate, V.C. Flores, J.D. Frutos, F. Cebollada, E. Menendez, F.J. Jimenez and A.M. Gonzalez, Integr. Ferroelectr., **101** (2008) 22.
15. P. Yadoji, R. Peelamedu, D. Agrawal and R. Roy, Mater. Sci. Eng. B, **98** (2003) 269.
16. M.U. Rana, T. Abbas and F.A. Khawaja, Mater. Lett., **52** (2002) 389.
17. T.T. Srinivasan, P. Ravindranathan, L.E. Cross, R. Roy, R.E. Newnham, S.G. Sankar and K.C. Patil, J. Appl. Phys., **63** (1988) 3789.
18. K. Tahmasebi, A. Barzegar, J. Ding, T.S. Herng, A. Huang and S. Shannigrahi, Mater. Design, **32** (2011) 2370.

Chapter-VII

Summary & Recommendations for Future Work

Chapter–VII

Summary & Recommendations for Future Work

7.1 Summary

The present work focuses on the synthesis and characterization of bulk NiZn ferrite–PZT composites. The modification was carried out by substituting La^{+3} and Sm^{+3} ions in PZT phase. This substitution was undertaken in a view to know the suitability of the substituting elements for the enhancement of dielectric, ferroelectric, piezoelectric properties of PZT ceramics. Thus, addition of La and Sm to PZT was expected to give rise to improved magnetoelectric properties. The samples were synthesized by conventional solid state reaction method. Some of the compositions (series 1) were also synthesized using novel microwave sintering technique. Over the course of this study, several important observations were made. The important findings of the entire work are summarized below:

1. Individual phases i.e. NiZn ferrite ($Ni_{0.8}Zn_{0.2}Fe_2O_4$) and PZT ($PbZr_{0.65}Ti_{0.35}O_3$) were synthesized using conventional solid state reaction method. The phase formation was confirmed by comparing their XRD patterns with standard JCPDS card 52–0277 for NZF and 89–1279 for PZT. Optimization of sintering temperature was done for $0.1Ni_{0.8}Zn_{0.2}Fe_2O_4$–$0.9PbZr_{0.65}Ti_{0.35}O_3$ composite sample. This sample was sintered at four different sintering temperatures (1100 ^oC, 1150 ^oC, 1200 ^oC and 1225 ^oC) for 4 hrs. Relative density, dielectric constant (ε'), remanant polarization (P_r), saturation polarization (P_s), piezoelectric coefficient (d_{33}), remanant magnetization (M_r) and saturation magnetization (M_s) were observed to be maximum for the sample sintered at 1200 ^oC.

2. Further study on $yNi_{0.8}Zn_{0.2}Fe_2O_4$–$(1–y)PbZr_{0.65}Ti_{0.35}O_3$, y = 0, 0.05, 0.10, 0.15 and 1 (series 1) was carried out. All samples were prepared by conventional solid state route at optimized sintering temperature, 1200 ^oC for 4 hrs. Coexistence of individual phases was

confirmed using XRD analysis. Decrease in the dielectric constant and increase in the loss with increase in the ferrite concentration (y) was observed. Increase in P_r and P_s with increase in ferroelectric content and increase in M_r and M_s with increase in ferrite content show that these composites obey the rule of mixtures. Change in values of M_r and M_s for electrically poled composite samples and generation of polarization by applying magnetic field are the evidences for magnetoelectric coupling in these composites. The maximum value of ME coupling coefficient of 6.67 mV/(cm.Oe) was observed for composite sample with y = 0.10.

3. To study the effect of La substitution, composites having general formula $yNi_{0.8}Zn_{0.2}Fe_2O_4–(1–y)Pb_{1–3x/2}La_xZr_{0.65}Ti_{0.35}O_3$ with x = 0.01, 0.02, 0.03 and y = 0, 0.05, 0.10, 0.15 (series 2) were synthesized by conventional solid state reaction route. The value of T_c was found to decrease with increase in La substitution (x). Results discussed in chapter–IV show that La substitution not only results in improved dielectric properties of pure ferroelectric series (y = 0) but also for composite series (y = 0.05, 0.10 and 0.15). On comparing the frequency dispersion for unsubstituted samples (x = 0) with that for substituted ones (x = 0.01, 0.02 and 0.03), we observed that dispersion is more in case of unsubstituted samples for all the series. La substitution results in increase in P_r as well as E_c for samples of series 2B and 2C. The gradual increase in d_{33} values was also observed with increase in La substitution. Maximum coupling coefficient of 18.5 mV/(cm.Oe) was observed for x = 0.03 due to higher d_{33} value of ~ 89 pC/N.

4. Composites having general formula $yNi_{0.8}Zn_{0.2}Fe_2O_4–(1–y)Pb_{1–3x/2}Sm_xZr_{0.65}Ti_{0.35}O_3$ with x = 0.01, 0.02, 0.03 and y = 0.05, 0.10 (series 3) were synthesized and characterized for their structural, dielectric, ferroelectric, piezoelectric, ferromagnetic and magnetoelectric properties for studying the effect of Sm substitution. Change in dielectric properties (ε' and tanδ) is more significant for Sm substituted series as compared to that for La substituted series due to more lattice anisotropy created in case of Sm substitution, as is evident from X–ray diffraction study. Sm substitution makes the materials more soft resulting in higher P_r, P_s and lower E_c as compared to that for La substitution. An enhancement in saturation magnetization (from 1.9 to 2.3 emu/g) for poled sample with x

= 0.05 was observed which can be exploited for sensor applications. Maximum α of 22.5 mV/(cm.Oe) was observed for the composite sample with x = 0.03 and y = 0.10 and is higher as compared to those reported for bulk ferrite–ferroelectric composites in literature.

5. The microwave sintered (MS) samples at 1150 ^{o}C for 10 min showed XRD patterns that were similar to those of conventionally sintered (CS) samples sintered at 1200 ^{o}C for 4 hrs. Microwave sintering resulted in more uniform and finer microstructure which is an attractive feature for the processing of electroceramics. The comparison between CS and MS samples reveals that the rapid heating in microwave resulted in comparable dielectric properties as those obtained from conventional heating for the studied system. P_r and P_s values are higher for MS samples which may be due to the change in the microstructure in case of MS samples. A significant increase in magnetization values for MS samples was also observed. The values of coupling coefficient, α are slightly higher for MS sample.

7.2 Recommendations for Future Work

An extension of the present study can be made to some areas which are not yet explored. Following are the few suggestions for future extension of this work:

1. The investigated La and Sm modified compositions have potential for applications in multifunctional devices. The thin films of the selected compositions may be made for enhanced magnetoelectric coupling.
2. Novel microwave sintering technique may be adopted for La and Sm modified NZF–PZT composites.
3. It would be quite interesting to study the grain size effect on magnetoelectric coupling.
4. A systematic study of frequency dependence of ME coupling may be done using dynamic method adopted in the present study. It would be helpful to enhance the ME output by several times at frequency of electromechanical resonance.